Optics measurement and correction for future electron circular colliders

Dissertation
zur Erlangung des Doktorgrades
an der Fakultät für Mathematik, Informatik und Naturwissenschaften
Fachbereich Physik
der Universität Hamburg

vorgelegt von

Elaf Salah Hassan Musa

Hamburg
2024

Gutachter/innen der Dissertation:	Prof. Dr. Wolfgang Hillert
	Dr. Ilya Agapov
Zusammensetzung der Prüfungskommission:	Prof. Daniela Pfannkuche
	Prof. Wolfgang Hillert
	Prof. Gudrid Moortgat-Pick
	Dr. Ilya Agapov
	Dr. Tessa Charles
Vorsitzende/r der Prüfungskommission:	Prof. Daniela Pfannkuche
Datum der Disputation:	11.12.2024
Vorsitzender des Fach-Promotionsausschusses PHYSIK:	Prof. Dr. Markus Drescher
Leiter des Fachbereichs PHYSIK:	Prof. Dr. Wolfgang J. Parak
Dekan der Fakultät MIN:	Prof. Dr.-Ing. Norbert Ritter

Declaration on oath

I hereby declare and affirm that this doctoral dissertation is my own work and that I have not used any aids and sources other than those indicated. If electronic resources based on generative artificial intelligence (gAI) were used in the course of writing this dissertation, I confirm that my own work was the main and value-adding contribution and that complete documentation of all resources used is available in accordance with good scientific practice. I am responsible for any erroneous or distorted content, incorrect references, violations of data protection and copyright law or plagiarism that may have been generated by the gAI.

Signature of doctoral candidate _____ Date _____

"The prize is the pleasure of finding the thing out."

- Richard Feynman, Nobel Laureate

Abstract

The development of ultra-low emittance storage rings, such as the e+/e- Future Circular Collider (FCC-ee) with a circumference of about 90 km, aims to achieve unprecedented luminosity and beam size. One significant challenge is correcting the optics, which becomes increasingly difficult as we target lower emittances. The use of stronger quadrupoles and sextupoles makes these machines particularly sensitive to misalignments, which can severely impact performance. This study investigates optics correction methods to address these challenges. We examined the impact of arc and Interaction Region (IR) magnet alignment errors in two optics design options for the FCC-ee, called Baseline and Local Chromatic Correction Optics (LCCO). To establish realistic alignment tolerances, we developed a sequence of correction steps using the Python Accelerator Toolbox (PyAT) to correct the lattice optics, achieve nominal emittance, and large Dynamic Aperture (DA). We focused initially on the Linear Optics from Closed Orbit (LOCO) method, which fits the measured Orbit Response Matrix (ORM) to the lattice model to determine optimal parameters such as quadrupole strengths. We implemented a Python-based numerical code for LOCO correction and evaluated its effectiveness for the FCC-ee. Preliminary results indicate successful optics corrections. We also compared LOCO with phase advance + η_x and coupling Resonance Driving Terms (RDTs) + η_y optics correction, finding that the latter performed better in achieving design emittance values and a large DA area for realistic alignment tolerances, for the studied cases. The code was further optimized and expanded to include more realistic scenarios. Additionally, we applied LOCO to PETRA IV -a fourth generation light source upgrade, and integrated the code into the Python Simulated Commissioning toolkit for Synchrotrons (PySC).

Zusammenfassung

Die Entwicklung von Speicherringen der nächsten Generation, wie dem e+/e- Future Circular Collider (FCC-ee) mit einem Umfang von etwa 90 km, zielt darauf ab, beispiellose Leuchtkraft und Strahlgröße zu erreichen. Eine bedeutende Herausforderung besteht in der Korrektur der Optik, die zunehmend schwieriger wird, wenn wir niedrigere Emittanzen anstreben. Der Einsatz stärkerer Quadrupole und Sextupole macht diese Maschinen besonders empfindlich gegenüber Fehlern in der Magnetausrichtung, die die Leistung erheblich beeinträchtigen können. Diese Studie untersucht Methoden zur Optikkorrektur, um diese Herausforderungen zu bewältigen. Wir untersuchten die Auswirkungen von Ausrichtungsfehlern der Magnete im Bogen und in der Interaktionsregion (IR) in zwei Optikoptionen für den FCC-ee: Baseline und LCCO @ Z-Energie. Um realistische Ausrichtungstoleranzen festzulegen, entwickelten wir eine Abfolge von Korrekturschritten mithilfe des Python Accelerator Toolbox (PyAT), um die Optik zu korrigieren, die nominale Emittanz zu erreichen und die Dynamische Apertur (DA) zu optimieren. Zunächst konzentrierten wir uns auf die Methode LOCO (Linear Optics from Closed Orbit), die die gemessene Orbit Response Matrix (ORM) an das Lattice-Modell anpasst, um optimale Parameter wie die Quadrupolstärken zu bestimmen. Wir implementierten einen Python-basierten numerischen Code zur LOCO-Korrektur und bewerteten dessen Wirksamkeit für den FCC-ee. Vorläufige Ergebnisse zeigen erfolgreiche Optikkorrekturen. Wir verglichen auch LOCO mit der Phasenvorschub und RDTs-Optikkorrektur und stellten fest, dass letztere bei der Erreichung der Entwurfs-Emittanzwerte und einer großen DA-Fläche für realistische Ausrichtungstoleranzen in den untersuchten Fällen besser abschnitt. Der Code wurde weiter optimiert und erweitert, um realistischere Szenarien zu berücksichtigen. Darüber hinaus wendeten wir LOCO auf das PETRA IV Lattice an und integrierten den Code in die

Python Simulated Commissioning toolkit for Synchrotrons (PySC).

Table of Contents

List of Figures

List of Tables

Abbreviations

AT	Accelerator Toolbox
BBA	Beam-Based Alignment
BPM	Beam Position Monitors
CDR	Conceptual Design Report
CEPC	Circular Electron Positron Collider
CERN	European Organization for Nuclear Research in Geneva, Switzerland
COD	Closed Orbit Distortion
CW	Crab Waist scheme
DA	Dynamic Aperture
DBA	Double Bend Acromat
DC	Unidirectional flow of electric charge
DESY	Deutsches Elektronen Synchrotron
DFS	Dispersion-Free Steering
ESRF	European Synchrotron Radiation Facility
FCC	Future Circular Collider

FCC-ee	electron-positron Future Circular Collider
FCC-hh	hadron-hadron Future Circular Collider
FMA	Frequency Map Analysis
FODO	Focusing and defocusing quadrupoles in alternating order
GN	Gauss-Newton method
HFD	Hybrid FoDo cell
ILC	International Linear Collider
IP	Interaction Point
IR	Interaction Region
KEK	High energy accelerator research organisation in Tsukuba, Ibaraki Prefecture, Japan
LEP	Large Electron-Positron collider
LHC	Large Hadron Collider
LM	Levenberg-Marquardt method
LOCO	Linear Optics from Closed Orbit
MAD-X	Methodical Accelerator Design version X
MATLAB	Commercially developed environment for technical computing and visualization
MICADO	Most effective corrector algorithm
ORM	Orbit Response Matrix
PETRA	Positron–Electron Tandem Ring Accelerator

PyAT	Python Accelerator Toolbox
PySC	Python version of the Simulated Commissioning toolkit for synchrotrons
QF, QD	Focussing, Defocussing Quadrupole
RDTs	Resonant Driving Terms
RF	Radio Frequency
SAD	Strategic Accelerator Design
SF, SD	Focussing, Defocussing Sextupole
SPS	Super Proton Synchrotron
SR	Synchrotron Radiation
SuperKEKB	Asymmetric-energy electron-positron collider
SVD	Singular Value Decomposition

Symbols

α, γ	Twiss parameters
α_{c}	Momentum compaction factor
α_{f}	Fine structure constant
β	Beta or amplitude function
β^*	Beta function at the interaction point
δ	Momentum deviation
ΔE_{loss}	Energy loss per turn
ε	Emittance
ϵ_0	Permittivity of vacuum
γ_L	Lorentz factor
$\lvert\kappa_{\pm}\rvert$	Driving terms for the sum and difference resonance
$\mathcal{I}_2$	Second SR integral
$\mathcal{L}$	Luminosity
ϕ	Initial condition phase
ψ	Phase advance

ρ	Bending radius
$\sigma_{x,y}$	Horizontal and vertical rms transverse beam size
σ_s	Bunch length
σp	Cross-section of particle reaction
θ	Crossing angle of two beams collision or orbit corrector strength
θ_b	Bending angle
Υ	Beamstrahlung parameter
ξ_x, y	Beam parameter
A	Trace space area
A_u	Amplitudes of both synchrotron oscillation and betatron oscillations
c	Speed of light
D	Dispersion function
E	Particle energy
e^-	Electron
e^+	Positron
f	Focal length of quadrupole magnets
f_{rev}	Revolution frequency
f_{1001}, f_{1010}	Coupling resonance driving terms
h	Hadron
J_i	Damping partition numbers

L	Circumference of the design orbit
m	Particle mass
$\boldsymbol{M}$	Transfer matrix
N_1, N_2	Bunch population of both beams
$\boldsymbol{p}$	Particle momentum
P_γ	SR total power
q	Particle charge
$Q_{x,y}$	Horizontal and vertical tune
Q'	Chromaticity function
$\vec{\eta}_{xy}$	Horizontal and vertical dispersion
$\dot{N}\mathrm{p}$	Number of interaction events per second
r_0	Classical electron radius
S	Luminosity reduction factor
U	Voltage
$\boldsymbol{v}$	Particle velocity
$\boldsymbol{B}$	Magnetic field
$\boldsymbol{E}$	Electric field
$\boldsymbol{F}$	Lorentz force

Chapter 1

Introduction

1.1 Motivation

Since the 1920s, various machines have been built to accelerate particle beams and were continuously developed aiming to achieve higher energies. One of the main applications of particle accelerators is in experimental nuclear and particle physics research. By increasing the energy that particles can reach, these accelerators have led to the discovery of many subatomic particles, including the antiproton, gluon, top quark, Higgs boson, and many other particles [1]. In nuclear physics, researches have covered a wide range of studies, from precise particles energy measurements to the exploration of phenomena like the quark-gluon plasma. Over time, the applications of particle accelerators have expanded beyond fundamental research to include various other fields such as health, food quality, and more. In addition, particle accelerators also play a crucial role in materials science and industrial applications enabling processes such as ion implantation and lithography. Biological and medical research benefits from X-rays produced by light source accelerators, or accelerated ion beam, that used in radiation therapy for medical treatments.

Over the years, advances in accelerator physics technology have enabled the achievement of increasingly higher particle energies, providing a more microscopic probe for understanding elementary particles and their interactions. Research and development in accelerator physics blossomed during the 1950s, supported by the development of high-power radio

frequency sources and increased government funding for accelerator projects [2]. Alongside technological progress, the growing number of publications in the field reflects increased research activity and interest [3].

The Future Circular Collider (FCC) study was launched, as an international collaboration hosted by CERN [4]. The FCC covers a high-luminosity lepton collider (FCC-ee) and an energy-frontier hadron collider (FCC-hh). This thesis focuses on the electron position collider, FCC-ee, representing the next intensity frontier in particle physics research, that aims to push the limits of the achievable centre-of-mass collision energy and luminosity. This will make the FCC-ee a unique precision instrument to study the heaviest known particles (Z, W and H bosons and the top quark), offering great insights into new physics.

This thesis is organized in five chapters, The first chapter provides an introduction to particle colliders, discussing different types of particle colliders. It also delves into beam dynamics, optics functions, and the role of different magnets. Additionally, this first chapter introduces computer codes used in accelerator physics. The second chapter, focuses on the proposed FCC-ee, it details the FCC-ee optics design and parameters and also highlights the specific challenges faced by this machine. The sources of magnet imperfections and their impact on machine performance will be presented in the third chapter, followed by discussion of several orbit and optics correction algorithms, to address these imperfections. In the fourth chapter, we present detailed results from tuning simulations for FCC-ee, covering a variety of studies followed by conclusions and outlook in the final chapter.

1.2 Beam dynamics and lattice optics

Beam dynamics is a crucial concept in the study of particle accelerators, it focuses on the behavior of particle beam as it travels through the various components of the accelerator. In this section, we will introduce the fundamental parameters and equations governing the motion of particles in accelerator.

1.2.1 Accelerator magnets

Accelerators are described as sequence of elements along the nominal trajectory of the beam, the horizontal and vertical axes of the coordinate system that describe the motion of beam particles are labelled by x and y respectively. The magnetic field component has the form $B = (B_x, B_y, 0)$, since the transverse dimensions of the beam are small compared to the radius of curvature of the particles trajectory, one may expand the magnetic field component in the vicinity of the nominal trajectory using Taylor series expansion [5], where n is the number of multipoles terms:

$$B_y(x) = B_{y0} + \sum_{n=1}^{\infty} \frac{1}{n!} \frac{d^n B_y}{dx^n} x^n \tag{1.1}$$

For optics design it is convenient to normalize the multipoles strengths to the particle momentum to get an energy-independent description of the focusing properties. By multiplying Eq.(1.1) by the factor $\frac{q}{\boldsymbol{p}}$, where q and $\boldsymbol{p}$ are the particle charge and momentum respectively, it becomes:

$$\frac{q}{\boldsymbol{p}} B_y(x) = \frac{q}{\boldsymbol{p}} B_{y0} + \sum_{n=1}^{\infty} \frac{1}{n!} \frac{q}{\boldsymbol{p}} \frac{d^n B_y}{dx^n} x^n \tag{1.2}$$

$$\frac{q}{\boldsymbol{p}} B_y(x) = \frac{q}{\boldsymbol{p}} B_{y0} + \frac{q}{\boldsymbol{p}} \frac{dB_y}{dx} x + \frac{1}{2!} \frac{q}{\boldsymbol{p}} \frac{d^2 B_y}{dx^2} x^2 + \frac{1}{3!} \frac{q}{\boldsymbol{p}} \frac{d^3 B_y}{dx^3} x^3 + \dots \tag{1.3}$$

$$\frac{q}{\boldsymbol{p}} B_y(x) = \frac{1}{R} + k_1 x + \frac{1}{2!} k_2 x^2 + \frac{1}{3!} k_3 x^3 + \dots \tag{1.4}$$

The magnetic field in an accelerator may therefore be described as a sum of multipoles terms and these terms in Eq.(1.4) corresponds to the dipole, quadrupole, sextupole, octupole and higher order terms respectively. Each of these terms has a different effect on the path and shape of the beam. If only the two lowest multipoles (dipole and quadrupole) are used for beam steering and focusing in an accelerator, the optics are considered as linear beam optics. Higher multipoles (sextupole, octupole etc.) are either unwanted field errors or are intentionally introduced for some parameters correction (e.g. sextupoles are used for chromaticity correction as will be described in Sec. 1.2.3).

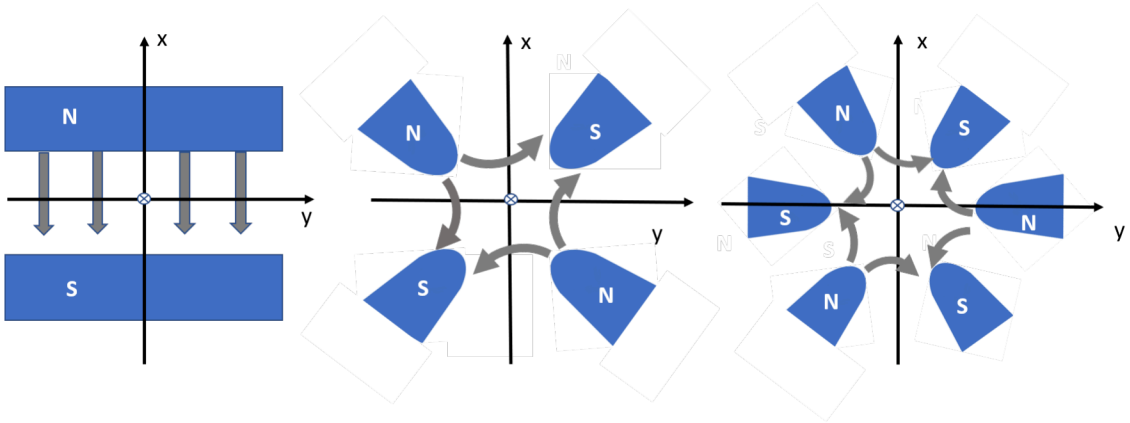

Figure 1.1: Magnetic field patterns of various magetic multipoles: dipole (left), quadrupole (middle), and sextupole (right).

Magnetic field lines of the first three multipoles are shown in Fig. 1.1. The different accelerator magnet designs and properties are described in many resources [6–8] . In the third chapter of this thesis we will discuss the different types of imperfections of these magnets and their impact in beam optics.

1.2.2 Equation of motion

As mentioned earlier the beam dynamics of charged particles in an accelerator describes the movement of single or multiple particles under the influence of external bending and focusing magnetic fields.

Starting from the basic Lorentz equation of motion for a particle of charge q moving under the influence of electric and magnetic fields $\boldsymbol{E}$, $\boldsymbol{B}$, we can define the force that controls the particle's motion as follows [9]:

$$\boldsymbol{F} = \frac{d\boldsymbol{p}}{dt} = q(\boldsymbol{v} \times \boldsymbol{B} + \boldsymbol{E}), \tag{1.5}$$

where $\boldsymbol{p} = \gamma_L m\boldsymbol{v}$ is the particle's momentum, $\boldsymbol{v}$ is the velocity vector, and m is the invariant particle mass. In the momentum expression, γ_L is the Lorentz factor,

$$\gamma_L \equiv \frac{1}{\sqrt{1 - \frac{v^2}{c^2}}}. \tag{1.6}$$

As the particle moves from point r_1 to r_2, the particle's energy changes by the amount:

$$\Delta E = \int_{\boldsymbol{r}_1}^{\boldsymbol{r}_2} \boldsymbol{F} \cdot d\boldsymbol{r} = q \int_{\boldsymbol{r}_1}^{\boldsymbol{r}_2} (\boldsymbol{v} \times \boldsymbol{B} + \boldsymbol{E}) \cdot d\boldsymbol{r}. \tag{1.7}$$

The path element $d\boldsymbol{r}$ is always parallel to $\boldsymbol{v}$. The vector $\boldsymbol{v} \times \boldsymbol{B}$ is perpendicular to $d\boldsymbol{r}$. At relativistic speeds, electric fields $\boldsymbol{E}$ and magnetic fields $\boldsymbol{B}$ have the same effect if $|\boldsymbol{E}| = c|\boldsymbol{B}|$. This implies that a magnetic field with a strength of $|\boldsymbol{B}| = 1\,\mathrm{T}$ is equivalent to an electric field of $|\boldsymbol{E}| = 3 \times 10^8\,\mathrm{Vm}^{-1}$. Magnetic fields over $1\,\mathrm{T}$ can be relatively easily produced using conventional methods, whereas generating an electric field of $3 \times 10^8\,\mathrm{Vm}^{-1}$ requires special types of accelerators (e.g., laser-plasma accelerators). Consequently, magnets are almost always used to steer beams in modern accelerators. Electric fields can steer beam only at very low energies, and are instead used for acceleration, where the energy gain from the electric field directly follows from Eq.(1.7):

$$\Delta E = q \int_{\boldsymbol{r}_1}^{\boldsymbol{r}_2} \boldsymbol{E} \cdot d\boldsymbol{r} = qU, \tag{1.8}$$

where U is the voltage crossed by the particle.

The forces used to bend and focus particle beams are perpendicular to both $\boldsymbol{v}$ and $\boldsymbol{B}$. As a result, the charged particles will move in a circular path or orbit. The condition for this

circular orbit is given by the equality of the Lorentz force and the centrifugal force that keeps the particle in a curved path:

$$q \cdot \boldsymbol{v} \cdot \boldsymbol{B} = \frac{m\boldsymbol{v}^2}{\rho}, \tag{1.9}$$

where ρ is the perpendicular distance from axis of rotation to the center of curvature known as the bending radiance. This equation also introduce the quantity known as the magnetic rigidity $\boldsymbol{B}\rho = \frac{\boldsymbol{p_b}}{q}$. Given a bending magnet that is designed to bend a beam on a circular orbit with bending radius ρ, its $\boldsymbol{B}\rho$ value indicates the corresponding beam momentum.

From the Lorentz force law, the bending angle θ_b is given by:

$$\theta_b = \frac{q}{\boldsymbol{p}_b}\int_{s_1}^{s_2} \boldsymbol{B}dl = \frac{1}{\boldsymbol{B}\rho}\int_{s_1}^{s_2} \boldsymbol{B}dl, \tag{1.10}$$

where $\boldsymbol{p}_b$ is the momentum of the beam, and $\boldsymbol{B}\rho = \boldsymbol{p}_b/q$ is the magnetic rigidity of the beam. The total bending angle for a circular accelerator is 2π, and the total integrated dipole field is

$$\oint \boldsymbol{B}dl = 2\pi\frac{\boldsymbol{p}_0}{q} = 2\pi\boldsymbol{B}\rho. \tag{1.11}$$

were $\boldsymbol{p}_0$ is the momentum of the reference particle.

The reference orbit is the path of the ideal particle. However, due to various errors, the actual orbit of particles (closed orbit) does not coincide with the ideal orbit, and the motion of a particle in the accelerator can be described with respect to the reference orbit using the curvilinear coordinate system (x, y, s) where s is the axis along the beam direction or trajectory. More precisely, it is the tangent to the reference orbit, while the horizontal and vertical axes are labelled x and y respectively as illustrated in Fig. 1.2.

The motion of particles through the accelerator can be described by the Hill's differential equation of motion. A full derivation of the linear equations of motion can be found in [10]. We write them here as,

$$x''(s) + \left(\frac{1}{\rho^2} - k_1(s)\right) \cdot x(s) = \frac{1}{\rho}\frac{\Delta p}{p_0} \tag{1.12}$$

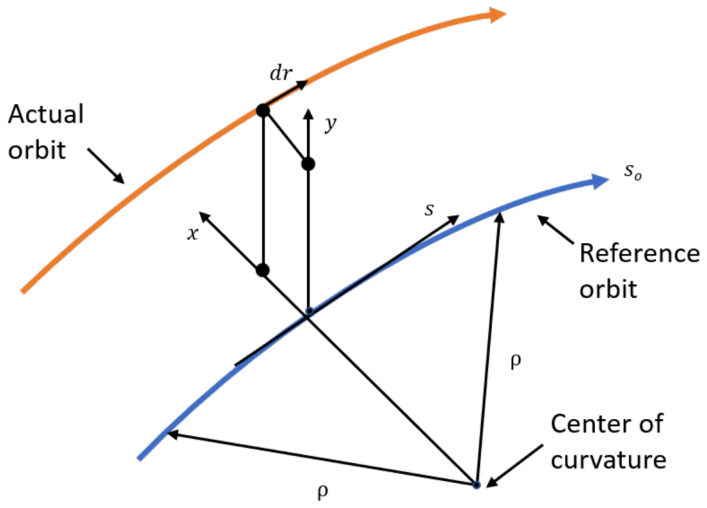

Figure 1.2: Curve linear coordinate system for particle motion in synchrotron

$$y''(s) + k_1(s) \cdot y(s) = 0 \tag{1.13}$$

where $k_1(s)$ is the focusing strength of the quadrupole elements. $\frac{1}{\rho}$ is the weak focusing term of the dipole field, $\Delta \boldsymbol{p}$ represent the particle momentum deviation from the momentum of reference particle $\boldsymbol{p_0}$. For monochromatic particle beams $\Delta \boldsymbol{p_0} = 0$.

We will continue to concentrate on the situation where $\Delta \boldsymbol{p}/\boldsymbol{p_0} = 0$. The solutions of the equation depend on the sign of the quadrupole strength, for $k_1 < 0$ the solution will be [11]:

$$x(s) = x_0 \cos\left(\sqrt{|k_1|}s\right) + \frac{x_0'}{\sqrt{|k_1|}} \sin\left(\sqrt{|k_1|}s\right) \tag{1.14}$$

$$x'(s) = -x_0\sqrt{|k_1|} \sin\left(\sqrt{|k_1|}s\right) + x_0' \cos\left(\sqrt{|k_1|}s\right). \tag{1.15}$$

In the linear approximation, the complete beam transfer line can be represented by a single matrix, called the transfer matrix $\mathbf{M}$ and it describes the change of particle coordinates between two locations. This approach allows the piece-wise calculation of the particle's full trajectory, by splitting the machine into separate elements i, finding the matrices for all of these N components $\mathbf{M}_i$ and multiply them all together:

$$\mathbf{M}(s) = \prod_{i}^{N} \mathbf{M}_i(s).$$

The solution of the equations of motion u (where $u = x, y$) of the particles in matrix form can be descried by:

$$\begin{pmatrix} u(s) \\ u'(s) \end{pmatrix} = \mathbf{M}(s) \cdot \begin{pmatrix} u_0 \\ u'_0 \end{pmatrix}. \tag{1.16}$$

In addition to the transverse motion of the particle, there is also motion along the longitudinal direction of the coordinate system. The longitudinal motion can be observed from Hill's equation of motion, which looks like the equations for a simple harmonic oscillator. Consequently, we can expect a quasi-harmonic oscillation of the particle's orbit around the reference orbit. The frequency and amplitude of this oscillation vary depending on the particle's location in the ring and exhibit periodic behavior. This phenomenon is known as particle synchrotron motion or synchrotron oscillation.

1.2.3 Optics functions

Particles perform oscillations around the design orbit known as betatron oscillations. In the Courant-Snyder formalism, the amplitude of the oscillation represented by the trajectory function $x(s)$ in Hill's equation Eq.(1.14) can be expressed in terms of optics parameters as following:

$$x(s) = \sqrt{\varepsilon}\sqrt{\beta(s)}\cos[\psi(s) + \psi_0] \tag{1.17}$$

where $\beta(s)$ is the beta function, also known as the beam envelope function, it represent the amplitude of the beam envelope, the beta function depends on the beam focusing, which varies with the positions along the lattice. $\psi(s)$ is the phase advance which is equal to $\int_0^s \frac{1}{\beta(s)}\, ds$, the initial condition phase is denoted by ψ_0. The constant ε is the emittance, which is proportional to the area $A = \varepsilon\pi$ of the phase space ellipse formed by the particle's potential states of motion at a specific position in the lattice, as shown in Fig. 1.3.

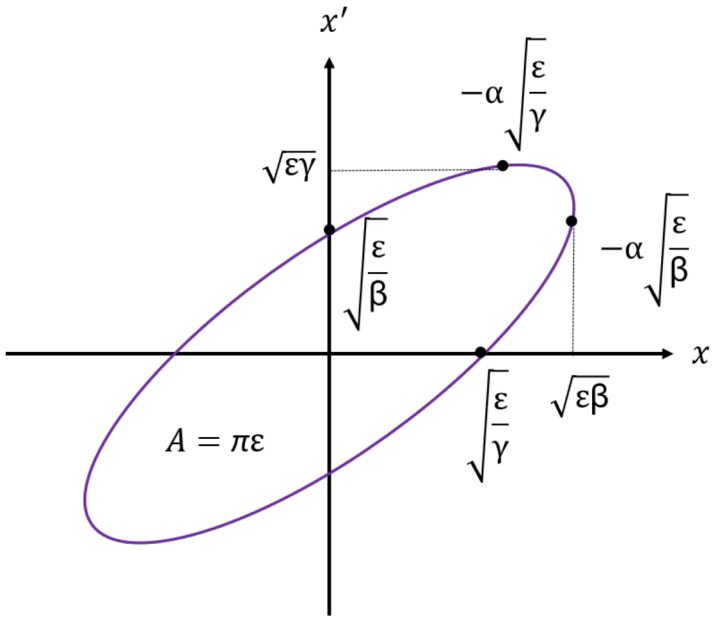

Figure 1.3: Ellipse representing the potential states of a particle in trace space.

The first derivative of the trajectory function in terms of the Courant-Snyder parameters (the formulas are identical for the vertical plane but x' is replaced with y' and the beta function and phase advance are evaluated in the vertical plane) is given by:

$$x'(s) = -\frac{\sqrt{\varepsilon}}{\sqrt{\beta(s)}}[\alpha(s)\cos(\psi(s)+\psi_0) + \sin(\psi(s)+\psi_0)] \tag{1.18}$$

Figure 1.3 shows the beam shape and orientation in the $x - x'$ plane that can also be described using the Twiss parameters β, α and γ by the following ellipse equation [11]:

$$\gamma(s)x^2(s) + 2\alpha(s)x(s)x'(s) + \beta(s)x'^2(s) = \varepsilon \tag{1.19}$$

where $\alpha(s) = -\beta'(s)/2$ is proportional to the correlation between x and x' and indicates the orientation of the ellipse in the phase space, $\gamma(s) = \frac{1+\alpha^2(s)}{\beta(s)}$ is a measure for the divergence of the beam.

The phase space ellipse of the beam is deformed by bending and focusing elements, and the transverse rms beam size is:

$$\sigma(s) = \sqrt{\varepsilon\beta(s)}. \tag{1.20}$$

Betatron tune and resonances

The number of betatron oscillations in one revolution of the particles around the reference orbit can be obtained by dividing the phase advance of the whole accelerator lattice of circumference L_o by 2π and this quantity is known as the betatron tune Q [12]. The tune is one of the most important parameters in circular accelerators since it has strong impact on beam dynamics as will be explained later.

$$Q = \frac{\psi(L_o)}{2\pi} = \frac{1}{2\pi}\oint_{L_o}\frac{\mathrm{d}s}{\beta(s)}. \tag{1.21}$$

Since the tunes are determined by the betatron motion, the focusing/defocusing quadrupoles have a major influence on the tunes values.

It is critical to keep the horizontal and vertical tunes away from specific values; otherwise, resonance may cause the oscillation amplitude of the particles to grow rapidly, leading to beam blow-up or particle loss into the machine aperture. Resonance condition are described by [13]:

$$mQ_x + nQ_y = p \tag{1.22}$$

where $(m, n, p \in \mathbb{Z})$ and $|m| + |n|$ is the resonance order. The tunes integer part is mostly irrelevant, but the fractional part of the tune should be kept away from low-order rational numbers, notably 0, $\frac{1}{2}$, $\frac{1}{3}$, and $\frac{1}{4}$.

The tune diagram shown in Fig. 1.4 is a convenient way to map out the unstable tune areas. This diagram shows the so-called tune space for an accelerated particle beam. The colored lines indicate resonances in tune space to be avoided. The dot represents a possible stable area (working point) where neither horizontal nor vertical tunes are near a resonance line.

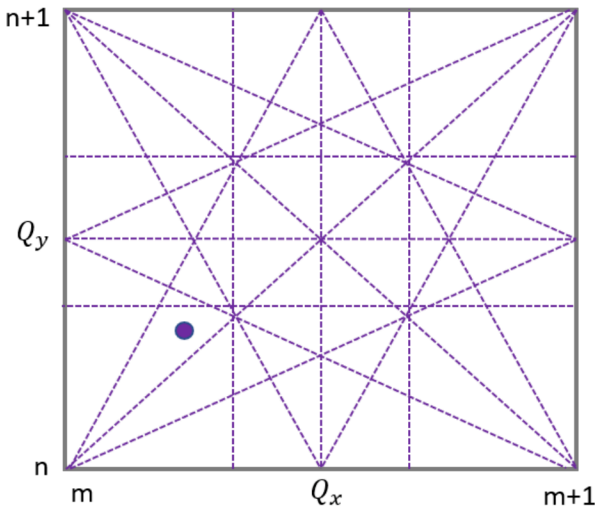

Figure 1.4: Tune diagram with resonances up to third order. The horizontal axis corresponds to the fractional part of the horizontal tune, and the vertical axis corresponds to the fractional part of the vertical tune. The lines show where the values of the tunes satisfy the resonance condition.

Dispersion

As mentioned earlier, in real situations, the particle beam dose not follow exactly the designed machine orbit; moreover, the beam is never quite mono-energetic and includes a finite distribution of particle energies. These deviations of particle energies from the ideal design energy cause perturbations in the solutions of the equations of motion even in the absence of magnet strength and alignment errors.

When a beam of charged particles pass through a dipole magnet, the particles are separated based on their momentum (the dipole works like an energy filter) as seen in Fig. 1.5 and each particle's positions is given by:

$$x(s) = D(s)\Delta \boldsymbol{p}/\boldsymbol{p_0} \tag{1.23}$$

where $D(s)$ is the dispersion function which is a function of position along the accelerator.

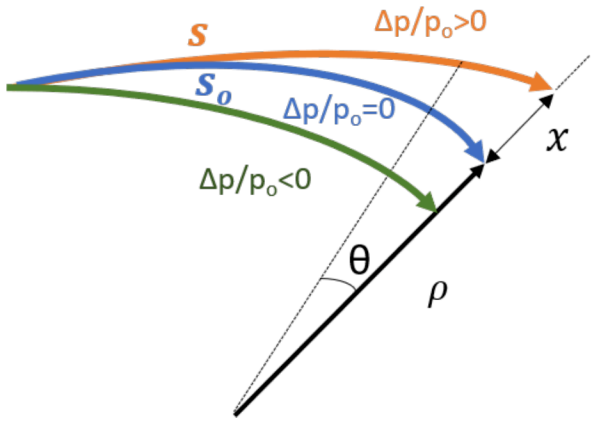

Figure 1.5: Dispersion can create a spread in transverse position of particles of different energies.

The solution of the equation of motion Eq.(1.12) can be considered now as a sum of the homogeneous (on-momentum) and the in-homogeneous (off-momentum) equation solutions:

$$x(s) = x_H(s) + x_I(s).$$

In that way, the equation of motion can be split in two parts [14]:

$$x''_H + k_1(s)x_H = 0, \quad x''_I + k_1(s)x_I = \frac{1}{\rho(s)}\frac{\Delta p}{p}. \tag{1.24}$$

Using the dispersion function expression in Eq.(1.23) we can also define the dispersion equation:

$$D''(s) + k_1(s)D(s) = \frac{1}{\rho}. \tag{1.25}$$

As will be clarified later in Sec. 3.1 , vertical dipole errors and a non-zero vertical closed orbit in the quadrupole magnets will directly introduce vertical dispersion and a non-zero vertical closed orbit through the sextupole magnets, vertical sextupole misalignments, or rotational misalignments of the quadrupoles will couple the horizontal and vertical dispersion planes.

Chromaticity

Similar to the dispersion concept we can examine particles beam with momentum deviations as it pass through quadrupole magnets. Due to these momentum deviations, the beam experience magnetic focusing errors, resulting in different focal points through quadrupoles. This phenomenon leads to a blurring of the beam spot and the quantity expressing this is known as the chromaticity [15]. In linear lattice we can define the natural chromaticity function Q' as:

$$Q' = \frac{\Delta Q}{\Delta p/p_0} = \frac{1}{4\pi} \oint k_1(s)\beta(s)ds \tag{1.26}$$

Fig. 1.6 shows the dependence of the quadrupole focusing strength on the momentum of the particle, which varies as $\frac{1}{f} \propto \frac{1}{p}$. Although the quadrupoles create positive chromaticity in their defocusing plane, the natural chromaticity is negative; As the beta functions at the quadrupoles reach maximum values in the focusing plane while having minimum values in the defocusing plane, the negative contribution from the focusing plane dominates.

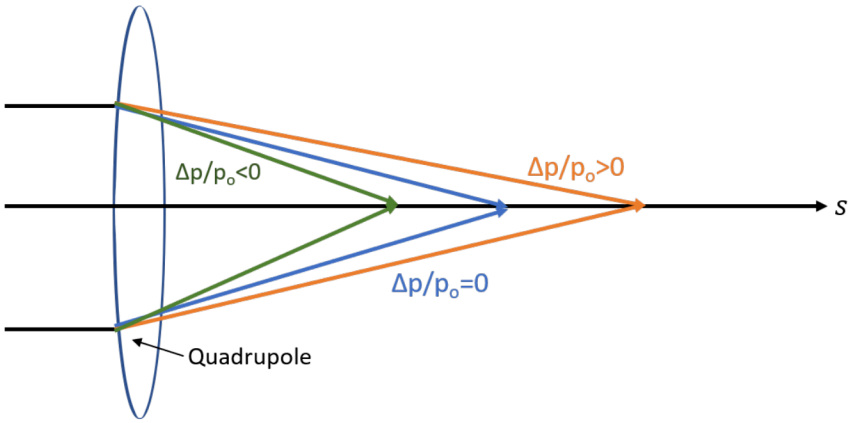

Figure 1.6: Trajectories of particles with different momentum deviations, exhibit different focus points.

Since it acts as a quadrupole error in the machine, the chromaticity leads to a tune spread. With a large tune spread, the particles might encounter optics resonances. Hence, the control of these chromatic effects is crucial [16], [17].

Since a certain energy spread of the beam cannot be avoided, especially in the case of a lepton beam with synchrotron radiation, chromaticity needs to be corrected.

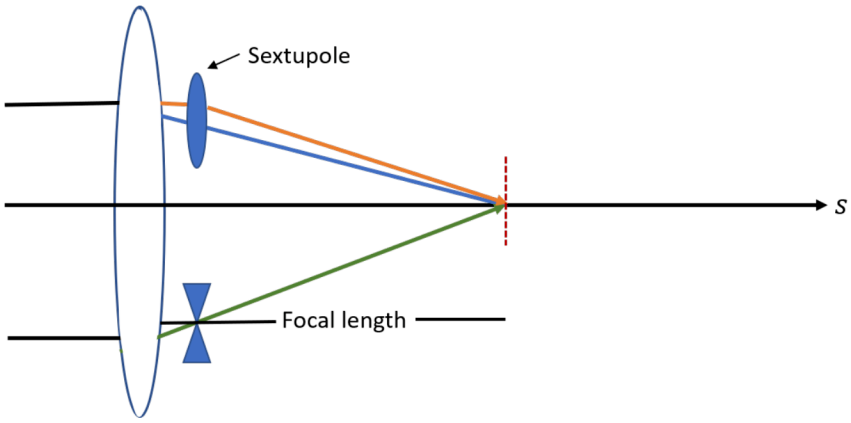

Figure 1.7: Sextupoles through a non-linear magnetic field, correct the effect of energy spread.

Sextupole magnets positioned where the dispersion is non-zero can alter the natural chromaticity to:

$$Q'_x = \frac{-1}{4\pi} \times \oint k_1(s)\beta(s)ds + \frac{1}{4\pi} \sum_{F \text{ sext}} k_2^F l_{\text{sext}} D_x^F \beta_x^F - \frac{1}{4\pi} \sum_{D \text{ sext}} k_2^D l_{\text{sext}} D_x^D \beta_x^D \qquad (1.27)$$

were the first term of the equation represent the natural chromaticity in the horizontal plane and the additional two terms are the focusing and defocusing sextupoles correction values of the first term, k_1 and k_2 are the normalised quadrupoles and sextupoles strengths respectively, l_{sext} is the length of the sextupole magnet, and β and D are the beta and dispersion value at the sextupole location (for a detailed derivation see reference [18]).

The sextupoles used for chromaticity correction are called chromatic sextupoles. Usually two families are used, one horizontal (focusing) and one vertical (defocusing), see Fig. 1.7. In a sextupole a charged particle passing off-center receives a kick proportional to the square of its displacement from the center, i.e. a sextupole acts like a quadrupole with a focusing strength proportional to the displacement of the closed orbit from the sextupole

center. This allows the chromaticity to be corrected because for off-momentum particles the closed orbit is displaced with respect to the reference one by a quantity $D\delta$, where D is the dispersion function and $\delta = \frac{\Delta p}{p}$ is the momentum deviation.

In a periodic FODO lattice (further discussion to follow in Chapter 2) the value of the chromaticity equals approximately the negative value of the betatron tune. For N cells, the total chromaticity is equals to N times the chromaticity of each cell.

Momentum compaction factor

The dispersion orbit of particles with momentum deviation has a different path length than the reference orbit, i.e. particle with $\Delta p/p_o > 0$ travels a larger distance per revolution than the reference particle. Since the bending radii increases with larger particle momentum, the nominal orbit L_0 moves outward of the ring and becomes longer. For particles with smaller momentum, the orbit becomes shorter.

The change of orbit length is proportional to the energy deviation and quantified by the momentum compaction factor α_c. It can be expressed as the derivative of normalized path length difference to normalized momentum:

$$\frac{\Delta L}{L_0} = \alpha_c \frac{\Delta p}{p_0} \tag{1.28}$$

$$\alpha_c = \frac{\Delta L/L_0}{\Delta p/p_0} = \frac{p_0}{L_0}\frac{\Delta L}{\Delta p} = \frac{1}{L_0}\oint \frac{D(s)}{\rho(s)} ds \tag{1.29}$$

1.2.4 Synchrotron radiation and energy loss

Charged particles moving in an accelerator will radiate energy in the form of electromagnetic waves known as Synchrotron Radiation (SR). SR from acceleration in the longitudinal direction is negligible compared to the transverse direction [19].

The total SR power emitted by a relativistic particle with charge q and energy E is [20]:

$$P_\gamma = \frac{cC_\gamma}{2\pi}\frac{E^4}{\rho^2} \tag{1.30}$$

where ρ is the bending radius associated with the bending field $\frac{1}{\rho} = \frac{q}{\boldsymbol{p}}B$ and the constant C_γ is defined as:

$$C_\gamma = \frac{q^2}{3\epsilon_0}\frac{1}{(mc^2)^4} \tag{1.31}$$

where ϵ_0 is the permittivity of vacuum. From Eq.(1.30) we noticed that the radiated power varies inversely with the fourth power of the rest mass m, which means that the radiated SR power increases for particles with small rest mass.

Comparing the power radiated from an electron ($m_e c^2 = 0.511$ MeV) with that from a proton of the same energy ($m_p c^2 = 938.19$ MeV) gives:

$$\frac{P_{\gamma,e}}{P_{\gamma,p}} = \left(\frac{m_p c^2}{m_e c^2}\right)^4 = 1.13 \times 10^{13}. \tag{1.32}$$

It becomes evident that the SR plays an important role for electrons, while for protons and all other heavy particles it can only be observed at energies of at least several hundred GeV.

In circular accelerators it is often important to know the energy loss ΔE_{loss} that a particle undergoes during one complete revolution which can be obtained by the integral of the radiation power for one revolution time T_0. Using $\mathrm{d}t = \frac{1}{c}\,\mathrm{d}s$ and an expression refereed to as the second SR integral [21]:

$$\mathcal{I}_2 = \oint \frac{1}{\rho^2} \tag{1.33}$$

the energy loss per turn is given by,

$$\Delta E_{loss} = \int_0^{T_0} P_\gamma \mathrm{d}t = \frac{C_\gamma}{2\pi} E^4 \mathcal{I}_2. \tag{1.34}$$

In order to reduce the energy losses the bending radius needs to be increased, which is why circular lepton colliders tend to have a large circumference as seen in Fig. 1.13.

Radiation damping

The emission of SR damps the particle oscillations both in the longitudinal and in the transverse planes. This leads to a reduction of the energy spread of the beam and hence to a smaller amplitude of the longitudinal or the synchrotron oscillation. The SR is emitted into the forward direction of the particle movement reducing both longitudinal and transverse momentum. Through Radio Frequency (RF) systems the particle only gains longitudinal momentum, see Fig. 1.8 and as consequence a net loss of transverse momentum is achieved, which leads to a compression of the volume occupied by particles in transverse phase space and to a reduction of transverse emittance.

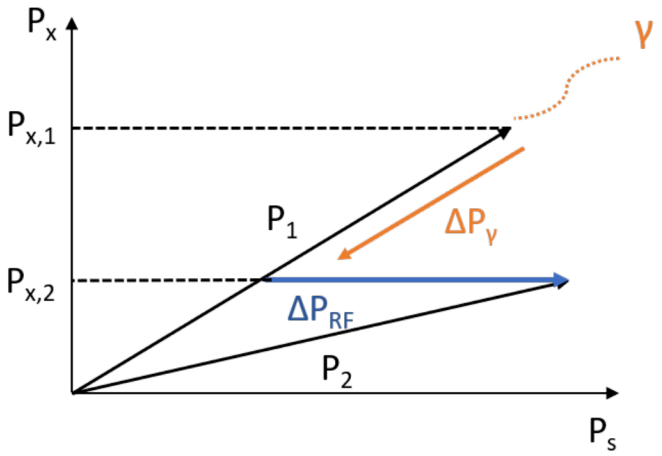

Figure 1.8: Decrease in transverse momentum due to radiation damping. Initially, the transverse momentum $\mathbf{P_{x,1}}$ decreases to $\mathbf{P_{x,2}}$. The emission of a photon (γ) results in a reduction of both the longitudinal momentum $\mathbf{P_s}$ and the transverse momentum $\mathbf{P_x}$ by $\Delta\mathbf{P}_\gamma$. However, the subsequent re-acceleration in the RF cavities ($\Delta\mathbf{P_{RF}}$) only increases the longitudinal component.

The amplitudes of the oscillation A_u are damped exponentially [22]:

$$A_u = A_{u,0}e^{-\alpha_u t}, \alpha_u = \frac{cC_\gamma}{4\pi L}E_0^3\mathcal{I}_2 J_u, \tag{1.35}$$

where, $u = x, y, s$, the parameters α_u are the damping decrements, the damping time t

depends on the initial beam energy E_0, and becomes shorter when SR losses increase and J_u is the damping partition number, which defined using the SR integrals as follows:

$$J_x = 1 - \frac{\mathcal{I}_{4x}}{\mathcal{I}_2}, J_y = 1 - \frac{\mathcal{I}_{4y}}{\mathcal{I}_2}, J_s = 2 + \frac{\mathcal{I}_{4x} + \mathcal{I}_{4y}}{\mathcal{I}_2} \tag{1.36}$$

where $\mathcal{I}_2$ is the second SR integral defined previously in Eq.(1.33), and $\mathcal{I}_{4u}$ is the fourth SR integral and it is given by:

$$\mathcal{I}_{4u} = \oint \frac{D_u}{\rho} \left(\frac{1}{\rho^2} + 2k_1 \right) \mathrm{d}s. \tag{1.37}$$

From the definition of the horizontal equilibrium emittance [23]:

$$\varepsilon_{x0} = C_q \gamma^2 \frac{\mathcal{I}_{5x}}{J_x \mathcal{I}_2}, \tag{1.38}$$

where $C_q = 3.832 \times 10^{-13}$m and $\mathcal{I}_{5x}$ is the fifth SR integral and is given by:

$$\mathcal{I}_{5x} = \oint \frac{\mathcal{H}_x}{|\rho|^3} ds, \quad \mathcal{H}_x = \gamma \eta_x^2 + 2\alpha \eta_x, \tag{1.39}$$

and from Eq.(1.37) we noticed that radiation in focusing quadrupoles, reduces the horizontal damping partition number. This reduction reduces the stability of the horizontal equilibrium emittance.

1.2.5 Dynamic Aperture (DA)

DA is an important parameter for circular accelerators, it is defined as the boundary of the stable area in co-ordinate space for fixed number of turns and it is computed directly via particle tracking. A large DA is needed both for good efficiency of injection of the beam into a storage ring, and for good lifetime of the stored beam. Achieving sufficiently large dynamic aperture is typically one of the biggest challenges in the design of modern light sources, due to strong non-linear dynamics effects.

Nonlinearities may originate from various sources, such as higher-order multipole components in dipoles and quadrupoles, higher-order multipole magnets (sextupoles, octupoles etc.) used to control various properties of the beam as we have discussed in Sec. 1.2.3 and also from effects of fields generated by a bunch of particles on individual particles within the bunch, like space-charge forces, beam-beam effects (Sec. 1.4.2), and many others [24] [25].

1.3 Computer codes

There are many software codes that are used to design and study accelerator beam dynamics e.g, the Methodical Accelerator Design software (MAD-X), X-suite and the Accelerator Toolbox (AT). The following section will introduce the AT code that is used in the tuning simulations described in this thesis.

1.3.1 The Accelerator Toolbox (AT)

Accelerator Toolbox (AT) [26] is a collection of tools that model storage rings and beam transport lines. The original papers of AT were published in 2001 by A. Terebilo [27], [28]. Since then AT proved to be an efficient and flexible tool for interactive accelerator modeling, with ability to:

- Model storage ring.
- Track particles through the lattice, choosing the correct integrator to represent the applicable physics.
- Determine properties of the beam and the influence of lattice parameters on the beam properties.

Lattice manipulation and computation of accelerator physics parameters in AT are provided by two interfaces:

Matlab interface

AT was originally designed to take advantage of the power and the simplicity of MATLAB, (commercially developed environment for technical computing and visualization [29]) since many accelerator facilities extensively were using or planned to use MATLAB. Illustrations of the different options and features AT offers are highlighted in the paper [27].

Python

pyAT is a Python interface to AT [30], first developed in 2019. It uses the "pass methods" defined in AT, implemented by compiling the C code used in the AT "integrators" into a Python extension. These pass methods are used by higher-level functions to provide physics results. PyAT, with its user-friendly interface, free accessibility, and integration of large open-source scientific and plotting libraries in Python, was used for lattice manipulation, beam optics calculations, and particle tracking simulations in this thesis. It also supports the creation of new scripts or the use of existing resources.

1.4 Particle colliders

Particle colliders are type of particle accelerators, in which two beams of particles are accelerated to high energy, circulate in opposite directions and perform high-energy collisions at specified interaction points with a crossing angle. A major advantage of such machines is that when two beams collide head-on, the energy of the particles goes directly into the energy of the interactions between them. When the beams collide, they produce high-energy events, that can be analyzed using detector devices. Secondary particles travel away from the collision point, they can be captured by detector devices that are able to measure their different properties, including positions in space, energy, momentum, mass, and charge. The particles are identified using these information, and entirely new particles could be discovered. Figure. 1.9 shows a schematic layout of the underground civil engineering for the electron positron future circular collider, with respect to the Large Hadron Collider (LHC) [31] and the Super Proton Synchrotron (SPS) [32] at CERN, the in the figure, the different parts of the accelerator including RF systems and detectors are shown.

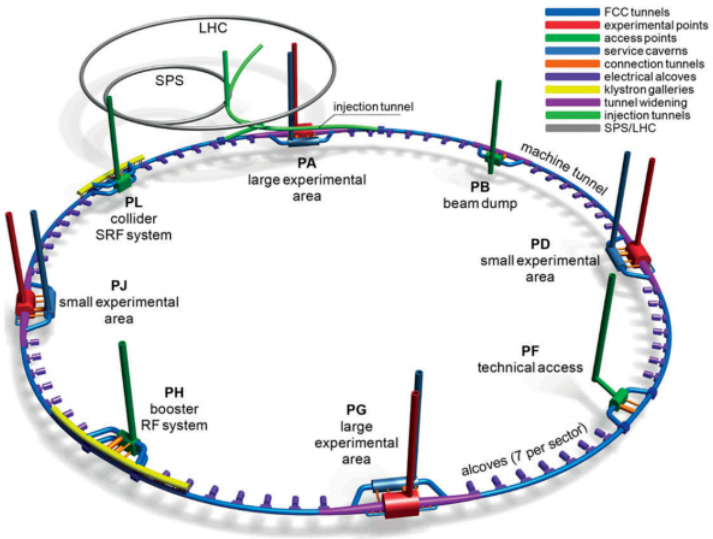

Figure 1.9: A schematic layout (not to scale) of the underground civil engineering for the FCC-ee machine and infrastructure. (Credit: FCC study) [33].

Particle colliders can be either circular, like the FCC-ee and CEPC [34], or linear, like

the International Linear Collider (ILC) [35]. Linear colliders can reach TeV energies, offer easy longitudinal polarization, and have low radiation. Circular colliders, on the other hand, can achieve the highest luminosity at Z/WW/ZH energies but are limited to below 400 GeV energies, as they experience more radiation. Both collider types produce a similar number of Higgs bosons. Circular colliders enable precision electroweak Z and WW physics, while linear colliders extend to higher energies for studying Higgs self-coupling [36].

Particle-antiparticle circular colliders, such as the FCC-ee, are designed with two storage rings that allow beams of the same type of particles to circulate in opposite directions and collide at multiple points. Another notable examples of particles colliders include the LHC at CERN, which collides protons, and the SuperKEKB [37] which collides electron and positron and located at KEK in Japan.

1.4.1 Luminosity

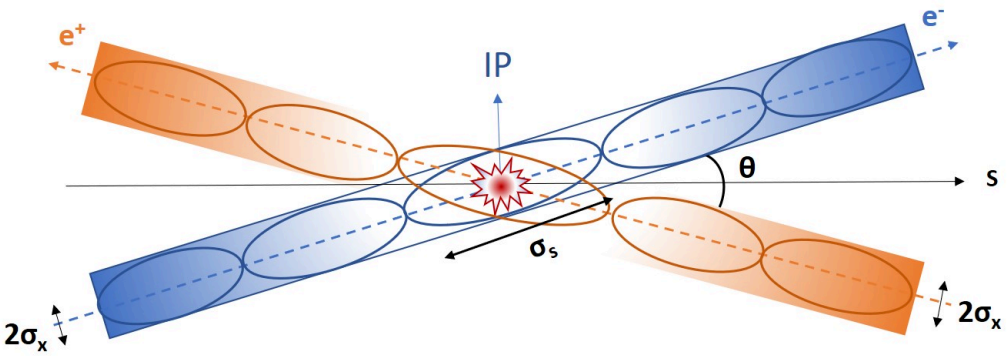

Figure 1.10: Scheme of beam bunches collision with a crossing angle θ.

Particle beam is not a continuous stream of particles but is clustered into "bunches" that may be a few centimetres long and a tenth of a millimetre across, and it may contain about 10^{12} particles (bunch population). Fig. 1.10 illustrates the collision of such particle bunches at cross angle θ, the horizontal and vertical root mean square (rms) transverse beam sizes at the collision point are indicated by σ_x, σ_y, the bunch length σ_s is also indicated in the figure. One of the most important factors that determine the performance of the

colliders is known as the luminosity $\mathcal{L}$, it is a measure of the interaction probability in the colliding beams and comes from the expression of the number of interactions events per second:

$$\dot{N}_{\mathrm{p}} = \sigma_{\mathrm{p}} \mathcal{L}. \tag{1.40}$$

where σ_{p} is the cross-section of the particle reaction. An expression for the luminosity of two colliding Gaussian beams (the amplitude envelope of the beam in the transverse plane is given by a Gaussian function) is given by [38]:

$$\mathcal{L} = \frac{1}{4\pi} \frac{f_{\mathrm{rev}} N_1 N_2}{\sigma_x \sigma_y} S \tag{1.41}$$

f_{rev} is the revolution frequency, N_1 and N_2 are the bunch population of both beams and S is the luminosity reduction factor, it is defined as function of the crossing angle θ for small crossing angles and for $\sigma_s >> \sigma_{x,y}$, as following:

$$S = \frac{1}{\sqrt{1 + \left(\frac{\sigma_s}{\sigma_x} \tan\frac{\theta}{2}\right)^2}} \approx \frac{1}{\sqrt{1 + \left(\frac{\sigma_s}{\sigma_x} \frac{\theta}{2}\right)^2}} \tag{1.42}$$

It may be noticed from Eq.(1.41) that the luminosity increases proportionally with the number of particles per beam, $\mathcal{L} \propto N_1 N_2$ for the two beams. Therefor, in order to produce a high enough rate of events, the vacuum in the rings of the colliders must be particularly good so that the particles can circulate for many hours in the storage rings without being lost through collisions with residual air molecules. The luminosity increases also with reducing the horizontal and vertical sizes of the beam σ_x and σ_y in the collision region. Furthermore, $\mathcal{L}$ is proportional to the frequency with which the beams are fired at one another. Eq.(1.42) also tells us that the luminosity reduction factor for Gaussian bunches colliding under a non-zero crossing angle decreases if the denominator increases, this term is called the Piwinski's angle ϕ:

$$\phi \approx \frac{\sigma_s}{\sigma_x} \frac{\theta}{2}$$

Particle colliders must account for all these factors to achieve high-energy beams and collide them with high luminosity. However, this objective is constrained by numerous other considerations, which will be discussed in detail later on.

Hour-glass effect

Up to this point, we have assumed that the transverse beam sizes remain constant over the entire collision regions. However, since the β-functions have their minima at the collision point and increases with distance, our previous assumption may not always be a good approximation.

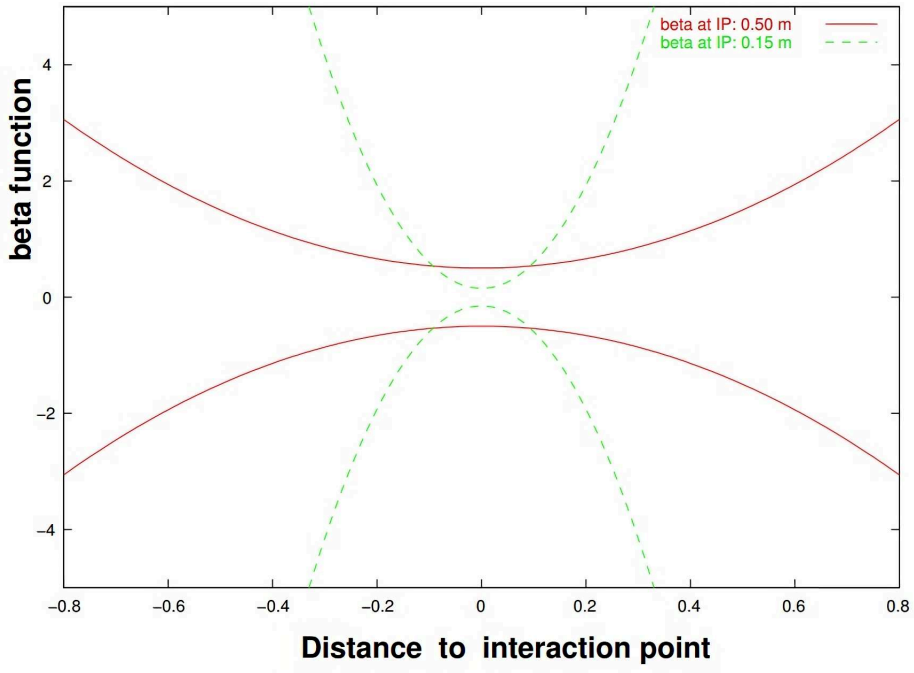

Figure 1.11: Schematic illustration of the hourglass effect where $\beta(s)$ is plotted for two different values of β^* [38].

The hourglass effect, as detailed in Ref. [38], arises due to the fact that the β-function exhibits a parabolic increase with distance from the interaction point, as follows, where β^* is the beta function at the interaction poin:

$$\beta(s) = \beta^* \left(1 + \left(\frac{s}{\beta^*}\right)^2\right) \tag{1.43}$$

Furthermore, the beam size increases approximately linearly with the distance from the interaction point. This is schematically shown in Fig. 1.11 where the functions $\beta(s)$ are shown for two different values of β^* (0.50 m and 0.15 m). Because of the shape of the $\beta(s)$ functions this effect is known as the hourglass effect. Returning to the luminosity expression in Eq.(1.41), we can now rewrite it in a more general form by replacing σ_u with $\sigma_u(s)$:

$$\begin{aligned} \mathcal{L} &= \left(\frac{N_1 N_2 f_{rev} N_b}{8\pi\sigma_x\sigma_y}\right) \frac{2\cos\frac{\theta}{2}}{\sqrt{\pi}\sigma_s} \int_{-\infty}^{+\infty} \frac{e^{-s^2 A}}{1 + \left(\frac{s}{\beta^*}\right)^2} ds, \\ A &= \frac{\sin^2\frac{\theta}{2}}{(\sigma_x)^2\left[1 + \left(\frac{s}{\beta^*}\right)^2\right]} + \frac{\cos^2\frac{\theta}{2}}{\sigma_s^2}. \end{aligned} \tag{1.44}$$

1.4.2 Beam-beam effect and tune shift

In particle colliders, charged particles in one beam exert forces on themselves and on particles in the other beam. These forces are experienced as localised periodic distortions when the two beams cross each other. This beam-beam interactions is considered to be one of the limiting factors of the luminosity, specially for high density beams, (high intensity and small beam sizes), which are the key to high luminosity [39]. When the beam-beam interaction becomes too strong, the beam can become unstable or the beam dynamics is strongly distorted.

Considering a single particle deflected by a Gaussian charge distribution and small orbit offsets, the beam-beam effect is equivalent to an additional quadrupole term, which creates a tune shift. The magnitude of the tune shift depends on the phase advance between the interaction points and the so-called beam-beam parameter, which is often used as a scaling factor to quantify the strength of the beam-beam interaction ($u = x, y$).

$$\xi_u = \frac{N r_0 \beta_u^*}{2\pi\gamma\sigma_u^* \left(\sigma_x^* + \sigma_y^*\right)} \tag{1.45}$$

where β_u^* is the beta function at the interaction point, r_0 is the classical electron radius. The beam-beam tune shift increases for large bunch population N, and small beam sizes. At high energies with large Lorentz factor $\boldsymbol{\gamma}$, the tune shift becomes less relevant. From the luminosity definitions Eq.(1.44) and Eq.(1.45), $\mathcal{L}$, and the horizontal and vertical tune shifts ξ_x, ξ_y, for beam collisions under a horizontal crossing angle θ can be scaled as [40]:

$$\mathcal{L} \propto \frac{N \cdot \xi_y}{\beta_y}; \quad \xi_y \propto \frac{N \cdot \beta_y}{\sigma_x \sigma_y \cdot \sqrt{1+\phi^2}}; \quad \xi_x \propto \frac{N}{\varepsilon_x \cdot (1+\phi^2)} \tag{1.46}$$

In this expression, ε_x is the horizontal emittance. Employing these formulas will address several challenges for colliders, as will be discussed in Sec. 2.3.

1.4.3 Hadron vs. Lepton colliders

Particle colliders can be classified based on main criteria: collider types, center-of-mass energy, and types of colliding beams.

- Collider types: ring-ring, linac–linac, and linac-ring.
- Center-of-mass energy: energy frontiers and particle factories.
- Colliding beams (species): hadron, lepton, photon, lepton–hadron, and photon–hadron colliders.

In this discussion, we will focus on the primary categories of beam particle types, specifically hadron and lepton colliders.

Hadron collider:

This type includes collision of two composite particles, made of two or more quarks held together by the strong interaction, known as hadrons, the collision includes electroweak interactions in addition to the strong interactions. The large number of events generated

from the collision of hadrons allows to study physics observations at highest energies, and also the study of the fundamental properties of matter and the forces that govern them or even search for new particles or phenomena beyond the Standard Model of particle physics.

Lepton collider:

This type of collider includes collision of two point-like particles known as leptons, with only electroweak interactions. Compared to hadron colliders, lepton colliders are used in order to gain better knowledge about already discovered particles and draw conclusions about the properties of new physics and for precision measurements of particles energies and parameters. An example of a lepton collider is the Large Electron-Positron collider (LEP) [41], which put the standard model on solid basis of empirical data by delivering precise measurements of the W and Z bosons. A comparison of various parameters for several lepton and hadron colliders worldwide is presented in Tab. 1.1.

Parameter	**LHC Design**	**LEP2 Achieved**	**FCC-hh**	**SuperKEKB**
Species	pp	e^+e^-	p^+p^-	e^+/e^-
E_{beam}[GeV]	7,000	104	100,000	4/7.007
Current [mA]	584	3.0	500	3.60/2.6
Number of bunches N_b	2808	4	10,400	2500
ϵ_x/ϵ_y [nm/pm]	0.5 / 500	22 / 250	-	1.9 / 4.4/ 8.64/12.9
β_x^*/β_y^* [m/mm]	0.55 / 550	1.2 / 50	1.1	23 /25/ 0.27 / 0.30
L/IP[10^{34}/cm^2/s]	1	0.01	5	0.8
Energy loss / turn [MeV]	0.0067	3340	4.67	1.76/2.43

Table 1.1: Comparison of various parameters for the LHC, LEP2, FCC-hh, and SuperKEKB.

Figure 1.12 shows the so-called Livingston plot that represent the evolution of the particles colliders from the past to the future and the achieved beam energy. It's clear from the plot that the hadron colliders provide highest values for the center of mass energy.

Lepton colliders typically have center-of-mass energies that are an order of magnitude smaller than those of hadron colliders, while lepton-hadron colliders offer intermediate energy values. The peak luminosity and size of various hadron and lepton colliders as a function of center-of-mass energy is represented in Fig. 1.13. The hadron colliders are represented by the blue bubbles, and the lepton colliders by the red bubbles. The semi-transparent bubbles in both cases represent the future colliders that are being suggested. The bubble's size indicates the collider's dimensions (diameter or length). Lepton colliders can be pushed to achieve high luminosity and high energy by increasing the size of the machine as clear from the example of the proposed FCC-ee.

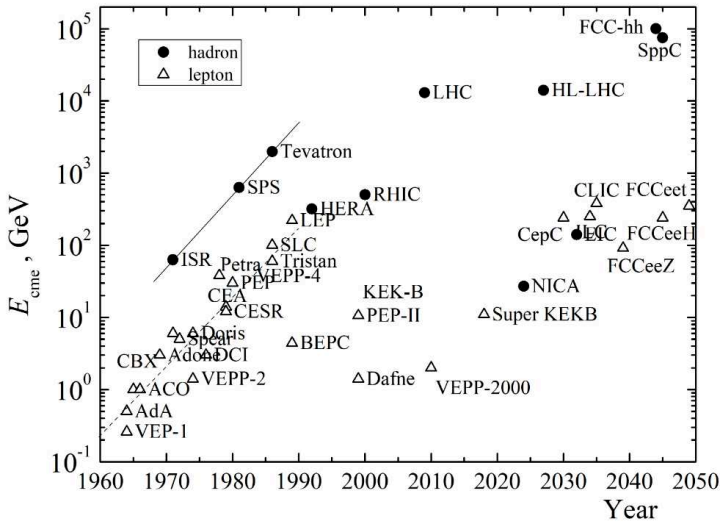

Figure 1.12: Evolution of particles colliders from the past to the future [42].

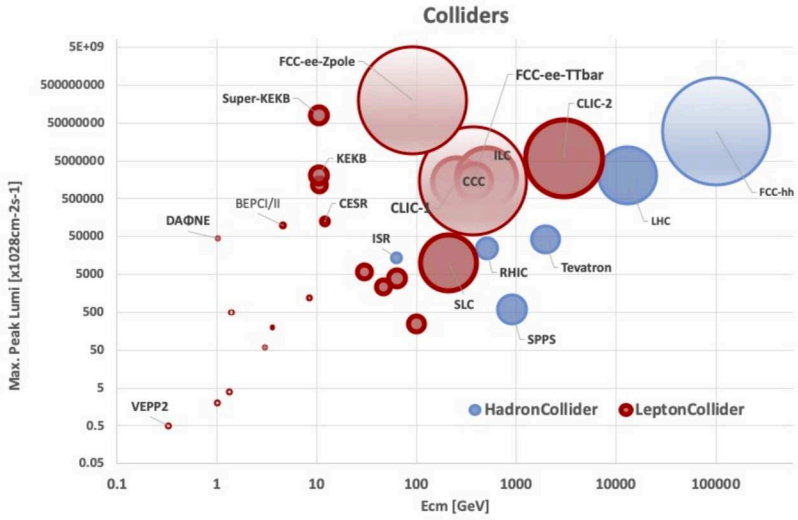

Figure 1.13: Colliders peak luminosity and size as a function of centre-of-mass energy [43].

Chapter 2

The electron positron future circular collider (FCC-ee) and its challenges

2.1 The Future Circular Collider FCC

The Future Circular Collider (FCC) study is developing plans for a new research facility that will host the next generation of higher performance particle colliders, extending the research that is being done at the LHC. The FCC aims to push the limit of the energy and intensity of particle colliders [4], combining research efforts of several international institutes and labs under the leadership of CERN. The timeline of the FCC project is illustrated in Fig. 2.1.

The FCC will offer immense physics potential, being a multi-stage facility at the energy and intensity frontier, it aims to explores three different types of particle collisions: FCC-hh for hadron collisions (involving protons or heavy ions) similar to those at the LHC, that can directly probe the next energy frontier and measure various Higgs couplings, and FCC-ee for electron-positron collisions as in the former LEP, which will achieves the highest luminosity at Z, W, and ZH energies, allowing ultra-precise measurements of the Higgs boson and electroweak parameters, indirectly exploring energy scales beyond the LHC, and other options like proton-electron or proton-heavy ion collisions. The FCC also

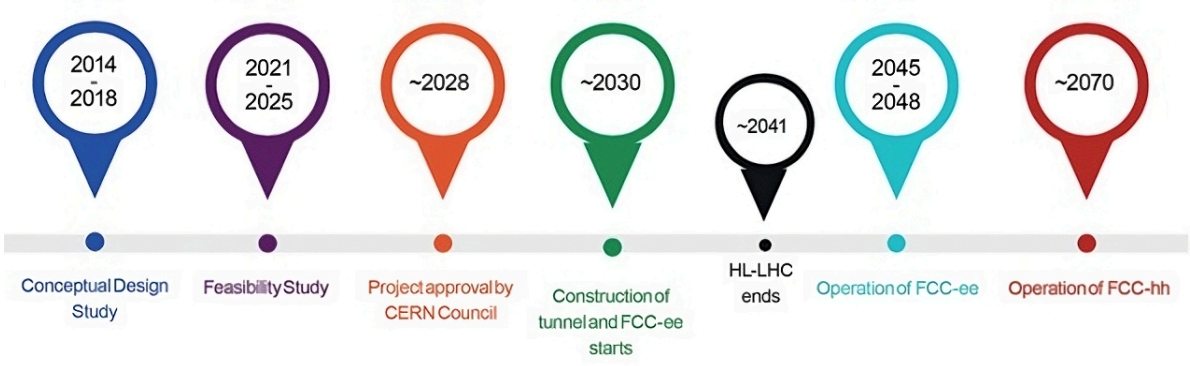

Figure 2.1: FCC timeline from the opening session at FCC week 2024 given by Fabiola Gianotti, director general of CERN: **2014-2018:** Conceptual design study, **2021-2025:** Feasibility study **2028:** Project approval by CERN Council, **2030:** Construction of FCC-ee tunnel, **2041:** HL-LHC ends, **2045-2048** Operation of FCC-ee, **2070:** Operation of FCC-hh [44].

supports heavy-ion collisions and possibly ion collisions. With four collision points, it ensures maximum physics output. The FCC program would foresee first the construction of the FCC-ee, followed by FCC-hh [45] which is proposed to push the energy to 100 TeV centre-of-mass energy. Figure. 2.3 shows the schematic layout of FCC-hh. Some of the main parameters of FCC-hh are presented in Tab. 1.1. The topic of the proposed FCC-hh, is not the primary focus of this thesis.

Figure. 2.2 shows the proposed location for FCC tunnel in the Geneva area with respect to the LHC ring. The circumference is determined by the available dipole magnetic field, which is in the order of 16 to 20 T. The foreseen circumference is therefor in the range of 90 km circumference.

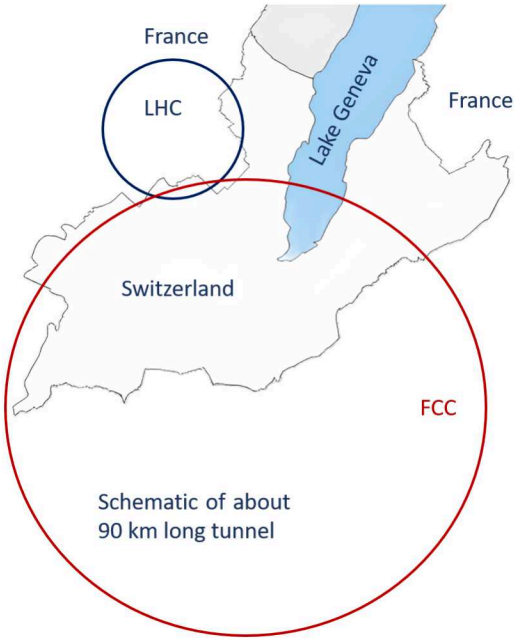

Figure 2.2: FCC footprint location at CERN with respect to the LHC collider.

2.2 FCC-ee optics design and parameters

The proposed FCC-ee is designed as a double ring collider similar to the KEKB accelerator. The schematic diagram of the FCC-ee, as represented in Fig. 2.3 shows the storage rings positioned 1m outside the FCC-hh footprint in the ring arc where the electron and positron rings maintain a 30 cm horizontal separation. The machine will have four Interaction Points (IPs) which are shifted 10.6 m away from the FCC-hh circumference. At two IPs, the FCC-ee beams cross at a 30 mrad horizontal angle. To implement a crossing angle at the Interaction Point (IP), the beam must come from the inner ring to the IP, then the beam will be bent strongly after the IP to merge back close to the opposing ring. Thus, the IP of the rings is displaced towards the outside relative to the hh-beam. Profiting from the crossing angle, a crab waist collision scheme, is adopted [46] (more details are on Section. 2.3.1), this scheme enables an extremely small vertical beta function (β_y^*) at the IPs.

FCC-ee beam energy covers a range extending from the Z (45.6 GeV/beam) to the

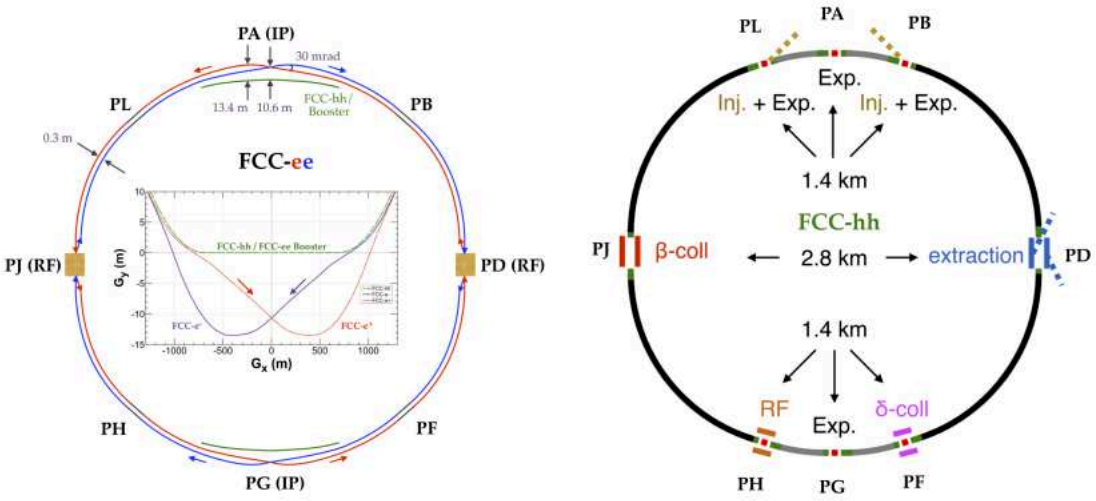

Figure 2.3: Schematics of the implementation of the FCC-ee collider (left) and the FCC-hh collider (right) in the common infrastructure [4].

$t\bar{t}$ production threshold (182.5 GeV/beam). The betatron tune, phase advance in the arc cell, final focus optics and the configuration of the sextupoles are set to the required values at each energy. Another RF system will be installed for the $t\bar{t}$ mode.

As clarified in the schematic layout of FCC-ee Fig. 2.3, experiments are hosted at points PA and PG and each ring incorporates two RF sections located at points PD and PJ. The intermediate straight sections in the middle of the arc can be used for injection, dump and collimation.

The latest table of parameters Tab. 2.1 representing the different parameters values of the FCC-ee different energy modes was published on 15 Nov 2023 [47]. The thesis focuses mainly on the Z energy mode 45.6 GeV, unless specified otherwise. This choice is driven by the higher sensitivity to errors in the Z mode compared to other energy modes, (see the comparison study between Z and $t\bar{t}$ mode in Appendix A.1) making the machine particularly suitable for conducting detailed and robust tuning studies, which can then be applied to other modes. Moreover, other higher energy operation modes come at a later stage in the physics programme of FCC-ee at CERN, thus Z energy lattice analysis has a higher priority.

Parameter [unit]	**Z**	**W**	**ZH**	**$t\bar{t}$**
Beam Energy [Gev]	45.6	80	120	182.5
Number of IPs	4			
Circumference [km]	90.66			
Bend. radius of arc dipole [km]	10.02			
Energy loss / turn [GeV]	0.04	0.37	1.88	10.29
SR power / beam [MW]	50			
Beam current [mA]	1279	137	26.7	4.9
Colliding bunches / beam	11200	1780	380	56
Bunch population [10^{11}]	2.14	1.45	1.32	1.64
Horizontal emittance ε_x [nm]	0.71	2.17	0.67	1.57
Vertical emittance ε_y [pm]	1.9	2.2	1.0	1.6
Arc cell	Long 90/90		90/90	
Momentum compaction α_c [10^{-6}]	28.6/75		7.4/146	
$\beta^*_{x/y}$ [mm]	110/0.7	220/1	240/1	800/1.5
Transverse tunes $Q_{x/y}$	218.158/222.200	218.186/222.220	398.192/398.360	398.148/398.216
Chromaticities $Q'_{x/y}$	0/+5	0/+2	0/0	0/0
Energy spread (SR/BS) σ_δ [%]	0.039/0.109	0.070/0.109	0.103/0.152	0.159/0.201
Bunch length (SR/BS) σ_z [mm]	5.60/15.5	3.46/5.09	3.40/5.09	1.85/2.33
RF voltage 400/800 MHz [GV]	0.079/0	1.00/0	2.08/0	2.1/9.38
Harmonic number for 400 MHz	121200			
RF frequency (400 MHz) [MHz]	400.786684			
Synchrotron tune Q_s	0.0288	0.081	0.032	0.089
Longitudinal damping time [turns]	1158	219	64	18.3
RF acceptance [%]	1.05	1.15	1.8	3.1
Energy acceptance (DA) [%]	± 1.0	± 1.0	± 1.6	$-2.8/+2.5$
Beam crossing angle at IP [mrad]	± 15			
Crab waist ratio [%]	70	55	50	40
Beam-beam ξ_x/ξ_y	0.0022/0.097	0.013/0.128	0.010/0.088	0.066/0.144
Piwinski angle $(\theta_x \sigma_{z,\mathrm{BS}})$ / σ^*_x	26.4	3.7	5.4	0.99
Lifetime (q + BS + lattice) [sec]	10000	4000	3500	3000
Lifetime (lum) [sec]	1330	970	660	650
Luminosity / IP [10^{34}/cm^2 s]	141	20	6.3	1.38

Table 2.1: Parameters of the FCC-ee baseline lattices at various energies [47]

Baseline and local chromatic correction optic lattices

The FCC-ee Conceptual Design Report (CDR) and feasibility study have been based for a few years on the baseline optics developed by Katsunobu Oide (former director of the accelerator laboratory at KEK) in 2016 [48]. These optics have clearly shown that the required performance for the collider can be reached. In 2022, Pantaleo Raimondi (accelerator physicist, currently leader of Fermilab's accelerator project) has developed another set of optics based on different principles as will be explained in the following subsections. The new proposed optics is known as the Hybrid FoDo cell (HFD) or more recently renamed to the Local Chromatic Correction Optic (LCCO). The developments of the two proposed optics with minor modifications are ongoing, at the time of writing the thesis.

Due to the differences between the two sets of optics as clarified in Subsections 2.2.1 and 2.2.2, they cannot share the same hardware or layout in the collider tunnel and underground areas, necessitating a thoughtful selection between the two proposed lattice designs, including comparisons of the physics performance, optics tuning, impact on hardware, process and timeline required by each of the two lattices [49]. Comparison of the optics tuning between the two proposed lattices will be discussed in this thesis.

2.2.1 Arc region

The FCC-ee lattice are designed to have eight arcs, the baseline arc are designed to have 42 arc cell. The transfer arc cell phase advances are 90/90 degrees for the Z energy modes [50], with FODO lengths and phase configurations varying across different energy modes [51].

The optics of the arc region for the baseline lattice rely on a FODO cell structure. The FODO structure consists of alternating horizontally focusing and defocusing quadrupoles (denoted as QF and QD) with bending dipoles in-between. The FODO cell setup provides the most space for dipole magnets that leads to the smallest synchrotron radiation losses for a given machine size and particle energy. In addition. The chosen number of the FODO cells was aimed at achieving the desired horizontal emittance.

Twin aperture quadrupoles with equal lengths for QF and QD are shared between the

electron and positron rings (one aperture for each beam). Additionally, one focusing (SF) and one defocusing (SD) sextupole pair within a supercell of 5 FODO cells will be used to correct the chromaticity [52]. The lattice incorporates "tapering" of all magnets, which locally rescales the field strength based on the local energy along the closed orbit. This approach nearly compensates for orbit excursions resulting from synchrotron radiation losses [51].

The general objectives of developing the LCCO include increasing tolerances on magnet misalignments, achieving larger DA and lifetimes, relaxing tuning requirements, and reducing both magnet power consumption through development of optics solutions that allow/rely on chromatic and harmonic corrections as local as possible [53].

The baseline lattice design incorporates a FODO arc structure, while the LCCO arc optics includes Hybrid FODO (HFD) arc. The arc lattice is periodic over 5 Hybrid-FODO cells, introducing a beta and phase-modulation, and relying on 4 sextupole families. The arc lattice has a phase advance of about 51/44 [54].

Figure. 2.4 offers a view of section of the arc regions for both lattices. The lattice components and optics parameters for the two nominal lattices are illustrated, showing the impact of focusing and defocusing quadrupoles on horizontal and vertical beta functions, along with horizontal dispersion. The FCC-ee baseline lattice includes 1420 arc quadrupoles and 568 arc sextupoles, while the LCCO includes 2168 arc quadrupoles and 1728 arc sextupoles.

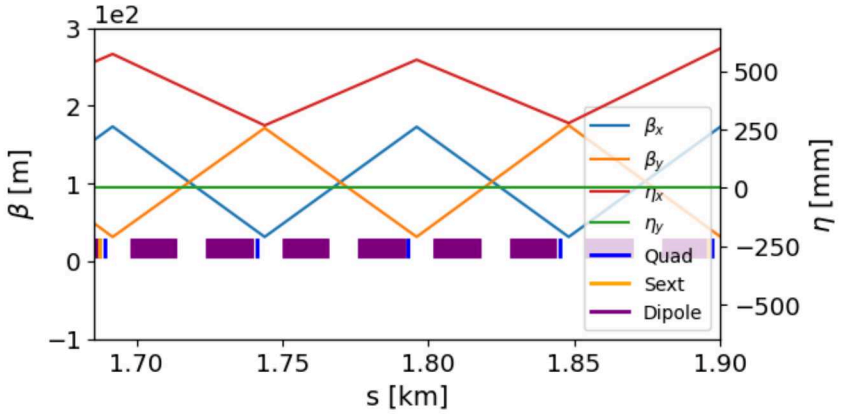

(a) Baseline lattice

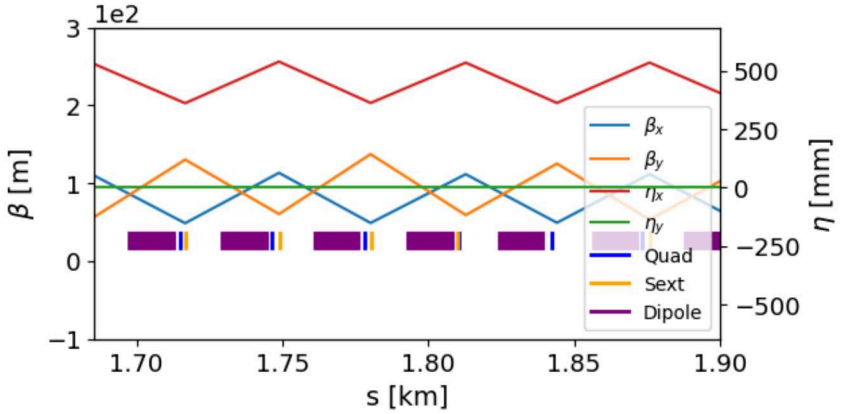

(b) LCCO lattice

Figure 2.4: Section of the arc region indicating the lattice and optics parameters for the baseline and the LCCO lattice. Quadrupoles, sextupoles and dipoles (rectangulars) are shown in blue, orange and purple respectively

2.2.2 Interaction region

To achieve the desired high luminosity for FCC-ee, it is crucial to reduce the beam size at the Interaction Points (IPs), as specified by Eq.(1.41). This reduction can be achieved through strong focusing of the beam (small beta function), as described by Eq.(1.20). This is accomplished by installing strong final focusing quadrupoles in the Interaction Region (IR). Additionally, special attention must be given to chromaticity resulted for the strong quadrupoles, as discussed in [55]. To address this, strong sextupoles are also installed in the IR.

In the baseline lattice, the IR has a Local Chromaticity Correction System (LCCS) (for more details see Ref. [56]) only in the vertical plane at each side of the IP, where two sextupoles separated by phase advance of π are located together with inner sextupole in dispersive region to correct vertical chromaticity [48]. The strength of the outer LCCS sextupoles are set to cancel geometric aberrations and reduced to generate crab waist (to be discussed in Sec. 2.3.1).

The LCCO final focusing system based in correcting the low-beta IP chromaticity in both planes With the need of placing the crab sextupoles in a nearly chromatic-free region which is the final focusing outer ends [57]. Table 2.2 illustrates the main parameters of the LCCO lattice at Z energy (version V22_hfd) [58].

Figure. 2.5 shows the optics function along the elements of the interaction region for the baseline and the LCCO lattices. The baseline lattice has 436 quadrupoles and 64 sextupoles in the IR, while the LCCO lattice IR has 532 and 136 quadrupoles and sextupoles respectively.

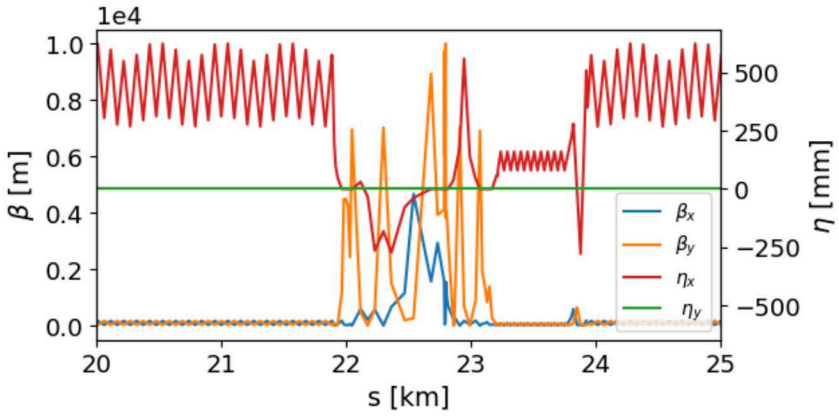

(a) Baseline lattice

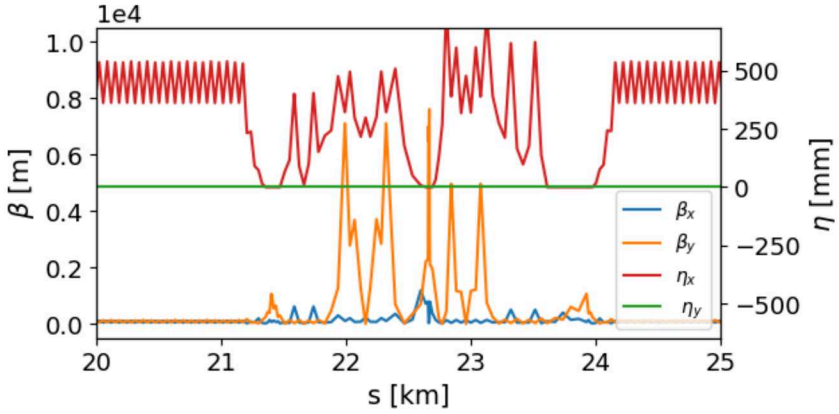

(b) LCCO lattice

Figure 2.5: IR region optics of the baseline and the LCCO lattice. S = 22.79 marks the IP.

Parameter [unit]	**Z**
Beam Energy [GeV]	45.6
Horizontal emittance ε_x [nm]	0.49
Horizontal emittance ε_y [pm]	0.98
$\varepsilon_x/\varepsilon_y$	2.0×10^{-3}
Colliding bunches / beam	10000
Bunch population [10^{11}]	2.43
Beam current [mA]	1280
Momentum compaction α_c [10^{-6}]	23.047
Transverse tunes $Q_{x/y}$	198.20 / 174.30
$\beta^*_{x/y}$ [mm]	150 / 0.80

Table 2.2: Parameters of the LCCO lattice @ Z energy (version V22_hfd) [58]

2.3 Challenges of FCC-ee

In high-luminosity colliders with conventional collision schemes, the key requirements for increasing luminosity include:

- A very small vertical beta function, β_y, at the IP.
- High beam intensity (current).

However, β_y at the IP cannot be smaller than the longitudinal rms bunch size without incurring the hourglass effect (Subsection. 1.4.1) that arises due to the finite bunch length relative to β_y, which causes an increase in transverse beam sizes as one moves away from the IP. For round beams, the hourglass effect reduces the contribution to luminosity from such locations (for more details see Ref. [42]). It is difficult also to increase beam current without exciting (multi-particle effects and multi-bunch effects) collective instabilities (further information on collective effects can be found in [59]).

These problems can be overcome with the crab-waist scheme for beam-beam collisions where a substantial luminosity increase can be achieved without bunch length reduction and with moderate beam currents.

2.3.1 Crab-waist collision scheme

The Crab-Waist collision scheme (CW) was initially proposed by P.Raimondi [60]. This scheme combines the following several potentially advantageous ideas to enhance the luminosity:

- **Large Piwinski angle**

Piwinksi's angle can be increased by increasing the bunch length σ_s, which will allows for an increased bunch population N, In this case, in Eq.1.46 ξ_y remains constant, ξ_x decreases and $\mathcal{L}$ increases proportionally to N [61, 62].

- **Vertical β-function comparable to the overlap area size:**

The vertical β-function at the IP (β_y^*) is set to be comparable to the overlap area size (σ_x/θ) and hence becomes smaller than the longitudinal bunch length, i.e:

$$\beta_y^* \approx \frac{\sigma_x}{\theta} \ll \sigma_s$$

As illustrated in the Fig. 2.6, in the CW scheme, two bunches with small transverse sizes (low emittance beams are essential) collide at large Piwinski angle, hence, the length of the overlap area is much smaller than the bunch length. In this case the vertical beta function at the IP can be squeezed to the length of the intersection area without incurring in the hourglass effect and the luminosity increases [63]. Figure. 2.7 shows the crab-waist sextupoles locations with respect to the IP and the required phase advances.

2.3.2 Beam dynamics challenges

The proposed FCC-ee faces a series of beam dynamic challenges. One of the challenges include the desire of achieving large transverse/longitudinal DA to ensure sufficient beam lifetime and momentum acceptance in the presence of Beamstrahlung and top-up injection [64]. The non-linear dynamics effects, originating from various sources as mentioned in the previous chapter, influence both the longitudinal and transverse motion of the particles. These effects can cause minor changes in beam properties or lead to serious limitations on beam stability. These nonlinearities reduce the DA area, which diminishes beam lifetime and achievable momentum acceptance, ultimately impacting machine performance.

The FCC-ee challenges extend to the need for precise energy calibration and to putting focus on cost and energy efficiency due to the sheer number of components and the large size of the facility [65].

Pushing the β function to its limits in the IP will make the IR highly sensitive to errors in its strong components, reflecting challenges during optics parameter correction/tuning. Alignment of the machine elements is also a major challenge. As a result, we need to carefully study and address these alignment issues and how to correct their effects. Many

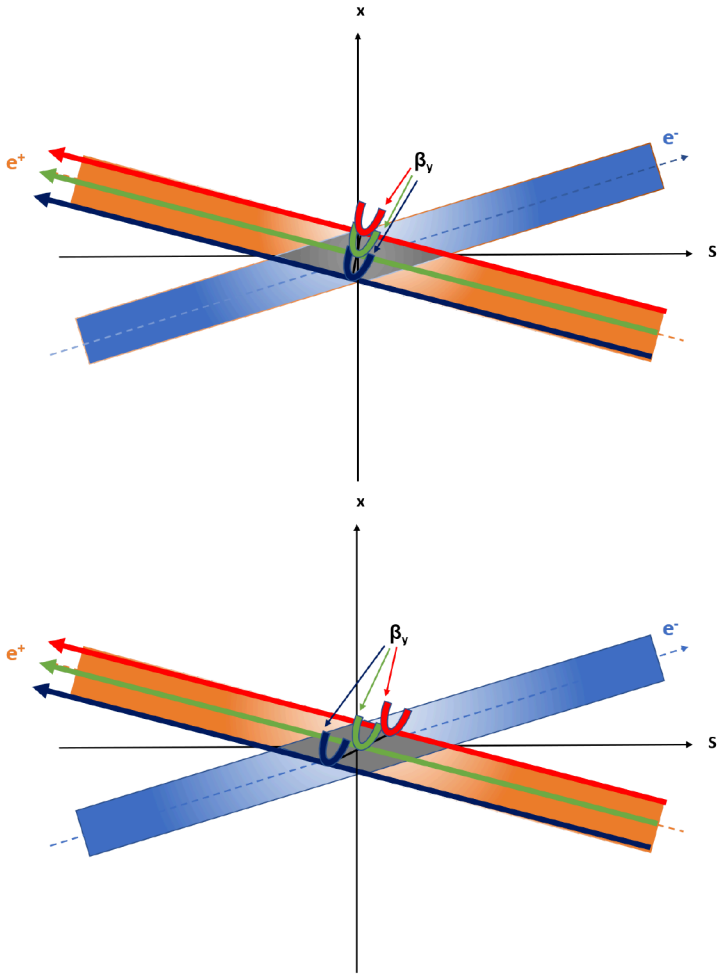

Figure 2.6: Comparison of β-function waist alignment without (upper) and with (lower) the crab sextupole transformation. The waist of the β-functions is aligned to the axis of the other beam via adequate sextupole powering

algorithms for correcting the linear optics have been developed to achieve better optics and DA. Continuous testing and development of various tuning procedures, along with further enhancements of these algorithms, are crucial to ensure new machine can achieve their challenging design parameters. We will outline the impact of element imperfections and discuss some of the developed correction algorithms in the following chapter.

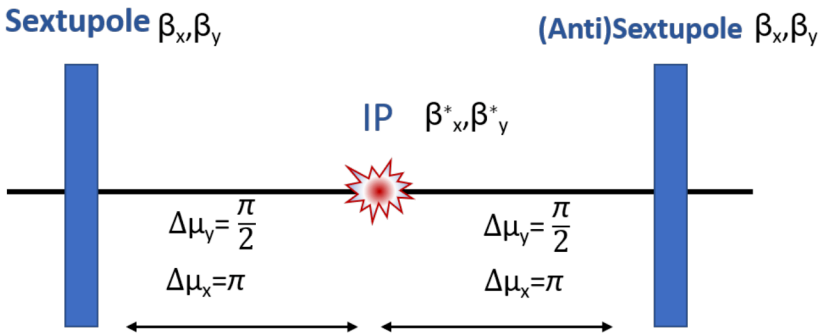

Figure 2.7: Crab waist sextupoles locations and required phase advances from the IP

Chapter 3

Optics measurement and correction algorithms

In preceding chapters, the specifications of the proposed high-performance FCC-ee have been outlined, with its primary goal being achieving remarkable level of high luminosity, by tightly focusing the beam vertically in the interaction regions, along with minimizing vertical beam emittance ε_y. This goal entails achieving low vertical beta functions β_y^* at the interaction point, ranging from 0.7 mm to 1.5 mm, depending on the mode of operation, and a ε_y of 1.9 pm for the Z mode, as specified earlier in Tab. 2.1. When accounting for the various sources of emittance growth, beam-beam effects are budgeted to contribute 1.2 pm to the vertical emittance [66], [67]. Therefore the vertical emittance to be achieved in simulations excluding beam-beam effects is 0.7 pm. Aiming for such an exceptionally low target vertical emittance highlights the necessity for a comprehensive understanding of tolerance requirements regarding magnet field imperfections and misalignments of accelerator components; since the vertical beam emittance without collision is strongly dominated by these imperfections which has impact on the machine performance.

Since the existence of strong focusing synchrotron accelerators and the development of strong focusing theory in 1957 [68], the measurement and correction of charged particle beam optics have been significant concerns. These concerns have continued through decades of research on accelerator linear optics measurement and correction techniques [69],

and numerous techniques have been developed and tested over many years to address this challenge effectively.

While alignment teams can achieve high precision of accelerator components alignments to the nanometre scale [70] and magnet designers can achieve high field quality [71], even small misalignments and field errors can introduce vertical dispersion and coupling of motion between the horizontal and vertical planes, causing the vertical emittance to increase. Additionally, other sources such as residual beta-beating, introduced by magnet misalignments and field errors, along with beam-beam effects, are expected to contribute to the growth of vertical emittance.

This chapter explores the origins of various misalignments and field errors, their impact on beam optics parameters and machine performance, and introduces concepts such as beta-beating, orbit distortion, and coupling. Furthermore, we discuss a group of orbit and optics correction techniques in the latter part of this chapter. These techniques, using different types of correctors placed based on magnet design specifications, include Singular Value Decomposition (SVD) and Dispersion-Free Steering (DFS), as well as k-modulation and multi-turns. Furthermore, we explore the LOCO method, which uses a comprehensive model of the machine to achieve effective optimization and correction.

3.1 Sources of imperfections and their impact on machine performance

Misaligned magnets are the prime source of imperfections on the machine and the major reason of beam optics degradation. It is required to ensure that element's alignment are precised, this process implies a precise measurements of the magnetic axis in the laboratory with reference to the element's alignment markers used by the survey group and precise on-site alignment (position and angle) of the element in the tunnel.

Magnets can be transversely displaced (shifted) in the x or y directions, and they can also be shifted longitudinally along the s axis. Magnets can also be rotated about the x,y, or s axes Figure. 3.1 illustrates different types of magnets rotations. Three cases of

rotations commonly known as the tilt (right), pitch (middle) and yaw (left) are shown. The tilt is a rotation around the s-axis, the pitch is a rotation around the x-axis and the yaw is a rotation around the y-axis.

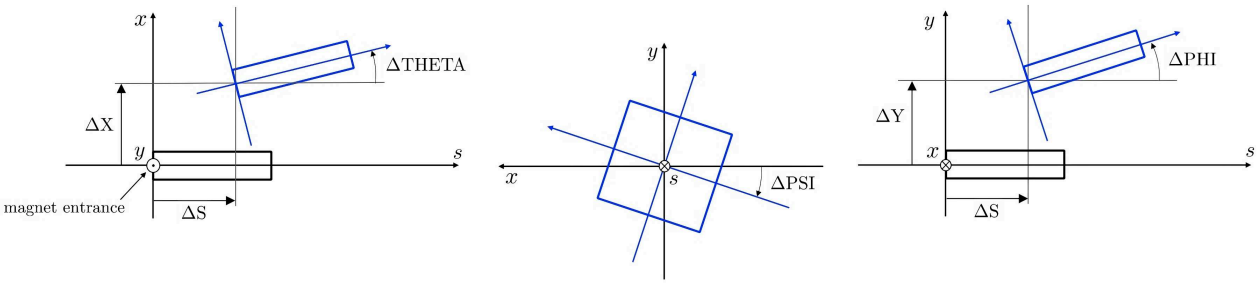

Figure 3.1: Illustrations of different types of magnet rotation misalignments [72].

Another class of imperfection is caused by magnets gradients errors, where the magnet field may differ from the design value and may vary with time, this happen for example when a power supply delivers a very high or very low current. A focusing quadrupole that excited too strongly, will focus the particles to a point closer to the quadrupole causing the beam optics and tunes to differ from the design values.

Other sources of imperfections that affects the machine could come from power supply calibration, fringe fields or in the case of low-energy beams, the earth's magnetic field. Multipoles imperfections can be either linear when the imperfection source is dipole or quadrupole, or non-linear when higher order multipoles are considered. As a consequence of multipole misalignments, field errors corresponding to a lower-order magnetic field type is generated. For example, a shifted quadrupole generates a dipole field, while a vertically shifted sextupole generates a (skew) quadrupole field error. This effect is commonly described as the feed-down effect.

Feed-down effect

To quantify the feed-down effect caused by imperfection of multipole of order m, we start with the multipole expansion of the magnetic field [5]:

$$B_y + iB_x = B_0 \sum_{m=1}^{\infty} (b_m + ia_m) \left(\frac{x+iy}{R_0} \right)^{m-1} \tag{3.1}$$

where B_0 and R_0 are the reference main field and reference radius respectively. b_m and a_m characterize the magnitude of the multipole component, were b_m describe magnets, which have a vertical field component B_y along the x-axis, known as upright or normal multipoles, whereas the a_m describe magnets which are rolled by $\phi = \pi/m$ and are called skew multipoles.

For magnet of length L, the orbit x' and y' kicks induced from the magnet can be written as:

$$\Delta x' - i\Delta y' = \frac{(B_y + iB_x)\, L}{B\rho} = -\sum_{n=0}^{\infty} \frac{k_n L}{n!} (x+iy)^n. \tag{3.2}$$

where $k_n L = L \left(\partial^n B_y / \partial x^n \right)_{y=0} / B\rho$ for an upright magnet, and $B\rho$ is the magnetic rigidity as described earlier in Subsection 1.2.2.

For a magnet with a single multipole component the kick from Eq.(3.2) simplifies to:

$$\Delta x' - i\Delta y' = \left(\frac{k_n L}{n!} \right) (x+iy)^n \tag{3.3}$$

When this magnet is horizontally displaced by d_x, the kick becomes

$$\begin{aligned} \Delta x' - i\Delta y' &= -\frac{k_n L}{n!} (x + d_x + iy)^n \\ &= -\frac{k_n L}{n!} (x+iy)^n - \frac{k_n L}{n!} \sum_{k=0}^{n-1} \begin{pmatrix} n \\ k \end{pmatrix} d_x^{n-k} (x+iy)^k, \end{aligned} \tag{3.4}$$

where the second equality derives from a binomial expansion of $(x + d_x + iy)^n$. The first term shows that the displaced multipole maintains its intended functionality and moreover all lower-order multipoles $k = 0, \ldots, n-1$ appear.

Consider a horizontally displaced sextupole, with kick given by:

$$\Delta x' - i\Delta y' = -\frac{k_2 L}{2} \left[(x+iy)^2 + 2d_x (x+iy) + d_x^2 \right] \tag{3.5}$$

The first term, proportional to $(x+iy)^2$ describes the sextupole component, the middle term $2d_x(x+iy)$, describes the quadrupole component, and an additional horizontal dipole kick appears in the last term as d_x^2.

A vertically misaligned sextupole causes the particles to be kicked by

$$\Delta x' - i\Delta y' = -\frac{k_2 L}{2}\left[(x+iy)^2 + 2id_y(x+iy) - d_y^2\right] \tag{3.6}$$

The linear term, proportional to $d_y(x+iy)$ is now multiplied by an imaginary unit, which describes a skew quadrupolar field.

Table. 3.1 summarizes the imperfections due to dipole, quadrupole, and sextupole magnets, their impact on the machine parameters and the corresponding feed-down effect.

Table 3.1: Sources and impact of magnets imperfections up to sextupoles

Field type	**Imperfection**	**Error type**	**Impact**
Dipole	Field error	Dipole	Orbit, trajectory distortion energy variation
Dipole	Roll	Dipole	Orbit, trajectory distortion
Quadrupole	Field error	Quadrupole	Tune shift, optics errors
Quadrupole	Offset	Dipole	Orbit, trajectory distortion
Quadrupole	Roll	Skew quad.	Introduced coupling
Sextupole	Field error	Sextupole	Introduced chromaticity
Sextupole	Horizontal offset	Quadrupole	Tune shift, optics errors
Sextupole	Vertical offset	Skew quad.	Introduced coupling

Orbit distortion

As discussed earlier, the shape of the closed orbit and particle positions is determined by the accelerator magnets. The orbit of the ideal particle is known as the design or reference orbit. However, due to previously described magnet imperfections, the closed orbit can deviate from the design value. Small additional dipole kicks, arising from dipole

magnet field imperfections and/or misalignments of higher-order multipoles through the feed-down effect, result in a distortion of the closed orbit. Consequently, particles will no longer undergo betatron oscillations around the design orbit but around a new closed orbit.

The general expression for the horizontal or vertical distorted closed orbit at specific location s in the presence of dipole deflection θ, at location s_0 is:

$$U(s) = \left[\frac{\sqrt{\beta(s)\beta(s_0)}}{2\sin(\pi Q)} \cos\left(\pi Q - \psi(s) + \psi\left(s_0\right)\right) + \frac{\eta(s)\eta(s_0)}{\alpha_c L_o} \right] \theta. \tag{3.7}$$

For the vertical plane, the term $\frac{\eta(s)\eta(s_0)}{\alpha_c L_o}\theta$ is zero because there is no vertical dispersion. Due to the factor of $\frac{1}{2\sin(\pi Q)}$, we can see that if the tune becomes an integer, the argument of the *sin* becomes a multiple of π and Eq.(3.7) becomes undefined and no stable orbit exists. In other words, at each revolution any small dipole error will always kicks the particle in the same direction and at the same phase of its betatron oscillation, and the individual kicks will add coherently leading to an unlimited increase of the amplitude of the particle's transverse oscillation and the closed orbit displacements will grow until the beam is lost. Thus, integer tunes have to be avoided in circular accelerators.

Figure 3.2 show the resulted distortion on the horizontal closed orbit due to applying horizontal random displacement errors distributed via a Gaussian distribution with a standard deviation of 10 μm on the arc quadrupoles of the baseline lattice.

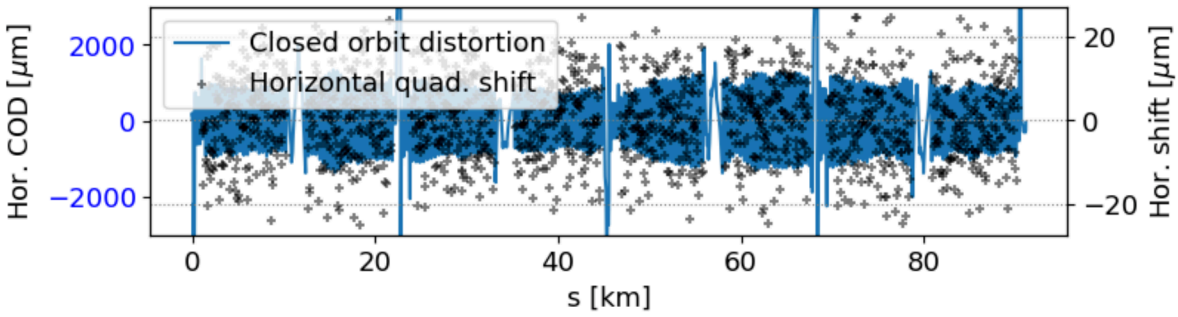

Figure 3.2: Horizontal Closed Orbit Distortion (COD) due to random displacement (shift) errors on arc quadrupoles of the baseline lattice, without applying correction

Beta beating

The imperfections of quadrupoles field components, influences beam optics parameters. Unlike dipole errors which affect orbit displacements, quadrupole field errors alter the focusing properties of the lattice, resulting in a change in the tune. The general expression of this change resulted from a distribution of quadrupole errors δK at location s along the ring is:

$$\Delta Q = \frac{1}{4\pi} \oint \beta(s)\delta K(s)\mathrm{d}s \tag{3.8}$$

Tune shifts in both planes could result also from space-charge, beam-beam effects and electron clouds. From Eq.(3.8) we noticed that quadrupole field errors will induce greater tune shifts at locations with larger beta functions.

In addition to tune shifts, quadrupole field errors will lead to a position dependent change of the beta function, which can be expressed as following:

$$\Delta\beta(s) = \frac{\beta(s)}{2\sin\left(2\pi Q_0\right)} \oint \delta K\left(s_0\right)\beta\left(s_0\right)\cos\left[2\left(\psi(s) - \psi\left(s_0\right) - \pi Q\right)\right]\mathrm{d}s_0 \tag{3.9}$$

Unlike Eq. (3.7), the beta function experiences a significant increase in the presence of half-integer tunes.

The relative change in the beta function in the presence of errors depends on both the beta function at the position of the gradient error $\beta(s_0)$ and the beta function at the measurement position $\beta(s)$. It is known as the beta beating [73]:

$$\frac{\Delta\beta(s)}{\beta(s)} = \frac{\beta(s)_{\text{measured}} - \beta(s)_{model}}{\beta(s)_{model}} \tag{3.10}$$

Figure 3.3 shows an example of the horizontal and vertical beta beating resulting from random relative field errors distributed via a Gaussian distribution with a standard deviation of 10^{-3} applied to arc quadrupoles of the baseline lattice.

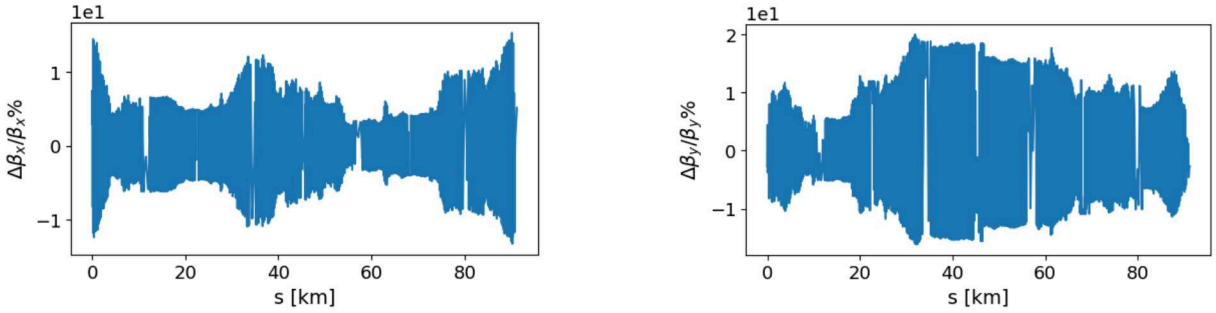

(a) Horizontal beta beating

(b) Vertical beta beating

Figure 3.3: Beta beating results from quadrupole field errors without applying correction

Coupling and vertical dispersion

Another important effect results from magnets imperfections is the betatron coupling between the transverse oscillations in the horizontal and vertical planes. These oscillations can be coupled by magnetic fields of rotated quadrupoles in the x–y plane, solenoids, orbit offsets in sextupoles or vertically misaligned sextupoles. The mentioned imperfections can also couple the horizontal dispersion into the vertical plane, thereby increasing the vertical dispersion. Vertical dispersion can also be introduced by dipole errors and a non-zero vertical closed orbit in the quadrupole magnets.

To improve machine performance, it is crucial to strictly control strong coupling and vertical dispersion, as they lead to emittance growth—particularly vertical emittance, which is typically dominated by alignment and tuning errors that generate vertical dispersion and betatron coupling. Furthermore, the vertical beam size is influenced by the local coupling between the vertical plane and the horizontal and longitudinal planes.

Resonance Driving Terms (RDTs)

The coupling between the planes is not constant around the ring. Consequently, a uniform coupling strength is used to quantify the coupling in a ring and is given by [74–76]:

$$C = -\frac{1}{2\pi} \oint ds k_s(s) \sqrt{\beta_x(s)\beta_y(s)} e^{-\mathrm{i}(\psi_x(s) - \psi_y(s) + i(s/L_o)\Delta} \tag{3.11}$$

where k_s is the s-dependent coupling strength, $\psi_{x,y}$ the horizontal and vertical betatron phase for the uncoupled lattice, L_o is the ring circumference, $\beta_{x,y}$ are the uncoupled beta functions, Δ is the fractional distance from the resonance of the tunes defined in Eq.(1.22):

$$\Delta = Q_x - Q_y - p$$

Using Hamiltonian and normal form theory, Resonance Driving Terms (RDTs) have been defined and it proved to be a powerful tool to describe betatron coupling close to the sum and difference resonance (for detailed derivations of the RDTs see References [77] and [78]).

These terms are functions of the uncoupled lattice parameters at the location of both the coupling elements and the observation point s and is given by:

$$f_{\substack{1001\\1010}}(s) = -\frac{1}{4\left(1 - e^{2\pi i(Q_x \mp Q_y)}\right)} \sum_l k_{sl}(s) \sqrt{\beta_x^l(s)\beta_y^l(s)} e^{i\left(\Delta\psi_x^{sl} + \Delta\psi_y^{sl}\right)}, \tag{3.12}$$

where $k(s)_{sl}$ is the l th integrated skew quadrupole strength, $\beta_{x,y}^l$ are the s-dependent beta functions at the location of the l th skew quadrupole, $\Delta\psi(s)_{x,y}^{sl}$ are the phase advances between the observation point s and the lth skew quadrupole.

A relation detailed in Ref. [12], shows that, in order to minimize the vertical emittance, the driving terms for the two nearest sum and difference resonances, should be minimized. Methods to correct these terms will be explained in the following section.

The global machine coupling can be determined directly using the closest tune approach [74], which is a measurement technique requires moving the transverse tunes close to each other and measuring the minimum distance between the fractional tunes that can be achieved in presence of linear transverse coupling. This distance ΔQ_{min} corresponds to the coupling parameter.

3.2 Orbit and optics correction algorithms

Several correction steps are required to mitigate the impact of magnet misalignments and field errors on machine performance. These steps include orbit and optics corrections, as well as other types of corrections performed by the installed magnets, such as using sextupoles to correct chromaticity. The aim of orbit and optics correction algorithms is to minimize lattice errors by adjusting magnet strengths. The primary goal of these algorithms is to achieve optics parameters that closely resemble the design optics. This helps to recover the dynamic aperture, momentum acceptance, and lifetime, while minimizing emittance and the beta function at the interaction point, thereby enhancing machine performance.

Before looking through the various correction algorithms, let's approach the overall issue as a minimization problem. This approach involves finding optimal values for fitting parameters, such as magnet strengths, to minimize resultant errors. In statistics the goal of minimization is to determine a set of numerical parameter values that yield the most accurate fit of an equation or series of equations to a given set of data (measurements). The minimization approach works for most of the cases in correcting the orbit and optics parameters, as will be explained in the coming sections.

3.3 Orbit Correction

Orbit corrections are achieved through orbit kicks produced by orbit steerers, resembling the impact of dipole errors on the orbit. The steerers kicks' strength are determined by different algorithms. Beam Position Monitors (BPMs) provide essential information about the position of the beam. The accuracy of BPM measurements is critical for achieving a well-corrected orbit. However, like other machine components, BPM measurements have some imperfections. These include measurement offsets due to BPM alignment, scale errors, non-linearity in position readings and other imperfections. Consequently, BPM measurements require calibration. For more details, see References [79] and [80].

Figure. 3.4 illustrates the simplest version of orbit correction for a transfer line where

the beam, represented in red, experiences a kick from a transversely misaligned quadrupole (in blue), and then a steering magnets (red triangles) with strength θ counteract this effect, redirecting the beam to ensure it passes precisely through the center of the BPMs. This approach is known as one-to-one steering in which one orbit reading at BPM is corrected at a time [81].

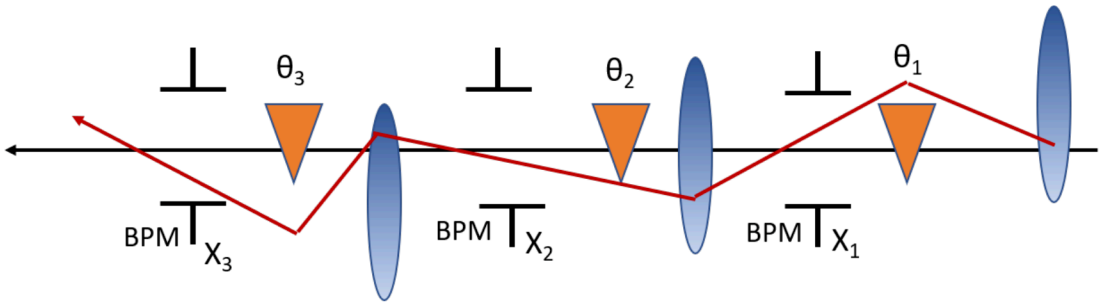

Figure 3.4: Orbit correction via one-to-one steering

Since the closed orbit reacts linearly to the dipole corrector kicks as represented in Eq.(3.7), orbit correction involves generating Orbit Response Matrix (ORM) for the closed orbit as a function of the corrector kicks, the matrix is of dimension $m \times n$, where n is the number of used orbit correctors and m is the number of BPMs.

For the ith BPM and the jth corrector the ORM element is:

$$ORM_{i,j} = \frac{\sqrt{\beta_i(s)\beta_j(s_0)}}{2\sin(\pi Q)} \cos\left(\pi Q - \psi_i(s) + \psi_j\left(s_0\right)\right) + \frac{\eta_i(s)\eta_j(s_0)}{\alpha_c L_o}. \tag{3.13}$$

By defining a column vector B contains m BPM readings and vector θ contains strengths of n corrector magnets:

$$B = (b_1, b_2, b_3, \ldots, b_m),$$
$$\theta = (\theta_1, \theta_2, \theta_3, \ldots, \theta_n),$$

the pesudo-inverse of the ORM can be used to identify correctors powering θ that minimise the orbit at the BPMs B.

Since the ORM is related to orbit responses due to correctors kicks, via the expression:

$$ORM.\theta - B = 0. \tag{3.14}$$

Least squares or weighted least squares [82] arise in this context, since in most cases the ORM is not invertible and also not a square matrix, Eq.(3.14) can only be solved using the least square fit by minimizing the square norm:

$$||ORM.\theta - B||_2. \tag{3.15}$$

This quadratic norm can be minimized by a pseudo inversion and the required correctors powering are expressed as:

$$\theta = (ORM^T ORM)^{-1} ORM^T.B. \tag{3.16}$$

3.3.1 Orbit correction using SVD

The Singular Value Decomposition (SVD) technique [83–85] is used to solve least squares problems more efficiently, especially when dealing with ill-conditioned or singular matrices.

In SVD the ill-conditioned matrix ORM can be decomposed into a product of two orthogonal U, V matrices of dimensions $m \times m$ and $n \times n$ and one diagonal matrix Σ, with non-negative, real eigenvalues on the diagonal $(1/\sigma_{11}, 1/\sigma_{22}, 1/\sigma_{33}, ...1/\sigma_{kk})$. The diagonal eigenvalues σ_{ii}, provide a measure for how ill-conditioned the matrix ORM is. Using SVD, the ORM becomes:

$$ORM = U\Sigma V^T. \tag{3.17}$$

We can define a correction matrix A:

$$A = U^T.\Sigma.V^T. \tag{3.18}$$

The required corrector strengths for a given distorted closed orbit reading can be given by:

$$\Delta\theta = ORM.A.B. \tag{3.19}$$

Small diagonal values in the matrix Σ reflect a strong amplification of orbit BPM reading errors during the calculation of the required corrector strength, making the least squares fit algorithm unstable. It is desirable to limit the number of eigenvalues used for the correction to avoid small eigenvalues that are very sensitive to the accuracy of the model. This can be done by choosing an appropriate cutoff value for the eigenvalues to exclude them from the orbit correction procedure, as illustrated in Fig. 3.5.

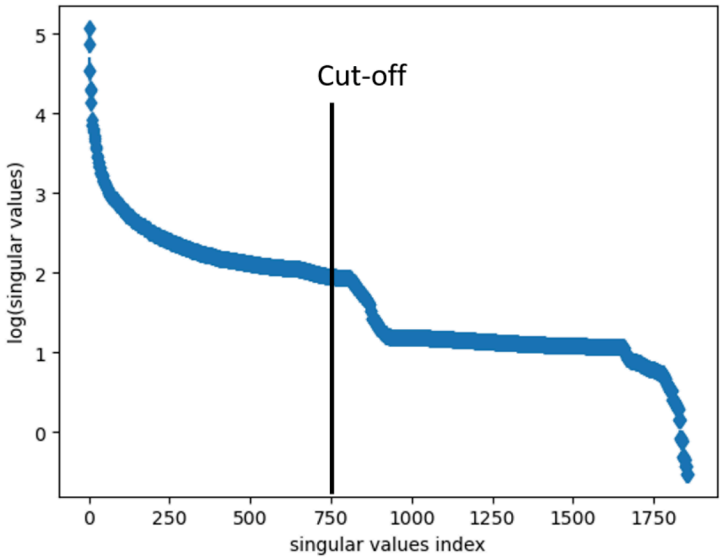

Figure 3.5: Selecting the cut-off of the singular values used for orbit correction, values above 750 will be removed.

In general we can say that orbit correction equation can be solved through the least squares method using the SVD of the ill-conditioned response matrix.

3.3.2 Orbit correction using MICADO

Another algorithm used for orbit correction is known as the Most Effective Corrector Algorithm (MICADO) [86], [87].

MICADO compares the response of every corrector with the orbit to be corrected, by calculating the scalar products:

$$\sigma_j = \sum_{i=1}^{i=m} b_i ORM_{ji} \quad \text{and} \quad \rho_j = \sum_{i=0}^{i=m} ORM_{ji} ORM_{ji}, \tag{3.20}$$

for j correctors. MICADO selects the corrector that has the best correlation with the orbit corresponding to the largest value of σ_j^2/ρ_j. By setting the right kick value $\Delta\theta_j$ to the chosen corrector, it will produce the largest reduction in the quadratic sum of Eq.(3.15). This procedure can be iterated using the remaining correctors until the orbit reach a desired value.

Both MICADO and SVD algorithms have their own distinct advantages and drawbacks. MICADO excels in selecting individual correctors, making it effective for identifying local sources of orbit perturbation in measurements. On the other hand, SVD always utilizes the entire set of correctors, and the number of SVD eigenvalues controls the quality of the correction; limiting the number of eigenvalues limits the influence of BPM noise. Additionally, the simplicity of the SVD correction, which can be represented as a straightforward matrix operation, makes it particularly well-suited for real-time orbit feedback applications.

3.3.3 Dispersion Free Steering (DFS)

One of the techniques to correct horizontal and vertical dispersion is Dispersion Free Steering (DFS). This method involves simultaneously correcting the orbit and dispersion using standard orbit correction algorithms, ensuring a flat orbit while minimizing residual dispersion.

DFS extends the orbit correction method described previously, to account for dispersion at the BPMs. It modifies Eq.(3.14) to incorporates dispersion effects as following:

$$\begin{pmatrix} (1-\alpha)u \\ \alpha\eta \end{pmatrix} + \begin{pmatrix} (1-\alpha)ORM \\ \alpha D \end{pmatrix} \theta = 0, \tag{3.21}$$

where η (vector of length n) represents the horizontal or vertical dispersion at the BPMs, and D is the $m \times n$ dispersion response matrix. The elements D_{ij} represent the dispersion change at the i-th monitor due to a kick from the j-th corrector. The weight factor α shifts the correction from a pure orbit ($\alpha = 0$) to pure dispersion correction ($\alpha = 1$). The optimal α is machine-specific. Applied to Eq.(3.21), a least square algorithm will minimize:

$$S = (1-\alpha)^2 \|B + ORM\theta\|^2 + \alpha^2 \|\eta + D\theta\|^2 . \tag{3.22}$$

For a detailed example of improving emittance using DFS at LEP, refer to reference [88].

3.3.4 Beam-Based Alignment (BBA)

The aim of Beam-Based Alignement (BBA) technique is to find the magnetic centers of magnets using the beam, aiming to determine a golden orbit. This process minimizes the feed-down effect resulting from quadrupole misalignment. Beam-Based Alignment (BBA) for quadrupole magnets has become a standard practice at modern accelerator facilities [89], [90]. BBA can be performed using two approaches. The first approach is model-dependent. In this method, the orbit shift due to a change in the quadrupole gradient is measured, and using a lattice model, the corresponding kick angle at the quadrupole location is calculated. From this, the orbit offset is obtained [91]. The second approach is model-independent. This method aims to find an orbit through the quadrupole where a change in the quadrupole strength does not cause a deflection of the beam orbit. This is achieved by experimentally steering the orbit with a corrector magnet while observing the orbit shift caused by the quadrupole variation at each step [92].

For storage rings with a large number of quadrupoles, like the FCC-ee, the conventional BBA procedure is time consuming, particularly during the commissioning phase, due to the necessary iterative process. Additionally, the conventional BBA method can be affected by strong coupling and the nonlinearity of the storage ring optics. For these reasons, BBA

has not been used in the scope of this thesis. However, it can be noted that some recent studies have presented novel methods to address this issue, such as those based on a neural network [93] or performing parallel BBA for FCC-ee [94].

3.4 Optics measurement and correction

Measuring and correcting the optics parameters such as beta-beating, dispersion, and coupling is crucial, much like orbit correction. Numerous techniques have been developed and tested over many years to address this challenge effectively. These techniques fall into two categories: The first set of techniques, provide beam information without requiring precise knowledge of the accelerator's model, (such as k-modulation in which the strength of individual quadrupoles is modulated to determine the local optics function and the Multi-turn technique, when the beam is excited and multi-turn beam position data is recorded to determine the betatron phase advance between beam position monitors allowing the betatron function to be reconstructed from the phase advance information). The goal of the second group, which includes the orbit response technique, is to create a comprehensive model of the machine, by measuring the ORM with orbit corrector kicks, and a fit to the response is used to reconstruct and correct the machine model.

Detailed explanations of the techniques in these two groups will be provided in this section.

3.4.1 K-modulation

This technique was first documented in 1975 [95]. During the measurement, a single quadrupole gradient variation (current) and the resulted horizontal and vertical tune shifts are recorded, and the average betatron function inside the modulated quadrupole can be determined, as clarified in Eq.(3.8).

The average β function at a quadruple of length L_q, with δK change in its strength and result in $\Delta Q_{x,y}$ tune shifts is given by:

$$\begin{aligned}\bar{\beta}_{x,y}\left(\Delta Q_{x,y}\right) &= \pm\left[\cot\left(2\pi Q_{x,y}\right)\left(1-\cos\left(2\pi\Delta Q_{x,y}\right)\right)\right.\\ &\quad\left.+\sin\left(2\pi\Delta Q_{x,y}\right)\right]\frac{2}{\delta K L_q}\\ &\approx \pm 4\pi\frac{\Delta Q_{x,y}}{\delta K L_q},\end{aligned} \tag{3.23}$$

In $(\pm)$ the $(+)$ and $(-)$ signs correspond to the horizontal and vertical planes respectively (derivations for this relation are presented in [12]).

The K-modulation technique has proven to be a powerful and simple method for effectively measuring average beta functions in a variety of accelerators. For example, it has been successfully applied at the LHC [96]. However, this technique has certain limitations. It requires the quadrupoles to be powered individually, which is a common scheme at synchrotron light sources but less so at large machines like the proposed FCC-ee, where only a subset of quadrupoles may be individually powered due to the high cost of power converters. Additionally, the technique is limited by several factors, including tune measurement resolution, residual betatron coupling, the accuracy of the quadrupole integrated gradient versus current, quadrupole fringe fields, and unwanted tune shifts caused by possible orbit changes at nonlinear magnets during quadrupole modulation.

3.4.2 Multi-turn technique

Multi-turn optics measurements rely on beam excitation over a certain number of turns, typically a few thousand, to obtain sufficient resolution. The collected beam position data provides comprehensive information about the linear optics. For example, the beam oscillation phase, corresponding to the betatron phase ψ at each BPM, is extracted for each BPM. Consequently, the betatron phase advance $\Delta\psi$ between two BPMs can then be determined [97]. An important advantage is that the phase measurement does not depend on the BPM calibration, though it remains sensitive to BPM non-linearities that may bias the phase reconstruction. In addition, exciting the beam with a single kick is often limited by the decoherence of the oscillation (or by radiation damping).

Previous studies have demonstrated that adjusting the phase advance is as effective as correcting the beta functions, providing a powerful numerical method for linear optics correction by minimizing the difference between measured and model phase advances between adjacent BPMs [98]. Equation(3.24) shows that the betatron function can be reconstructed from the phases obtained for three BPMs, assuming there are no sources of errors between those BPMs. For three consecutive BPMs labeled 1, 2, and 3, the measured betatron function at BPM 1, β_1^{meas}, may be obtained with input from the model as [69]:

$$\beta_1^{\text{meas}} = \beta_1^{\text{model}} \frac{\coth\left(\Delta\mu_{12}^{\text{meas}}\right) - \coth\left(\Delta\mu_{13}^{\text{meas}}\right)}{\coth\left(\Delta\mu_{12}^{\text{model}}\right) - \coth\left(\Delta\mu_{13}^{\text{model}}\right)} \tag{3.24}$$

Once the optics data is extracted from the multi-turn data, an optics modelling tool can be used to fit machine errors to the data as following:

From the ideal model, one can obtain the response matrix, $C_{(\text{model})}$, that relates the relative phase-advance $\delta\Delta\psi$, relative horizontal dispersion $\delta\eta_x$ and tune errors ΔQ to the relative strengths δK of all quadrupole, as following:

$$\begin{pmatrix} \delta\Delta\psi_x \\ \delta\Delta\psi_y \\ \delta D_x \\ \delta Q \end{pmatrix} = \mathbf{C}_{(\text{model})} \cdot \delta K, \tag{3.25}$$

and then the SVD method is used to solve this system (similar to the orbit correction as described in Sec. 3.3).

The multi-turn technique has several advantages. It obtains the optics for both planes from two measurements, which can be significantly faster compared to the K modulation method. This method is also not sensitive to BPM calibrations. However, a disadvantage of the multi-turn technique is that the beam must be excited to a sufficiently large amplitude relative to the BPM resolution. While BPM noise is generally not an issue for multi-turn measurements (since it is averaged over many turns), it can be very problematic for single-turn measurements.

3.4.3 Linear Optics from Closed Orbits (LOCO)

While k-modulation and multi-turn techniques offer direct measurements of optics functions, the Linear Optics from Closed Orbit (LOCO) algorithm requires fitting measured data to a model to obtain information about the optics functions. The principle behind LOCO is to leverage the extensive information encoded in the ORM, described in Eq. (3.13).

LOCO has proven to be a powerful and reliable tool for storage rings and synchrotrons since it was established at NSLS by J. Safranek [99–103]. It measures the closed orbit responses to the steering corrector variations matrix and optionally the dispersion function of the machine. The data are then fitted to a lattice model by minimizing the deviation between the model and measured orbit response matrices, $\hat{C}$ and C respectively.

The minimization process involves adjusting parameters to fit the model to the measured data, which is represented by the following chi-square equation:

$$\chi^2 = \sum_{i,j} (C_{i,j} - \hat{C}_{i,j})^2 W_i, \tag{3.26}$$

where W_i is the diagonal weights matrix given by $W_i = \frac{1}{\sigma_i^2}$, and σ_i is the measured noise level on the i-th BPM (variance of input error).

The measured coefficients can be expressed as first-order Taylor expansion of the model coefficients in the fit parameters. Thus, χ^2 is minimized by solving the following equation:

$$C_{i,j} = \hat{C}_{i,j} + \sum_k \frac{\partial \hat{C}_{i,j}}{\partial g_k} \Delta g_k + \hat{C}_{i,j} \Delta x_i + \hat{C}_{i,j} \Delta y_j + \sum_l \frac{\partial \hat{C}_{i,j}}{\partial p_l} \Delta p_l, \tag{3.27}$$

where Δg_k is quadrupole k gradient, Δx_i is the amount by which the reading of monitor i differs from unity, and Δy_j is the scale error of steering magnet j. Additional parameters p_l can be accounted for by numerically determining the derivative $\frac{\partial \hat{C}_{i,j}}{\partial p_l}$ and including parameter variations Δp_l in the fitting procedure.

Fitted parameters

Parameters varied to fit the orbit response matrices in LOCO include:

- Quadrupole gradients
- Quadrupole rolls (skew quadrupole gradients)
- BPM horizontal and vertical calibration
- BPM roll (coupling)
- Steering magnet horizontal and vertical calibration
- Steering magnet rolls
- Energy shifts

Due to the propagation of random measurement noise on BPMs, if all the BPMs were perfectly calibrated, it would be better not to vary the BPM gains in the fit [104].

Solving such system of equations with an iterative approach is a well-known numerical optimization task. The method for solving it will be explained in detail in the next.

Non-linear Least Squares

Least squares fitting minimizes the sum of squared errors between a model and measured data. If the model is linear in its parameters, the minimization can be done in one step by solving a linear matrix equation, as shown in Sec. 3.3. However, if the model is non-linear in its parameters, as in the case for storage rings like FCC-ee to which we will apply the LOCO algorithm, an iterative solution is required. These iterations reduce the sum of the squares of the errors through a sequence of well-chosen updates to the fit parameters. Non-linear least squares fitting aims to match m observations with a model that is non-linear in n unknown parameters, where $m \geq n$ [105], [106]. More mathematical clarification will be given in the next.

Objective function

In fitting a model function $\hat{C}(t;\boldsymbol{p})$ of an independent variable t and a vector of n parameters $\boldsymbol{p}$ to a set of m data points (t_i, C_i), it is customary and convenient to minimize the sum of the weighted squares of the errors (or weighted residuals) between the data C_i and the curve-fit function $\hat{C}(t;\boldsymbol{p})$ known as the objective function:

$$\begin{aligned}\chi^2(p) &= \sum_{i=1}^{m}\left[\frac{C(t_i)-\hat{C}(t_i;p)}{\sigma_{C_i}}\right]^2 \\ &= (C-\hat{C}(p))^\top W(C-\hat{C}(p)) \\ &= C^\top WC - 2C^\top W\hat{C} + \hat{C}^\top W\hat{C}.\end{aligned} \tag{3.28}$$

The weights matrix W is diagonal as mentioned earlier with $W_i = 1/\sigma_i^2$, Such problem is known as weighted non-linear least square method.

Common optimization algorithms for solving nonlinear weighted least squares problems include the Gauss-Newton algorithm and the Levenberg-Marquardt algorithm. To start, we can define the local sensitivity of the function $\hat{C}(\boldsymbol{p})$ to variations in the parameter vector $\boldsymbol{p}$ by the Jacobian matrix $J = \left(\frac{\partial \hat{C}}{\partial \boldsymbol{p}}\right)$.

Gauss-Newton algorithm

The Gauss-Newton (GN) method was the first minimization algorithm adopted by the original LOCO [99]. In this method, the function evaluated with perturbed model parameters may be locally approximated through a first-order Taylor series expansion:

$$\hat{C}(p+h) \approx \hat{C}(p) + \left(\frac{\partial \hat{C}}{\partial p}\right) h = \hat{C} + Jh, \tag{3.29}$$

where, h represents the perturbation to the model parameters.

Parameter update derivation

Substituting the approximation $\hat{C}(\boldsymbol{p}+h) \approx \hat{C}(\boldsymbol{p}) + Jh$ into Eq.(3.28) for $\chi^2(\boldsymbol{p}+h)$ yields:

$$\chi^2(\boldsymbol{p}+h) = \sum_{i=1}^{m} \left[\frac{C\left(t_i\right) - \hat{C}\left(t_i; \boldsymbol{p}+h\right)}{\sigma_{C_i}} \right]^2 = \sum_{i=1}^{m} \left[\frac{C\left(t_i\right) - \hat{C}\left(t_i; \boldsymbol{p}\right) - Jh\left(t_i\right)}{\sigma_{C_i}} \right]^2. \quad (3.30)$$

Expanding the square:

$$\chi^2(\boldsymbol{p}+h) = \sum_{i=1}^{m} \left[\frac{C\left(t_i\right) - \hat{C}\left(t_i; \boldsymbol{p}\right)}{\sigma_{C_i}} \right]^2 - 2\sum_{i=1}^{m} \frac{C\left(t_i\right) - \hat{C}\left(t_i; \boldsymbol{p}\right)}{\sigma_{C_i}} \frac{Jh\left(t_i\right)}{\sigma_{C_i}} + \sum_{i=1}^{m} \left[\frac{Jh\left(t_i\right)}{\sigma_{C_i}} \right]^2. \quad (3.31)$$

Now by using the weighted sum of squares and the transpose notation Eq.(3.31) can be rewritten as,

$$\chi^2(\boldsymbol{p}+h) \approx C^\top W C + \hat{C}^\top W \hat{C} - 2C^\top W \hat{C} - 2(C-\hat{C})^\top W J h + h^\top J^\top W J h. \quad (3.32)$$

The parameter update h that minimizes χ^2 is found from $\partial\chi^2/\partial h = 0$:

$$\frac{\partial}{\partial h}\chi^2(\boldsymbol{p}+h) \approx -2(C-\hat{C})^\top W J + 2h^\top J^\top W J, \quad (3.33)$$

The factor of 2 in the second term on the right-hand side of Eq.(3.33) arises from the chain rule when differentiating $h^\top J^\top W J h$ with respect to h as following:

The chain rule for matrix differentiation states that $\frac{d}{d\boldsymbol{x}}\left(\boldsymbol{a}^\top \boldsymbol{x}\right) = \boldsymbol{a}$, where $\boldsymbol{a}$ and $\boldsymbol{x}$ are vectors. So, for our expression, we apply the chain rule twice:

$$\frac{d}{dh}\left(h^\top\right) \cdot \left(J^\top W J h\right) + \left(h^\top J^\top W J\right) \cdot \frac{d}{dh}(h) \quad (3.34)$$

Now, let's calculate these derivatives:

1. The derivative of $h^\top$ with respect to h is 1 because it's a scalar.
2. The derivative of h with respect to h is the identity matrix, typically denoted as $\mathbf{I}$.
Then, the expression becomes:

$$J^\top W J h + h^\top J^\top W J = 2 h^\top J^\top W J. \tag{3.35}$$

Parameter update formula

In GN algorithm the solution propagates toward the minimum at each iteration by δh_{GN}, which is determined by

$$\left[J^\top W J\right] \delta h_{\mathrm{GN}} = J^\top W (C - \hat{C}), \tag{3.36}$$

$$\delta h_{\mathrm{GN}} = \left[J^\top W J\right]^{-1} J^\top W (C - \hat{C}) \tag{3.37}$$

where $(C - \hat{C}) \approx r_0$ is the residual vector of the previous iteration. The algorithm converges to the global minimum only if the initial guess is already somewhat close to the final solution. SVD is introduced here to solve the matrix inversion $[\left[J^\top W J\right]]^{-1}$ and optics corrections can be performed by applying the differences in quadrupole gradients found through the fitting, with opposite sign to the machine.

The Levenberg-Marquardt algorithm

The Levenberg-Marquardt method, often referred to as LM, also known as the damped least-squares is based on the paper by Moré [107] in combination with the book of Nocedal and Wright [108]. In many cases it finds a solution even if it starts very far from the final minimum. This algorithm adaptively varies the parameter updates using damping parameter λ, and the damped version of Eq.(3.37) reads:

$$\left[J^\top W J + \lambda I\right] \delta h_{\mathrm{LM}} = J^\top W (C - \hat{C}). \tag{3.38}$$

The (non-negative) damping factor λ, is adjusted at each iteration in the following way:

If any iteration happens to result in a worse approximation ($\chi^2(\boldsymbol{p} + h_{\mathrm{LM}}) > \chi^2(\boldsymbol{p})$) and/or the iteration gives insufficient reduction in the residual, then λ is increased. Otherwise, if reduction of χ^2 is rapid and the solution improves, λ is decreased, in this case the LM method approaches the GN method, and the solution typically accelerates to the local minimum. If either the length of the calculated step δh_{LM} or the reduction of χ^2 from the latest parameter vector $\boldsymbol{p}+\delta$ fall below predefined limits, iteration stops, and the last parameter vector $\boldsymbol{p}$ is considered to be the solution [109].

In 1971, Fletcher modified the expression Eq.(3.38) by replacing the identity matrix I with a diagonal matrix made up of the diagonal elements from the transpose of the matrix J times itself $J^\top W J$ [110] as following:

$$\left[J^\top W J + \lambda \operatorname{diag}\left(J^\top W J\right)\right] \boldsymbol{h}_{\mathrm{lm}} = J^\top W (C - \hat{C}) \tag{3.39}$$

The choice of damping parameter λ significantly influences the performance of the LM optimization method. Various strategies exist for selecting an appropriate λ, each balancing local convergence and global convergence considerations. For more details on different approaches to choose the damping parameters, see References [111] and [112].

In conclusion, LOCO is one of the strongest techniques to correct optics errors in accelerators, by finding the proper normal and skew quadrupoles gradient strengths to correct the beta function and the coupling. Including dispersion fitting in LOCO is possible and often beneficial. Fitting the response to steering magnets alone usually results in a model with correct tunes and beta functions, but may not accurately reproduce the dispersion. This discrepancy occurs because beta functions do not vary much with dipole magnet errors around the ring, whereas dispersion does. Additionally, when LOCO is used to correct some gradient error, non-local gradient corrections can fix beta function distortions associated with the gradient error, but not necessarily the dispersion distortion. Including dispersion explicitly as a column in the response matrix ensures that LOCO generates a model reflecting both the beta functions and the dispersion of the real storage ring. This dispersion fitting option is useful for controlling dispersion to achieve low emittance [104].

Today, most synchrotron light sources worldwide routinely perform LOCO. The robustness of LOCO is based on the significant redundancy of experimental data. However,

LOCO is known to be a time-consuming technique. For larger rings such as FCC-ee, fitting thousands of parameters to tens of thousands of data points (consuming hundreds of gigabytes of storage) requires reducing the size of the problem by limiting the number of steering magnets in the response matrix until the desired tolerance is achieved. This reduction, however, limits the amount of information and the minimization accuracy, and is known as reduced-size LOCO.

3.4.4 Coupling correction and vertical dispersion correction

In Section 3.1, we discussed the concept of coupling, its origins, and its significant impact on vertical emittance growth. In order to correct coupling, skew quadrupoles must be installed, primarily at each sextupole magnet. Similar to betatron phase, the coupling matrix can be inferred from multi turn BPM data [113] or orbit measurements [114]. These measurements are analyzed and minimization is applied to determine the appropriate skew quadrupole strength. Another approach to correct the coupling is by minimising $\Delta Q_{x,y}$ (more information in Ref. [12]).

In Eq.(3.12), we sow how coupling can be quantified using the two coupling Resonant Driving Terms (RDTs), known as f_{1001} and f_{1010}, in order to correct these RDTs, (the lower these RDTs, i.e., the coupling, the lower the vertical emittance) the system to invert via SVD reads:

$$\begin{pmatrix} f_{1001} \\ f_{1010} \end{pmatrix}_{\text{meas}} = -\mathbf{M} k_s, \tag{3.40}$$

where k_s is a vector of length n of the integrated strengths of the corrector skew quadrupoles to be determined, f is a (complex) vector containing the measured or computed RDTs at all BPMs, and $\mathbf{M}$ is the (complex) RDT response matrix of size (m $\times$ n).

However, correcting only the RDTs is not sufficient to minimize the vertical emittance, a further correction of vertical dispersion is required (more details in Reference [114]), the skew quadrupoles can also be used to perform this. A more general system to be solved can then reads:

$$\begin{pmatrix} a_1 f_{1001} \\ a_1 f_{1010} \\ a_2 \eta_y \end{pmatrix}_{\text{meas}} = -\mathbf{M} k_s, \tag{3.41}$$

where $\mathbf{M}$ is now a (m $\times$ 2+m) $\times$ n, and $\Delta\eta_y$ is vector of the vertical dispersion distortion at each BPM induced by the skew corrector. The weights $a_2 = 1 - a_1$ are introduced in order to determine the best compromise between correction of dispersion and deterioration of coupling. Their determination is empirical. Coupling correction alone is not sufficient without correcting focusing errors using normal quadrupoles components [115].

Vertical emittance reduction via RDTs correction has been successfully performed at the European Synchrotron Radiation Facility (ESRF) [114].

3.4.5 Summary of Chapter 3

In this chapter, we provide an overview of how machine imperfections, such as incorrect field settings and misalignments, affect linear machine optics. We explore the effects of these imperfections on various magnet types, including dipoles, quadrupoles, and sextupoles, and discuss the resulting observable beam parameters. Additionally, we introduced some global correction techniques, that are mostly based on a response matrix approach, in which matrices containing information of the model in response to a change in model is used to obtain the required magnets strengths in order to restore the nominal machine parameters.

In the upcoming chapter, we will delve deeper into how these machine imperfections impact the performance of the proposed FCC-ee. Additionally, we will analyze the application of correction techniques on perturbed FCC-ee lattices and evaluate their effectiveness in achieving the machine's design performance.

Chapter 4

Optics correction simulations for FCC-ee @ Z mode

In lepton storage rings, the emittance primarily depends on the machine geometry, lattice, and beam energy. Consequently, the smallest emittance achievable is largely determined during the machine's design phase. Reference [116] discusses the considerations and possible modifications involved in designing the FCC-ee lattice to achieve the desired emittance. Nonetheless, during operation, emittance and optics beating, can be corrected within a certain range to achieve the design value using optics correction techniques. Additionally, it is crucial to thoroughly understand the tolerance requirements for magnet field errors, alignments, and large optics tuning simulation campaigns are needed to achieve this.

Tuning simulations for the FCC-ee $t\bar{t}$ lattice at an energy of 182.5 GeV, including a comprehensive correction strategy, were performed using MAD-X [117], [118]. We decided to focus on the Z energy mode because, although both energy modes are challenging to correct, the Z energy mode is more sensitive to errors compared to $t\bar{t}$ as illustrated in the study we carried in Appendix A.1, in which we assigned random horizontal and vertical misalignment errors with a range of rms standard deviations and compared the resulting optics distortion between the Z and $t\bar{t}$ energy modes. The study shows a larger distortion for the Z lattice compared to $t\bar{t}$. For example, Fig. A.4 and Fig. A.5 shows that assigning 1.2 μm errors led to a horizontal closed orbit distortion with a mean value (averaged for

10 seeds) of 80 μm for $t\bar{t}$, while for the Z mode it resulted in a distortion of 260 μm.

As we have mention previously, the higher sensitivity to error of the Z mode makes the machine especially well-suited for detailed and robust tuning studies, which can subsequently be applied to other modes. Additionally, other higher energy operation modes are scheduled for later stages in the FCC-ee physics program at CERN, giving higher priority to Z energy lattice analysis. To include realistic optics measurement scenarios, we carried out tuning studies for FCC-ee @ Z energy that allowed for further analysis, ensuring the effectiveness of the proposed correction strategies for FCC-ee.

In this chapter, we will discuss the error tolerances of the proposed FCC-ee, specifically focusing on the arc and IR magnets alignments errors. We will evaluate the effectiveness of optics and orbit correction methods that we implemented in PyAT through a tuning scheme, aiming to bring the machine optics parameters to acceptable values. This, in turn, improves vertical emittance, DA, beam lifetime, and luminosity. The chapter will explore the iterative modifications we made to our tuning scheme, aiming to optimize it providing a detailed analysis of its evolution.

Moreover, we will delve into specific studies conducted on the FCC-ee's two proposed optics designs, to offer insights into the performance and characteristics of these lattices. A comprehensive benchmarking analysis comparing the performance of commissioning simulations utilizing two computer codes, AT and MAD-X will also be presented. Moreover, the correction algorithms evaluated in more realistic scenarios than the previously conducted work on the $t\bar{t}$ lattice such as including SR and BPM misalignments.

The simulations presented in this chapter are based on the following assumptions:

- Synchrotron radiation effects were excluded from the initial simulations (except for emittance calculations). The effects of SR are considered later in Sec. 4.8.
- Solenoid errors were not included.
- Emittances were calculated for non-colliding beams (i.e. without considering beam-beam effects).

The FCC-ee lattices used in this study are available in the FCC-ee optics and data GitLab repository [119], which contains various lattice designs, including those under development. This repository includes files detailing machine layout, optics, and parameters for each operation mode. Additionally, the CERN optics repository, accessed through the CERN accelerator models website [120], includes all published versions of the lattices along with parameters values. These lattices are available in different formats, including SAD scripts [121] and MAD-x sequence files.

To convert lattice file between different simulation codes, the Xconverters tool [122] [123] was used to convert the sequence from MAD-X format into AT format. By the time this thesis was completed, AT had developed a function that uses the command `at.load_madx` to load MAD-X sequence files and convert them into AT format directly inside AT.

Specifically, we used the baseline lattice at Z energy mode (45.6 GeV), version $V22$, and the LCCO lattice at Z mode, version $79a$ or as defined in the FCC-ee optics repository, version $V22\_hfd$.

The code developed for these studies, along with various examples, has been made available in a GitHub repository [124].

Figure 4.1 presents the nominal DA for the baseline and the LCCO lattice computed at marker "RFR.1" and marker "center" respectively, these elements are in the RF section of the lattices. The DA calculations were conducted with beam sizes of $\sigma_x = 8.84 \times 10^{-6}$m and $\sigma_y = 3.12 \times 10^{-8}$m, particles were tracked over a sufficient number of turns initially without considering synchrotron radiation effects. Incorporating radiation effects in the DA calculation would typically yield a smaller DA area due to increased particle losses resulting from the change in particles energy due to SR, as discussed in Subsection 1.2.4. Nominal DA in presence of SR will be presented in Sec. 4.8.

Figure 4.1 was generated by tracking single particles with varying initial horizontal and vertical amplitudes to determine the stable area - or dynamic aperture, over 1000 turns. If a particle survived the 1000 turns, then the amplitude was increased and the tracking performed again. The procedure searched in radial lines from the origin, in steps of 10-degrees over a 180-degree range. If the particle was lost before reaching 1000 turns, then the search returned to the previous successful step and increased the amplitude with a

smaller step size.

The FCC-ee baseline lattice nominal DA (i.e. without errors or corrections applied) with radiation not included (shown in Fig. 4.1) covers an area range from -20 to 20 horizontally and up to 380 vertically in multiples of the horizontal and the vertical beam sizes respectively, while the DA of the LCCO lattice extends over -30 to 25 in the horizontal plane and up to about 100 in multiples of the horizontal and vertical beam size respectively.

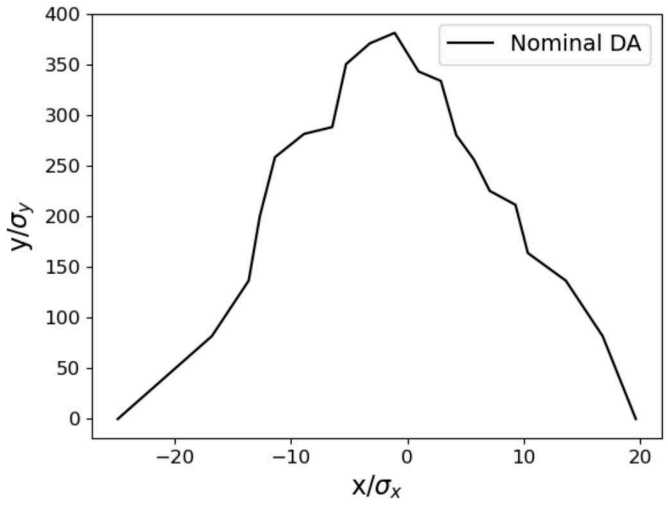

(a) Baseline lattice

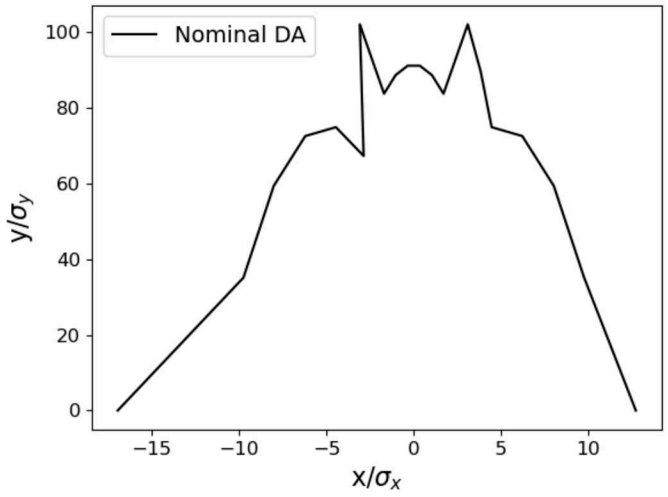

(b) LCCO lattice

Figure 4.1: Nominal DA without synchrotron radiation for a) the baseline lattice and b) the LCCO lattice.

4.1 Correction scheme

The most basic correction procedure, considering our simulation assumptions, is illustrated in Fig. 4.2. We adopted this basic scheme as our foundation. This correction scheme is feasible if nonlinear effects from sextupoles are initially neglected by turning off the sextupoles at the start of the simulation. This is a common approach in the commissioning of 4th generation light sources [125, 126]. After initial orbit correction, the beam lifetime is long enough to start detailed optics corrections steps. We present initial studies using this scheme and explore potential improvements.

In the following subsections, the correction scheme steps are described in more detail.

Installing correctors to the lattice

The FCC-ee proposed lattice designs, that are provided by the FCC-ee Optics Group, are subject to modifications from time to time as the design evolves. Figure. 4.3 illustrates the placement of the corrector elements utilized in these simulation studies for the baseline lattice (similar locations were used for the LCCO lattices). One horizontal and one vertical orbit corrector were installed at every quadrupole. One BPM was also placed at each quadrupole, including the final quadrupole doublets next to the IPs. Skew quadrupole correctors combined with a trim quadrupole are placed at each sextupole in order to correct the coupling and to rematch the vertical dispersion.

In a recent proposal from the FCC-ee Optics Group [127], it was suggested to position the horizontal orbit correctors at the edges of each dipole element, without losing the main dipole field. Vertical orbit correctors are positioned at each quadrupole.

Another proposal involves installing long steerers (∼20 cm) before the quadrupoles and placing BPMs after the quadrupoles (the first quadrupole magnets near the IPs do not have steerers or BPMs) [128]. Although we explored this alternative arrangements of orbit correctors and BPMs, our tuning results did not show significant differences. Therefore, we used the initially mentioned locations for our chosen studies. It is worth noting that these alternative locations could yield different results in other studies.

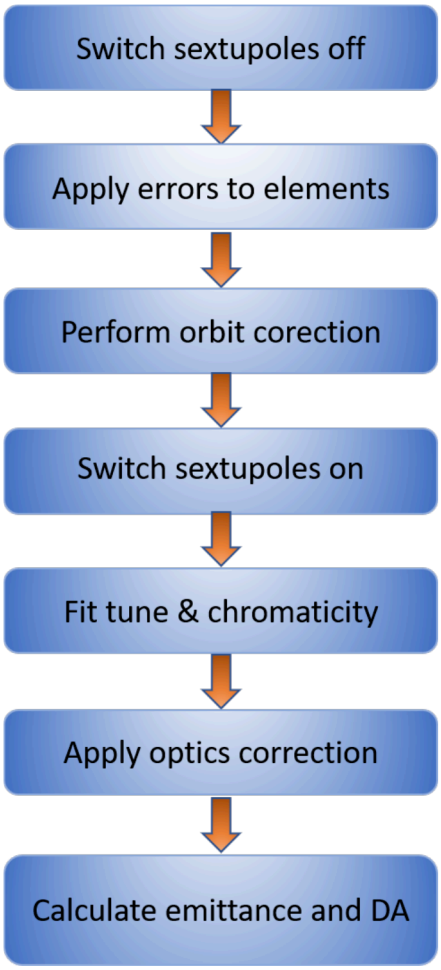

Figure 4.2: Baseline tuning scheme procedure that was later iterated upon and improved.

The total number of each corrector type and the BPMs used for the two lattices are listed in Tab. 4.1.

Switching off sextupoles

The lattice is used with full beam energy 45.6 GeV and the AT function `radiation_off` was used to turn off everything affecting the longitudinal momentum, including the RF cavities and the energy loss from SR.

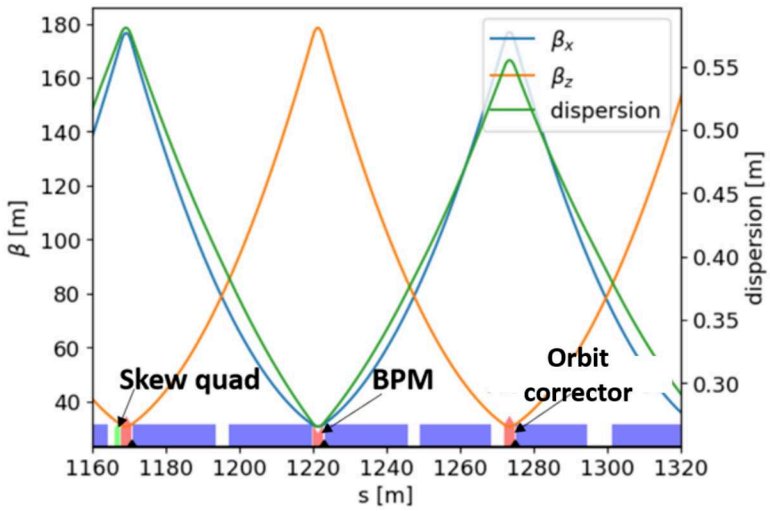

Figure 4.3: Orbit correctors, BPMs and skew quadrupole locations shown over part of the arc region for the baseline lattice. Purple rectangles are dipoles, pink objects are focusing and defocusing quadrupoles, and the orbit correctors, BPMs, and skew quadrupoles are as indicated.

Table 4.1: Number of correctors and BPMs for the baseline and the LCCO lattice

Corrector type	Baseline	LCCO
Hor. orbit	1856	2700
Ver. orbit	1856	2700
Skew quads	632	2000
BPMs	1856	2700

The next step involved turning off all sextupoles. This was done to mitigate strong non-linear effects caused by the sextupole fields and the strong orbit distortions (illustrated in previous chapters), thereby starting with linear lattice that can initially tolerate larger imperfection values. Figure 4.4 illustrates the impact of sextupole fields on deforming the optics parameters in the arc, even when small alignment errors of only 10 μm rms are applied to arc magnets.

Turning off all sextupoles magnets initially is feasible as long as the orbit distortion

does not exceed the vacuum chamber gap and if the distortion does exceed the gap, a first-turn trajectory correction can be applied to achieve a closed orbit inside the vacuum chamber.

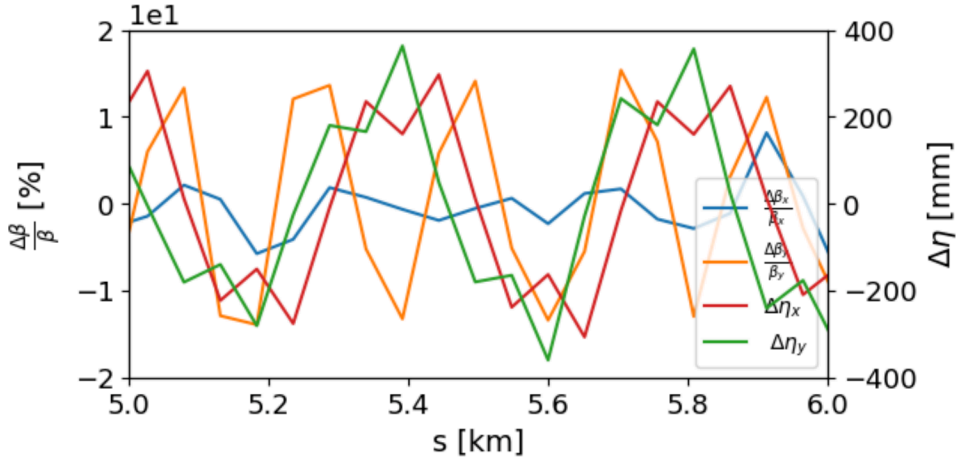

Figure 4.4: Impact of horizontal and vertical random alignments errors with standard deviation of 10 μm applied to arc magnets with sextupoles on. The region shown is one arc.

Sextupoles nonlinear effect on the ORMs

Due to the nonlinear fields generated by the sextupoles, the kick values assigned to orbit correctors for generating ORMs lead to changes in the horizontal and vertical tune values (Q_x and Q_y). Thus the kick values of the orbit correctors need to be chosen carefully, such that it avoid the nonlinear effect of the sextupoles. The relationship between the kicks magnitude and the BPM readings of the closed orbit was generated while sextupoles are turned on by choosing one orbit corrector, assigning a range of kicks values to the corrector and recording the orbit reading at one BPM. The non-linearity between the kicks values and BPM readings of the closed orbit is illustrated in Fig. 4.5. For the baseline lattice, the acceptable range for horizontal corrector kicks lies between -10×10^{-5} radians and 3.75×10^{-5} radians. Similar values were obtained for the LCCO lattice.

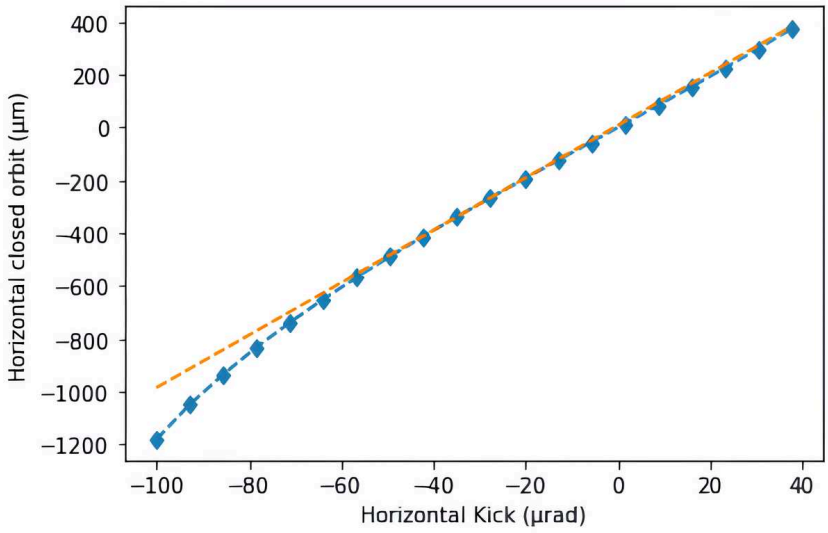

Figure 4.5: The plot shows how the horizontal closed orbit changes with different kick values. The straight dotted orange line represents a linear fit based on the midpoint slope of the data, highlighting the general trend of the orbit distortion with varying kicks.

Applying errors to elements

To apply errors to elements we used the `shift_elem` function that sets the transverse displacement of an element. The translation vectors are stored in the T1 and T2 attributes. While for rotation we applied the `rotate_elem` function that can apply tilt, pitch, and yaw angles to the elements. The rotation matrices are stored in the R1 and R2 attributes, where θ is the element tilt angle:

$$R_1 = \begin{pmatrix} \cos\theta & \sin\theta \\ -\sin\theta & \cos\theta \end{pmatrix}, \quad R_2 = \begin{pmatrix} \cos\theta & -\sin\theta \\ \sin\theta & \cos\theta \end{pmatrix}. \tag{4.1}$$

These transformations are applied by changing the particle coordinates at the entrance of the element and restoring them at the end. For field errors we changed the corresponding polynomial component of the elements or the integrated field parameters K (for quadrupoles) and H (for sextupoles).

In Sec. 4.2, we will conduct a comprehensive investigation into the influence of alignment errors on both the IR and arc components for both lattices.

Orbit Correction

The SVD orbit correction is the algorithm used in this study for orbit correction through the correction scheme. The implemented SVD algorithm utilizes all orbit correctors available along the lattice, ensuring the orbit distortion is minimized in both the horizontal and vertical planes at all BPM locations around the ring. Figure 4.6 shows an example of the SVD correction method implemented to correct the distorted orbit resulting from introducing random horizontal and vertical misalignments with standard deviation of 50 μm on the arc quadrupoles, while the sextupoles are switched off, resulting in reduction of the horizontal orbit distortion rms values from 3152.43 μm to 4.78 μm and in the vertical orbit distortion rms values from 5895.83 μm to 3.88 μm.

In Sec. 4.4, we will analyze the effects of the selected number of eigenvectors on the orbit correction results.

Switching on sextupoles

The orbit correction step helped in achieving stable optics values in terms of the rms orbit and the relative dispersion in the presence of sextupole fields. Now, the sextupole fields need to be switched on again to manage the chromatic effects of the lattice and to dampen the head-tail instability [16]. Therefore, we initially followed orbit correction by setting the sextupole strength to its full design value of 100% in one step. However, further optimization of this correction process revealed improved tuning (resulting in lower beta-beating, lower coupling, smaller vertical dispersion, and ultimately smaller vertical emittance) when incrementally increasing the sextupole strength in steps, interleaved with other necessary corrections, as will be detailed in Sec. 4.4.

At the end of the sextupole ramping process, when the sextupole strengths reach their design values, the partial correction of chromaticity achieved by setting the sextupole

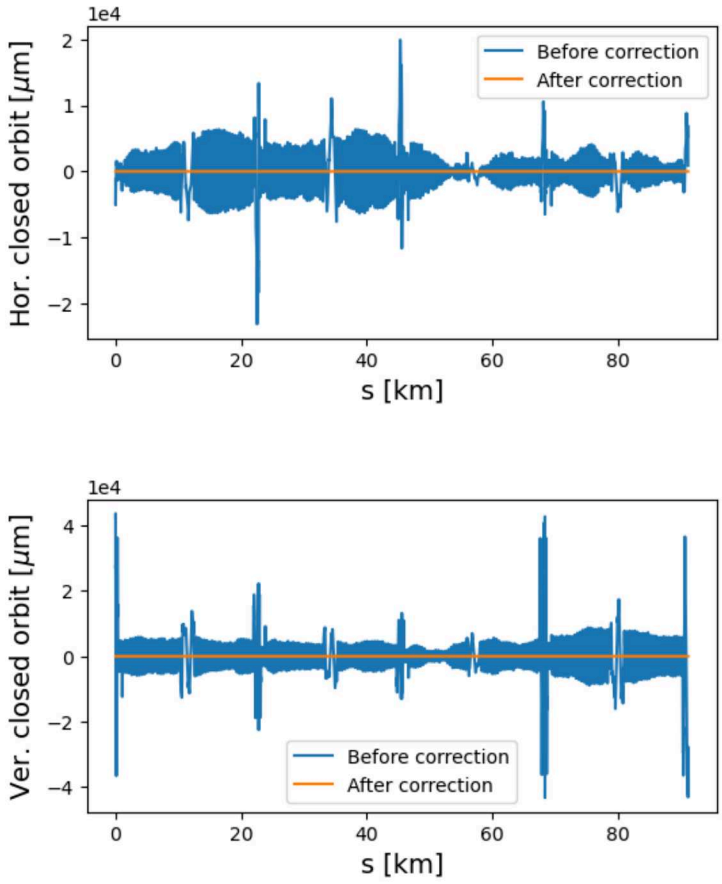

Figure 4.6: Horizontal and vertical closed orbit before and after applying the SVD orbit correction. The correction led to a reduction in the rms value of the horizontal orbit distortion from 3152.43 μm to 4.78 μm and in the vertical orbit distortion rms value from 5895.83 μm to 3.88 μm.

strengths to full value in the presence of alignment and field errors is only a preliminary step. It is crucial to fine-tune the sextupole strengths further to bring the chromaticity as close to the design values before moving on to subsequent correction steps. Additionally, constant adjustment of the tunes through the correction scheme is necessary. Both chromaticity correction and tune correction are vital to avoid resonances and ensure overall

beam stability.

Fitting tune and chromaticity

For tune fitting we used the AT `fit_tune` function that uses an optimization routine to vary the quadrupole strength values until the correct output tunes are achieved. A similar manner is followed by the `fit_chrom` function that changes the sextupole strengths to correct the chromaticity. In this study, all focusing and defocusing arc quadrupoles were used to fit the horizontal and vertical tunes, while all arc focusing and defocusing sextupoles were used for horizontal and vertical chromaticity fitting. Initially, we included the IR magnets in the fitting process, however, they showed poor results. Therefore, we excluded the IR magnets. The arc magnets were used for tune and chromaticity fitting for both lattices.

Optics Correction

At this stage, linear optics correction is performed, including beta beating, coupling, horizontal and vertical dispersion corrections. For optics correction, we utilised LOCO method, and we developed our own implementation of it. The implementation includes numerical calculations of orbit response matrices, Jacobian calculations, and the design of LOCO iterations strategies.

Since the Jacobian calculations are the most time-consuming part of this process, we initially used only 10 horizontal and 10 vertical orbit correctors to generate the ORMs, for both lattices. However, realizing the necessity for more accuracy, we doubled this number to 20 horizontal and 20 vertical orbit correctors distributed evenly around the ring. Figure. 4.7 shows the horizontal and vertical phase advance distribution of the 20 orbit correctors used for the baseline lattice. The Jacobian calculations were executed using parallel processing on a computer cluster and it took approximately one hour in total in the case of the baseline lattice.

Our LOCO scheme began with two iterations of beta beating correction, through adjusting the strengths of all normal quadrupoles, including only the diagonal ORMs in the

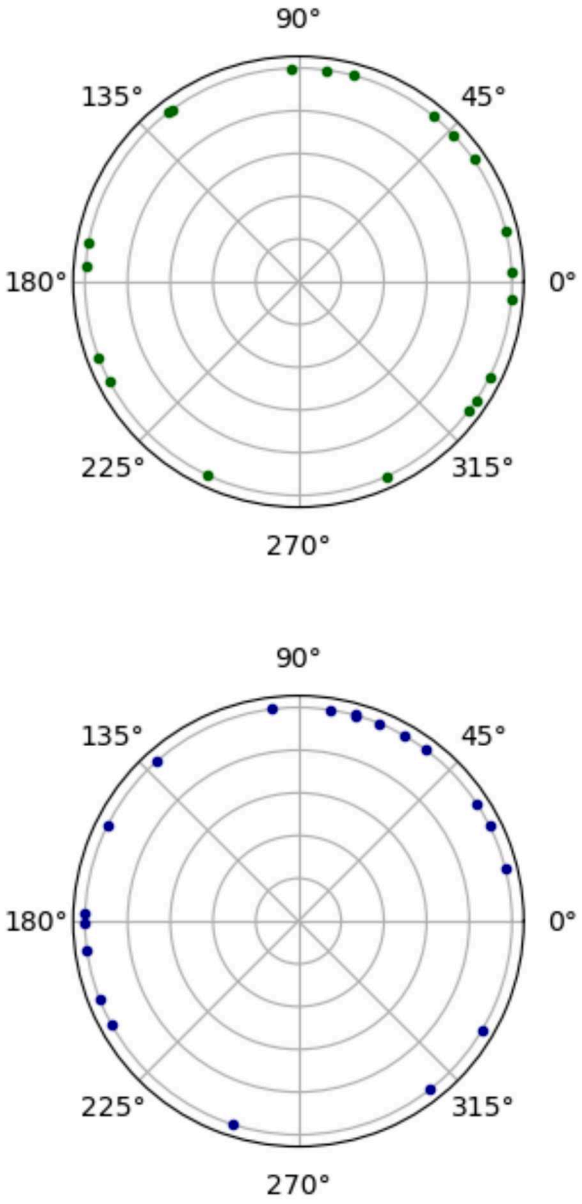

Figure 4.7: Horizontal (upper) and vertical (lower) phase advance distribution of 20 used orbit correctors for the baseline lattice

calculations. These initial iterations ensured convergence of beta beating and horizontal dispersion values. Figure 4.8 showed the reduction of the horizontal and vertical beta beating over each LOCO iteration until convergence. As seen in Fig.4.8, the first LOCO iteration had the most impact on reducing the beta beating. These results were produced from choosing a relatively large number of singular values when performing the SVD, leading to faster convergence of the fit. Following the beta-beating iterations, one iteration of coupling and dispersion correction was applied, including the on and off (coupling) diagonal matrices, where skew quadrupole strengths were adjusted alongside normal ones. A final iteration of beta-beating correction was then applied to refine the beta-beating values from the previous step. Vertical dispersion remained relatively stable throughout this last iteration. Each LOCO iteration was interleaved with tune fitting. The LOCO iteration steps with the interleaved tune fitting are illustrated in Fig.4.9. A final check on tune and chromaticity preceded emittance and DA calculations.

The implemented Python-based numerical code for LOCO correction, has been tested using FCC-ee $t\bar{t}$ energy mode 182.5 GeV [129]. The code has also been integrated into the Python version of the Simulated Commissioning toolkit for Synchrotrons (PySC) [130–132]. The code will be expanded and applied in the commissioning of PETRA IV at the Deutsches Elektronen Synchrotron (DESY) [133–135]. A validation of the code under strength and calibration errors using PETRA IV lattice can be found in Appendix B.

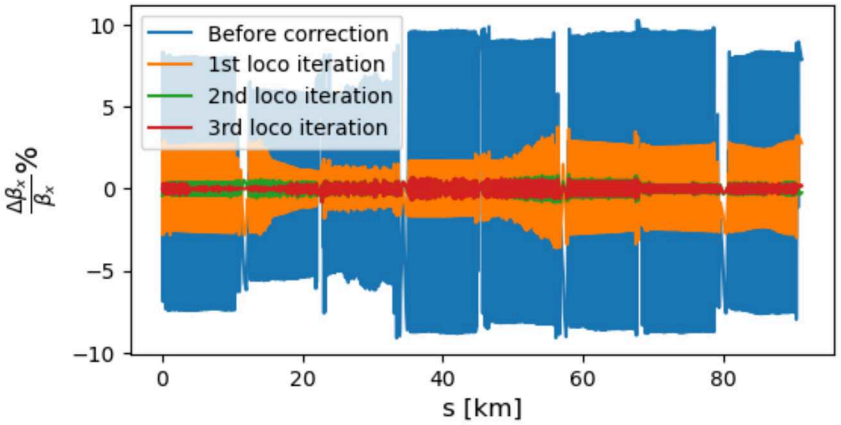

(a) Horizontal beta beating correction

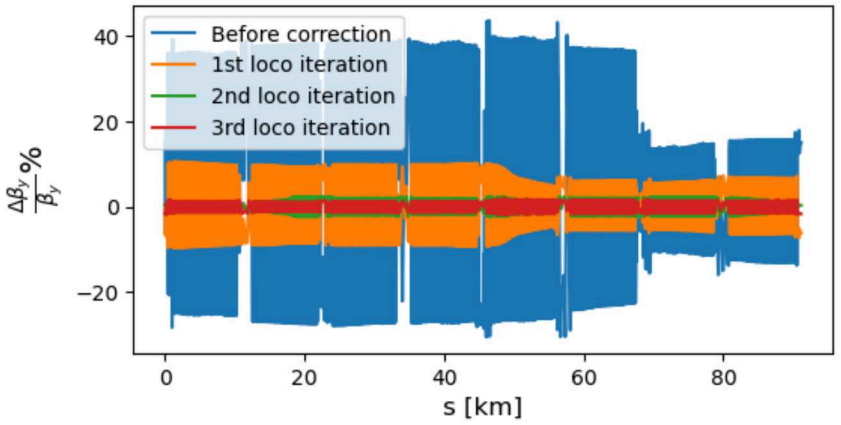

(b) Vertical beta beating correction

Figure 4.8: Improvement of beta beating over three LOCO iterations

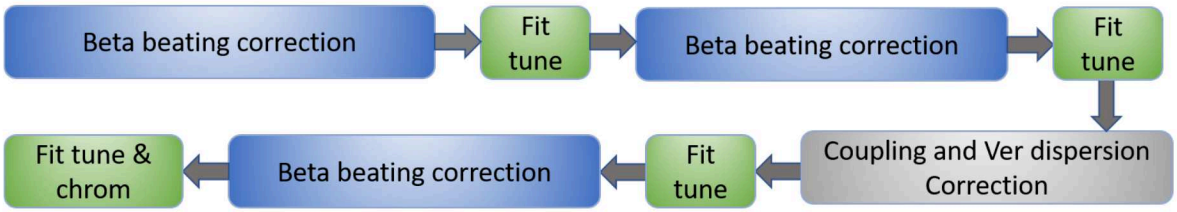

Figure 4.9: Explanation of the initial LOCO iteration scheme

4.2 Optics sensitivity to magnet alignment errors

In this section we present a sensitivity analysis to investigate the impact of magnets misalignment errors on various optics parameters crucial for the machine performance. The parameters evaluated include horizontal and vertical Closed Orbit Distortion (COD), relative dispersion, beta beating, tune, chromaticity, and emittance. Sextupoles were set to 100% of their design value for this sensitivity analysis. Horizontal and vertical random alignment errors distributed via a Gaussian distribution with a cutoff at 2.5 times the standard deviation. The cutoff and alignment error values are consistently applied throughout the simulations tested in this thesis, unless specified otherwise. Errors were systematically introduced first to the arc quadrupoles, sextupoles, and dipoles, and then to the IR magnets. The range of standard deviations used (in micrometers) is:

$$[0.0, 0.2, 0.4, 0.6, 0.8, 1, 1.2]$$

These misalignment values are unrealistically small and are just used to compare the sensitivity of the lattice to alignment errors on arc region magnets and on the IR magnets separately, enabling insightful comparisons between these two regions of the proposed FCC-ee. Additionally, the study compared the optics performance between the proposed baseline and the LCCO lattices, providing further insights into optimal design considerations. Fifty simulations were conducted, each employing different random seed, and the assigned alignment errors followed the same standard deviation range. The study generated plots illustrating the standard deviation of alignment errors against each evaluated parameter.

4.2.1 Arc region

Figures 4.10–4.14 show how various optics parameters change with the increase in the standard deviation of random errors applied to the arc magnets for the baseline and LCCO lattices. Large outliers were removed from the plots when needed. Following the mean values line in the plots, the COD difference between the baseline lattice and LCCO is not clear, as seen in Fig. 4.10. However, Fig. 4.2.1 illustrates that the horizontal and

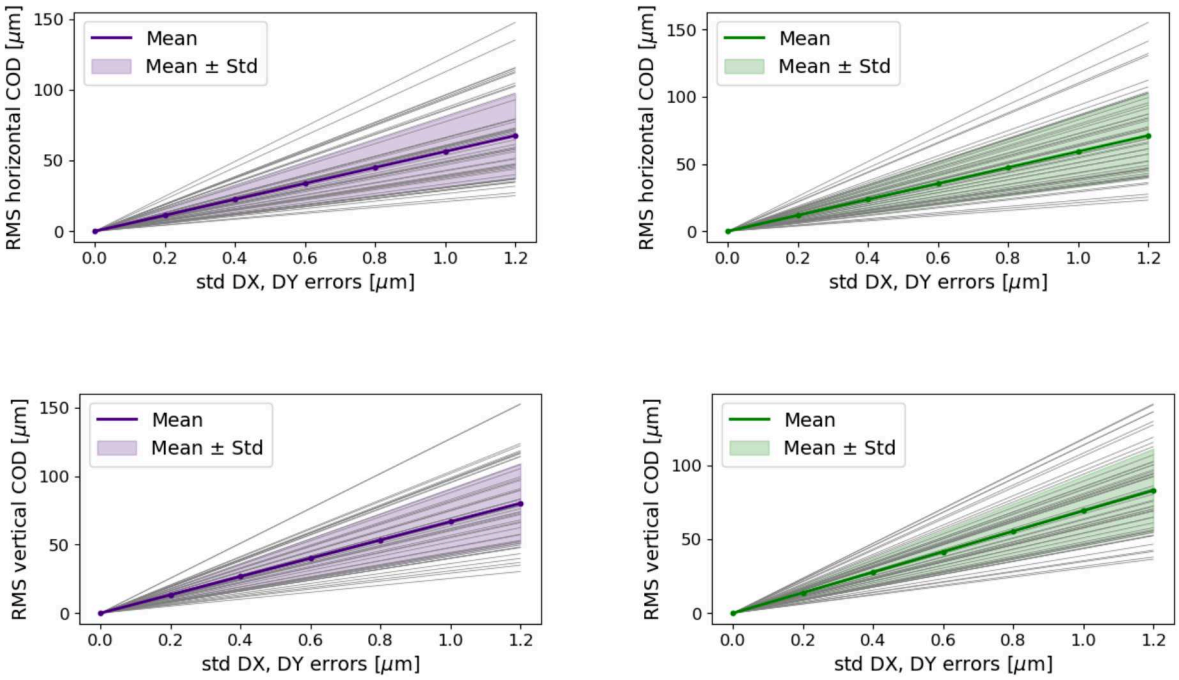

Figure 4.10: Horizontal and vertical closed orbit distortion vs. error standard deviation for the baseline (left) lattice and LCCO lattice (right) (errors in arc magnets)

vertical dispersion distortions are larger for the baseline lattice compared to LCCO. The assigned errors in the arc region do not lead to a significant increase in the beta beating for either lattice, as shown in Fig. 4.11. The fractional part of the horizontal tunes, shown in Fig. 4.12, does not exhibit large variations that might lead to resonance issues; however, the LCCO lattice vertical tune variation is larger compared to the baseline. In contrast, the baseline lattice showed a large change in vertical chromaticity compared to the LCCO, as seen in Fig. 4.14. Regarding emittances, the horizontal emittance does not show significant distortion with errors, while the vertical emittance distortion is larger and more pronounced for the LCCO lattice, as shown in Fig. 4.14.

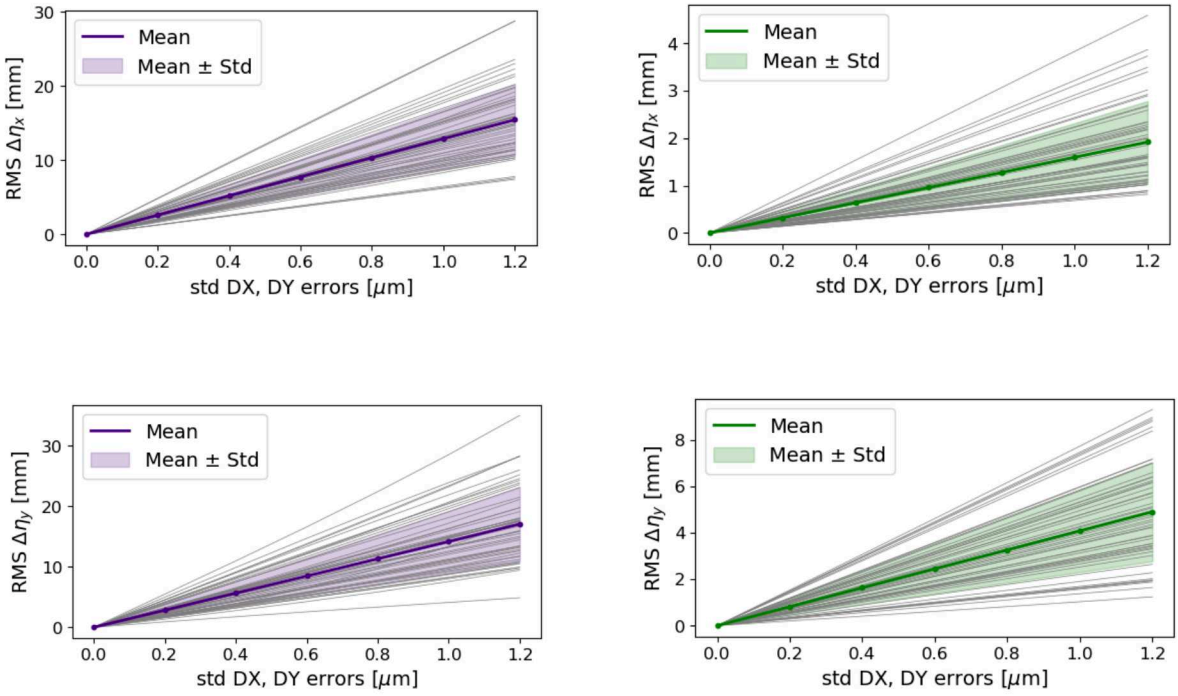

4.2.2 Interaction region

The distortion of the optics parameters is larger when errors are applied to the IR magnets as seen in Figures 4.15–4.21. In this scenario, all parameters exhibit greater distortion for both lattices compared to when errors are only applied to the arc magnets, e.g. when misalignments are applied to the arc region, the baseline design shows a mean rms vertical dispersion of 15 mm, while the LCCO design results in a mean vertical dispersion of 5 mm. In contrast, for misalignments applied only to the IR, the baseline design experiences a larger rms mean vertical dispersion of approximately 500 mm, whereas the LCCO design maintains a mean vertical dispersion of 70 mm.

As mentioned earlier, turning off the radiation and sextupoles at the beginning of the simulation allows for assigning larger error values, avoiding any non-linearity or instability caused by the sextupole fields and radiation before applying corrections. A similar optics sensitivity to error analysis study with larger error values, conducted with sextupoles and

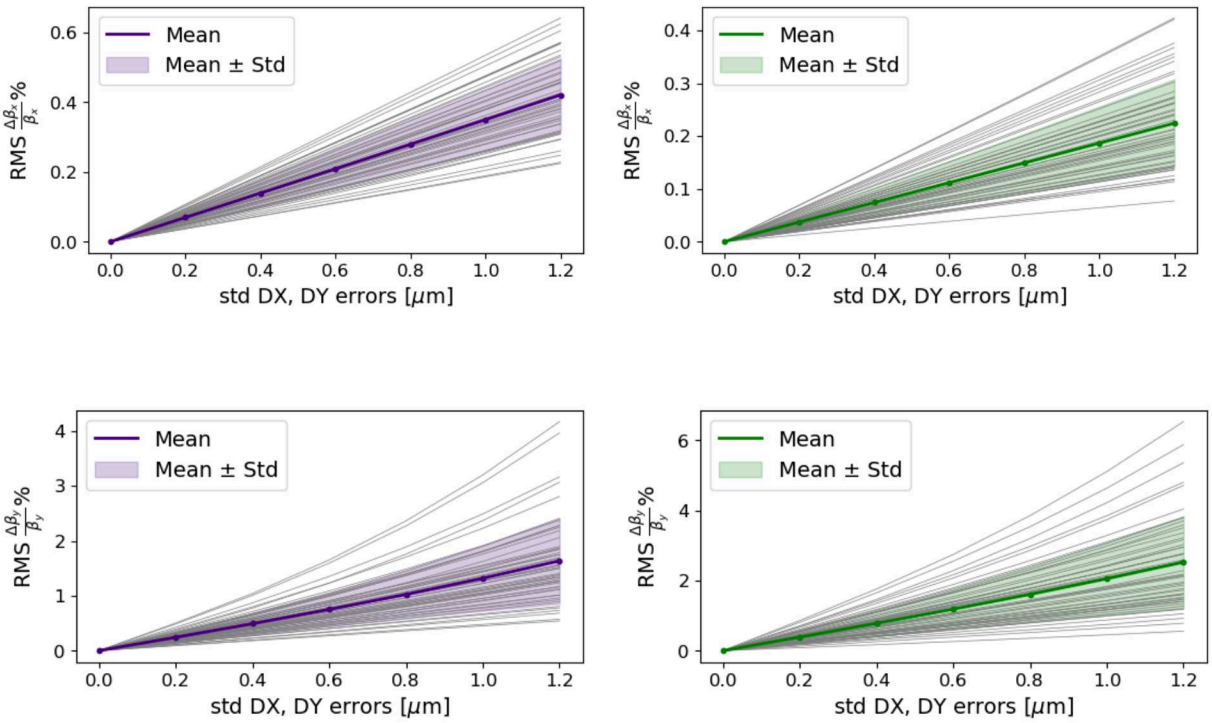

Figure 4.11: Horizontal and vertical percentage beta beating vs. error standard deviation for the baseline (left) lattice and LCCO lattice (right) (errors in arc magnets)

radiation turned off, is available in Appendix A.2. In the mentioned study, the assigned random alignment errors standard deviations are increased by a factor of 10, starting from a standard deviation of 10 μm up to 50 μm. These errors were applied to the arc, the IR, and in combination to both regions.

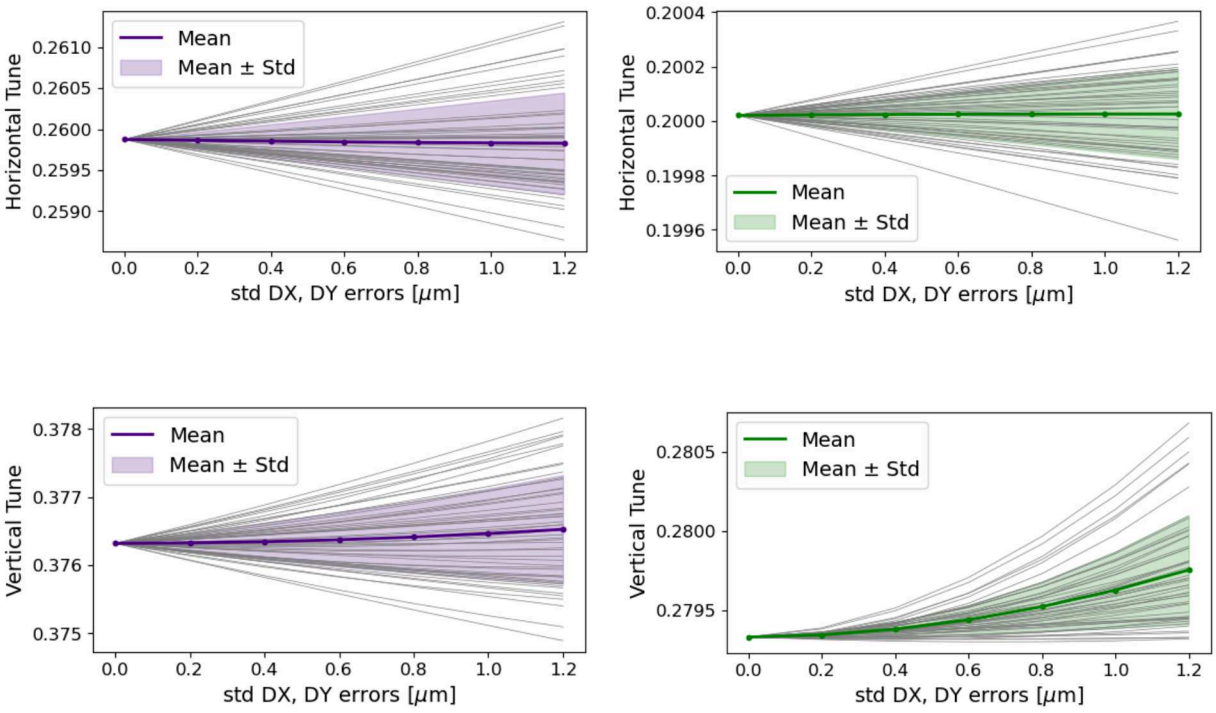

Figure 4.12: Horizontal and vertical tune vs. error standard deviation for the baseline (left) lattice and LCCO lattice (right) (errors in arc magnets))

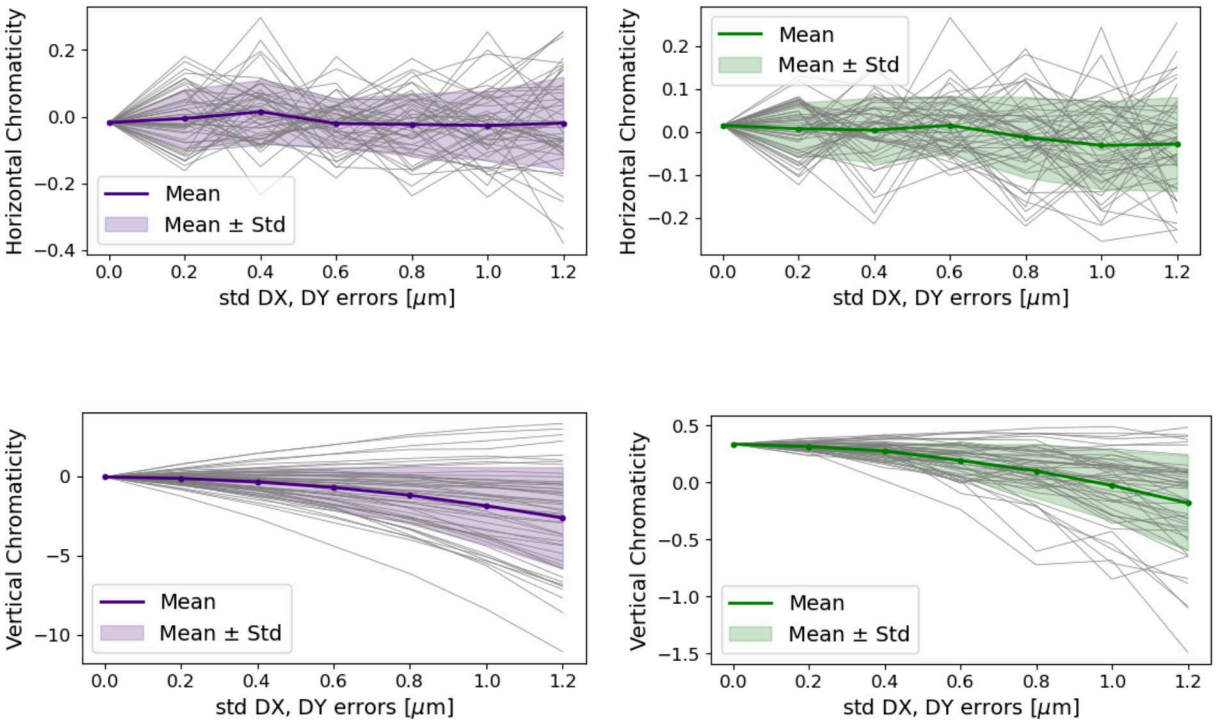

Figure 4.13: Horizontal and vertical chromaticity vs. error standard deviation for the baseline (left) lattice and LCCO lattice (right) (errors in arc magnets)

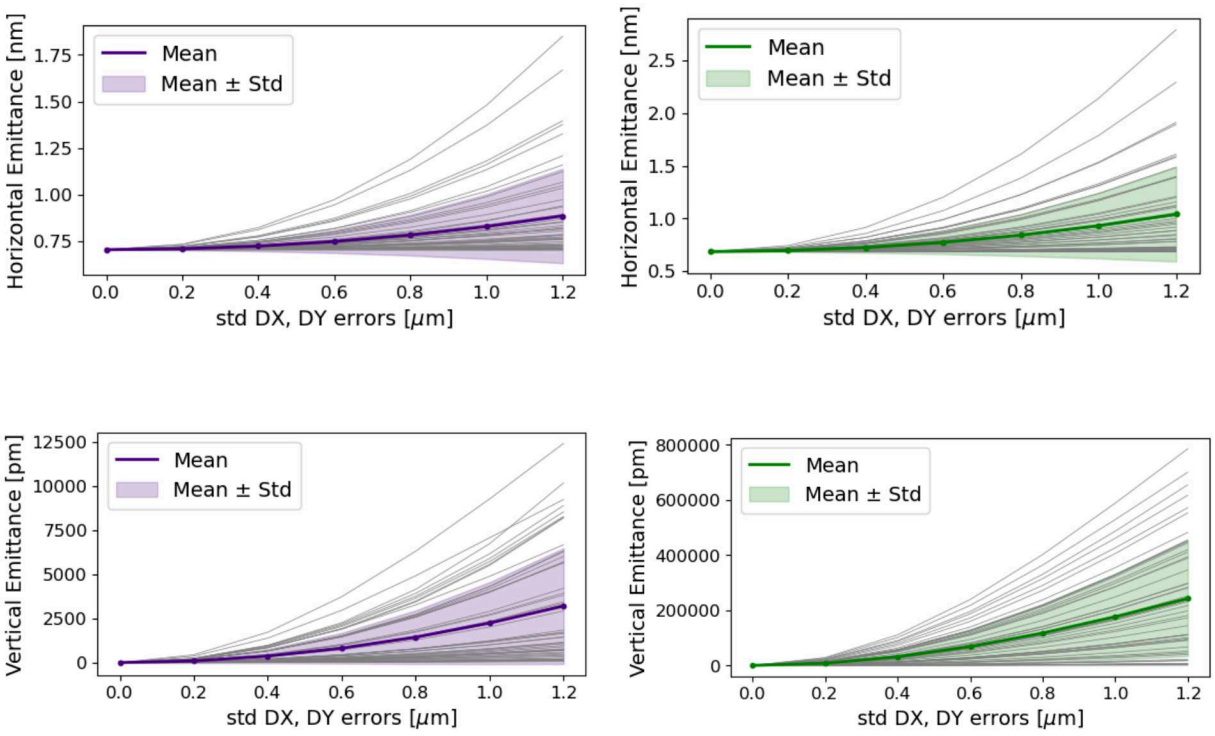

Figure 4.14: Horizontal and vertical emittance vs. error standard deviation for the baseline (left) lattice and LCCO lattice (right) (errors in arc magnets)

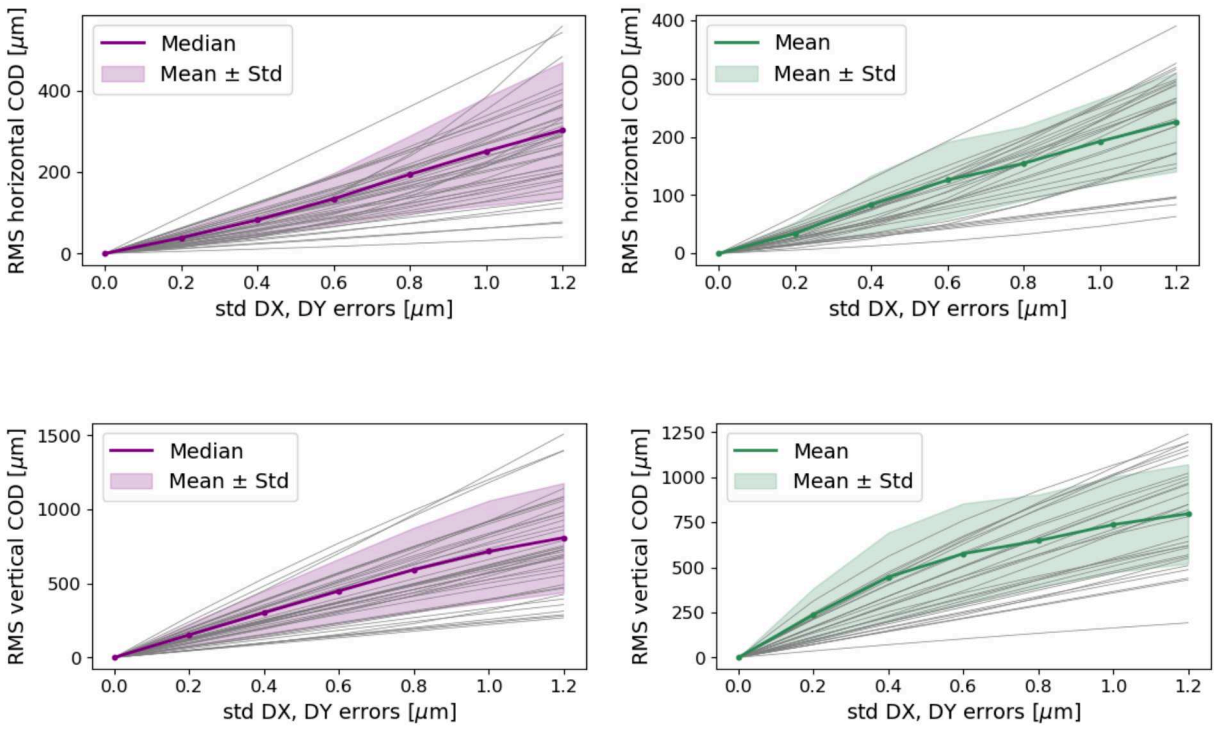

Figure 4.15: Horizontal and vertical closed orbit distortion vs. error standard deviation for the baseline (left) lattice and LCCO lattice (right) (errors in IR magnets)

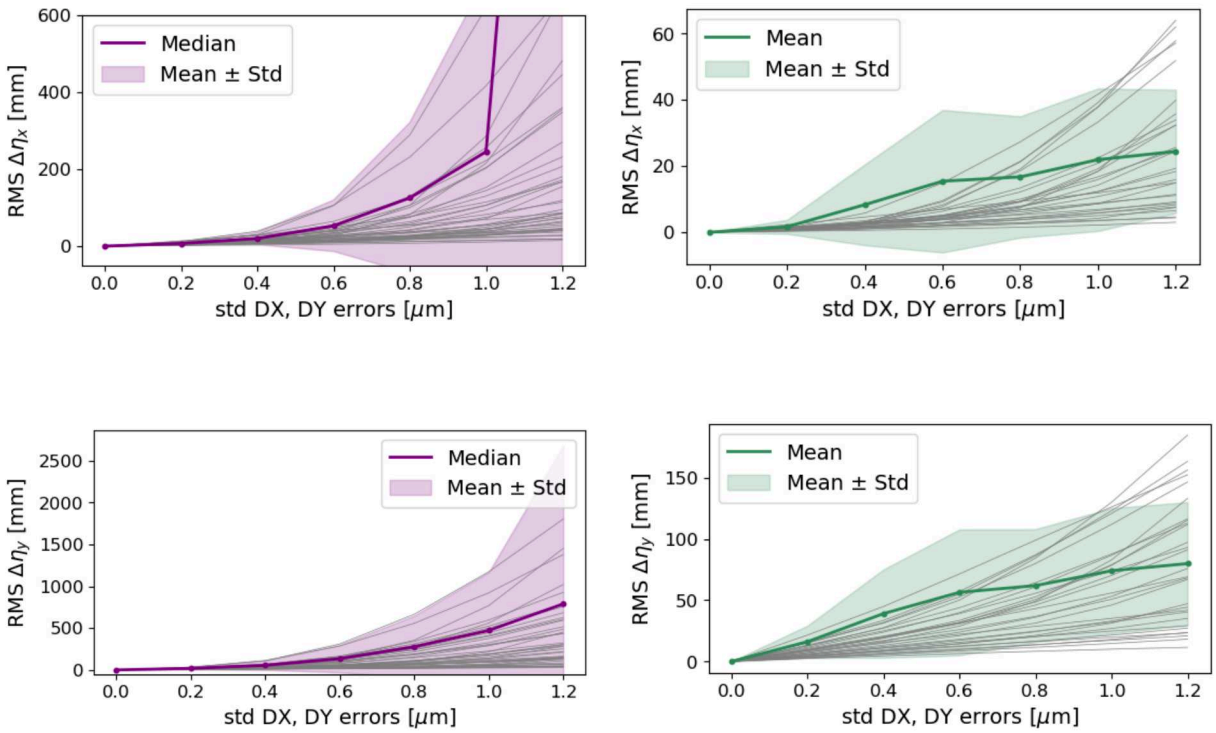

Figure 4.16: Horizontal and vertical relative dispersion vs. error standard deviation for the baseline (left) lattice and LCCO lattice (right) (errors in IR magnets)

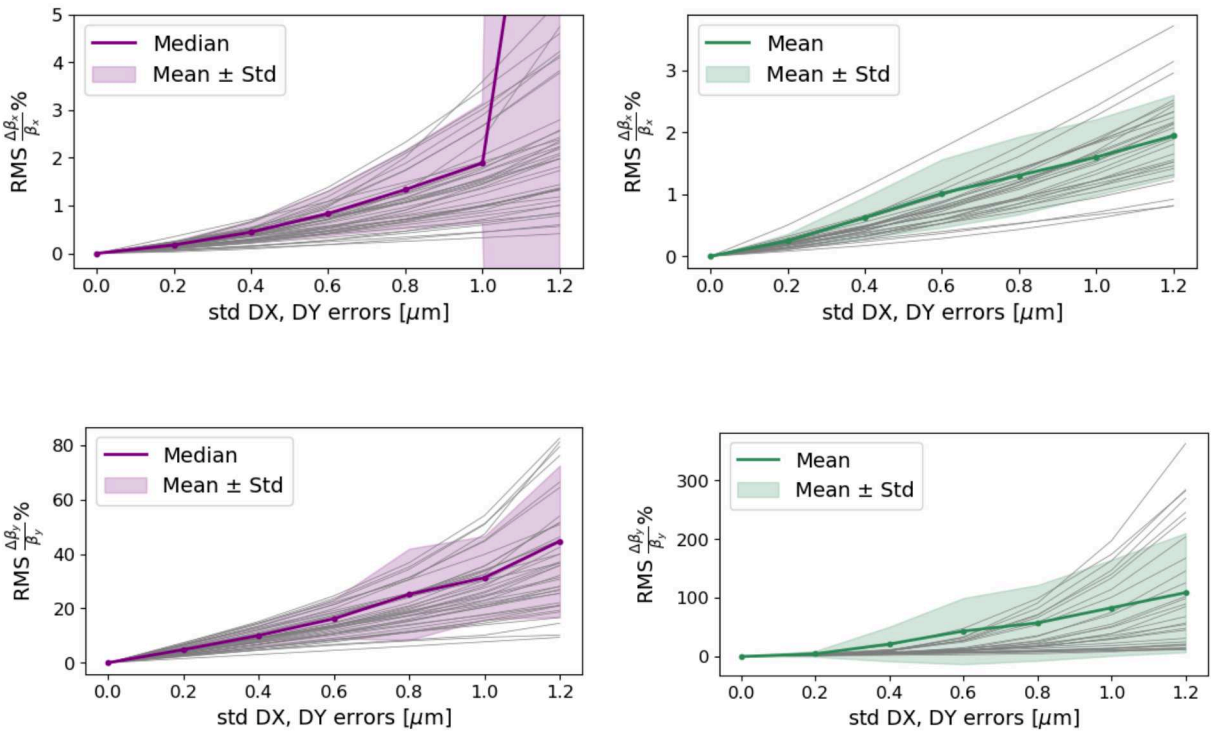

Figure 4.17: Horizontal and vertical percentage beta beating vs. error standard deviation for the baseline (left) lattice and LCCO lattice (right) (errors in IR magnets)

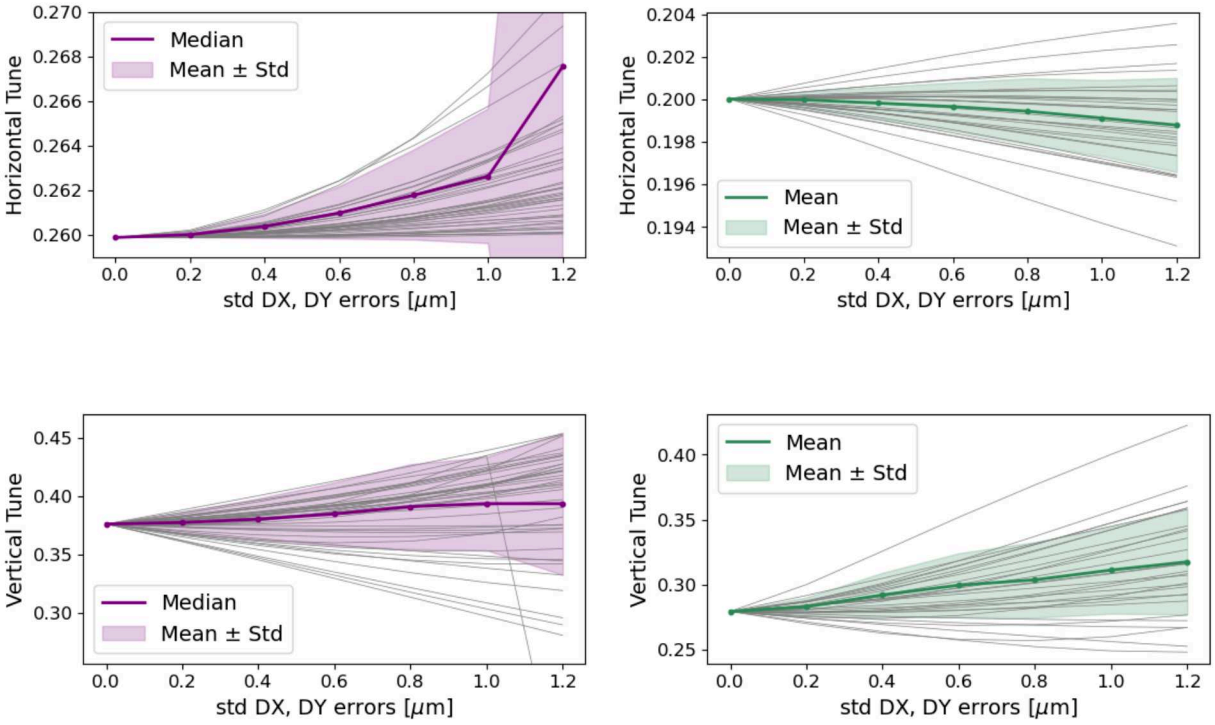

Figure 4.18: Horizontal and vertical tune vs. error standard deviation for the baseline (left) lattice and LCCO lattice (right) (errors in IR magnets)

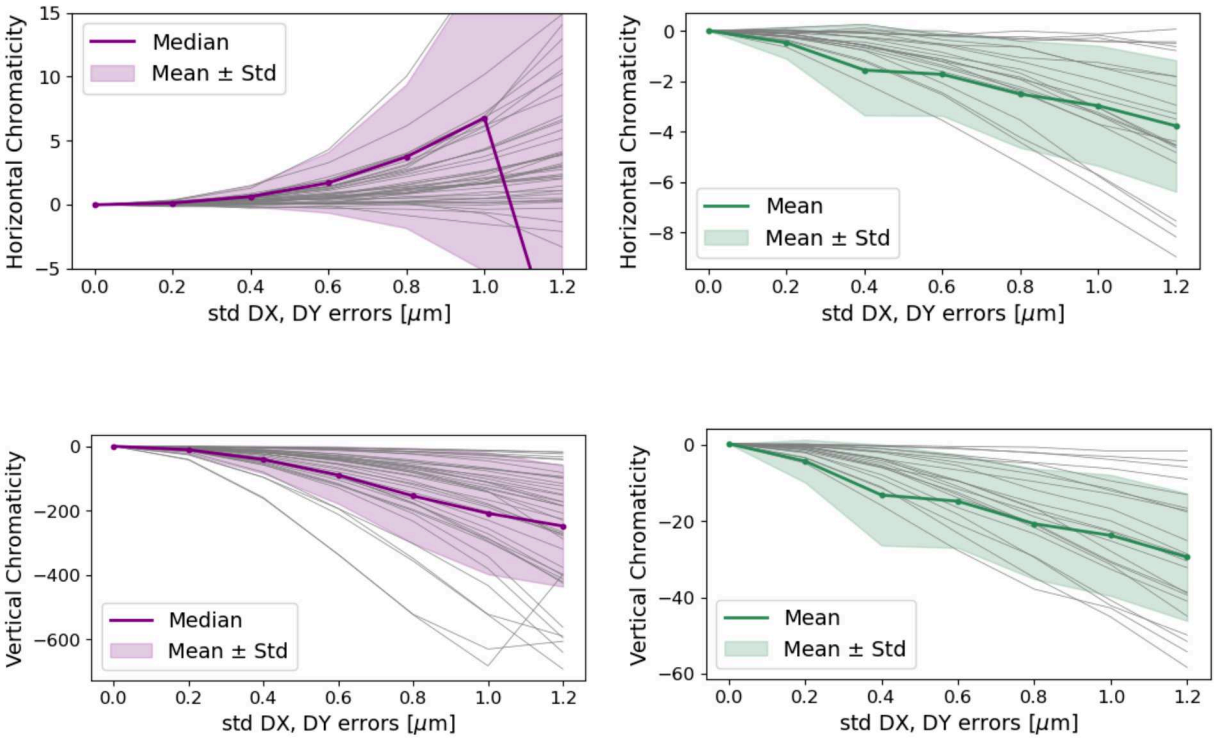

Figure 4.19: Horizontal and vertical chromaticity vs. error standard deviation for the baseline (left) lattice and LCCO lattice (right) (errors in IR magnets)

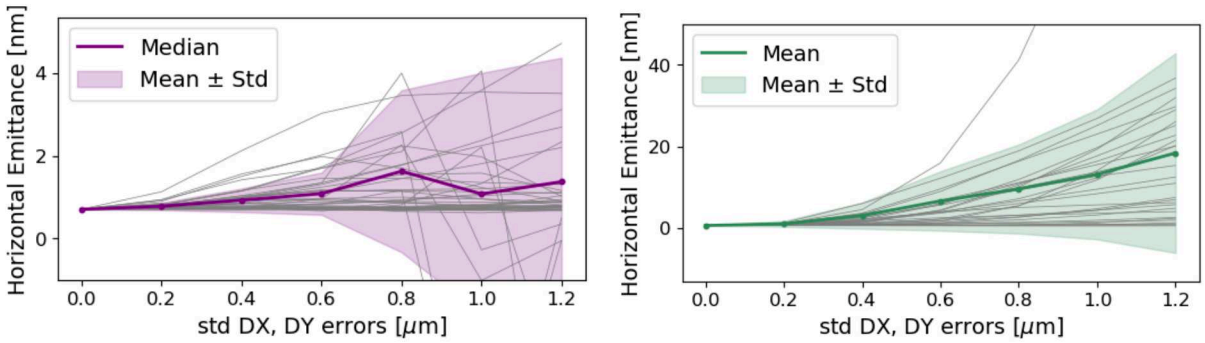

Figure 4.20: Horizontal emittance for baseline lattice

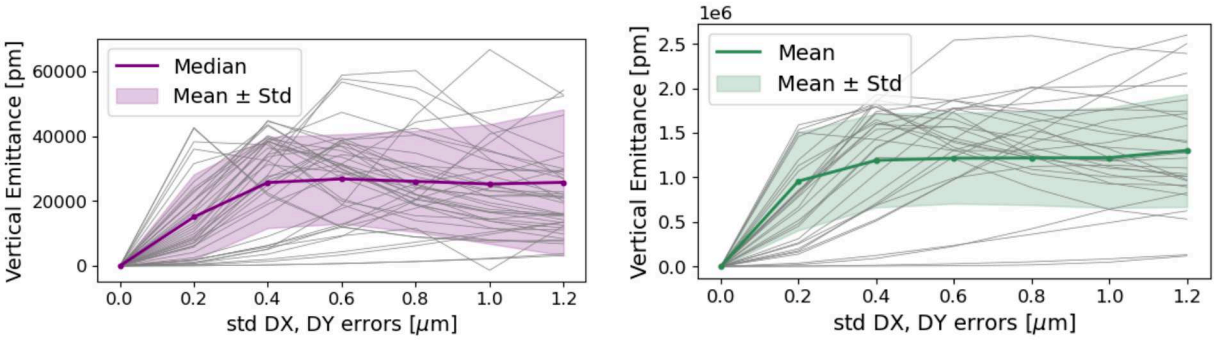

Figure 4.21: Horizontal and vertical emittance vs. error standard deviation for the baseline (left) lattice and LCCO lattice (right) (errors in IR magnets)

4.3 Preliminary results of tuning procedure

The initially implemented correction scheme was tested with random alignment errors with standard deviation of 10 μm on arc magnets for the baseline and LCCO lattices. The BPMs alignments are considered later in Sec. 4.9. When assigning errors, before performing any corrections, PyAT failed to calculate emittance values, indicating unstable optics. Consequently, the other optics parameters, which were calculated using only 4D phase space coordinates (i.e. without the effects of radiation) are unreliable; however, they indicate that these parameters will be large. In tables 4.2 and 4.3, the emittance with errors, before performing any corrections, is marked with "-" to indicate that the emittance could not be calculated. Similarly, in the following tables throughout this chapter "-" in the emittance column indicates that the emittance could not be calculated.

Tables 4.2 and 4.3 show optics parameters at the intermediary correction steps of the procedure outlined in Fig. 4.2. Tables 4.2 and 4.3 demonstrates reduction in orbit rms values following the SVD orbit and tune correction. Turning on the sextupoles after this step increased the beta beating and dispersion via the feed down effect from sextupoles misalignments, which required optics correction using LOCO. The first two LOCO iterations corrected the horizontal and vertical beta beating, followed by a LOCO coupling correction iteration that reduced the horizontal and vertical dispersion as seen in the table. The correction procedure resulted in vertical emittance mean values of 0.12 pm and 0.057 pm for the baseline and LCCO lattices, respectively, both of which are below the target vertical emittance value of 0.7 pm.

We further increased the assigned random errors standard deviation to 20 μm. Tables 4.4 and 4.5 show achieved mean vertical emittance values of 1.34 pm and 5.14 pm for the baseline and LCCO lattices respectively, after correction. These values exceed the target, even with small rms misalignments of 20 μm, indicating that the initial correction scheme needs further optimization in order tolerate realistic error values.

Figures 4.22 and 4.23 show the distribution of horizontal and vertical emittance for 50 seeds after the correction of 10 μm and 20 μm standard deviations of random alignment errors in the baseline and LCCO lattices. Figure 4.23 shows two large outliers that influence the vertical emittance mean value for the LCCO lattice.

At this stage, it is premature to include the IR errors due to the high sensitivity of the IR region to errors (as seen in Subsection 4.2.2), while the correction scheme is still under development. However, the correction procedure has also been tested with random alignment errors of 10 μm standard deviation in both arc and IR magnets for the two lattices. Tables 4.6 and 4.7 show that while the optics were corrected through the chain, PyAT failed to provide emittance values for the baseline lattice after correction, the other optics parameters aren't reliable, but give an indication of the optics parameters values after correction. For the LCCO lattice, the resulting vertical emittance was 4.89 pm.

Table 4.2: Optics values of the baseline after each correction step with horizontal and vertical random displacement errors having standard deviation of 10 μm on arc magnets for 50 seeds

		rms orbit x (μm)	rms orbit y (μm)	$\Delta\beta_x/\beta_x$ (%)	$\Delta\beta_y/\beta_y$ (%)	$\Delta\eta_x$ (mm)	$\Delta\eta_y$ (mm)	ε_{h} (nm)	ε_{v} (pm)
With errors	mean	661.1230	766.0700	1.20e-07	1.80e-04	1294.3200	8109.6700	-	-
	std	298.5500	297.0230	7.50e-08	6.152e-06	835.0800	5724.0400	-	-
Orbit cor.	mean	0.8530	0.8250	6.88e-06	1.80e-04	0.0187	0.0242	0.7060	0.0054
	std	0.0490	0.0520	2.10e-10	8.44e-09	0.0079	0.0105	0.0001	0.0069
Sext. on	mean	0.8570	0.8370	0.6340	0.9616	3.9900	4.4190	0.7060	0.1366
	std	0.0480	0.0510	0.1990	0.4800	1.3890	1.6510	0.0002	0.0684
Beta beat cor.	mean	0.8590	0.8460	0.1764	0.2080	3.6710	4.4190	0.7060	0.1690
	std	0.0504	0.0520	0.0746	0.0977	1.2840	1.6560	0.0002	0.0952
Coup. & η_y cor.	mean	0.8600	0.8430	0.1740	0.2137	0.0330	0.1522	0.7060	0.1258
	std	0.0490	0.0520	0.0728	0.0996	0.0064	0.0099	0.0002	0.0869
Final cor. result	mean	0.8600	0.8430	0.1474	0.1890	0.4640	0.1520	0.7060	0.1265
	std	0.0490	0.0520	0.0750	0.0940	0.1970	0.0095	0.0002	0.0870

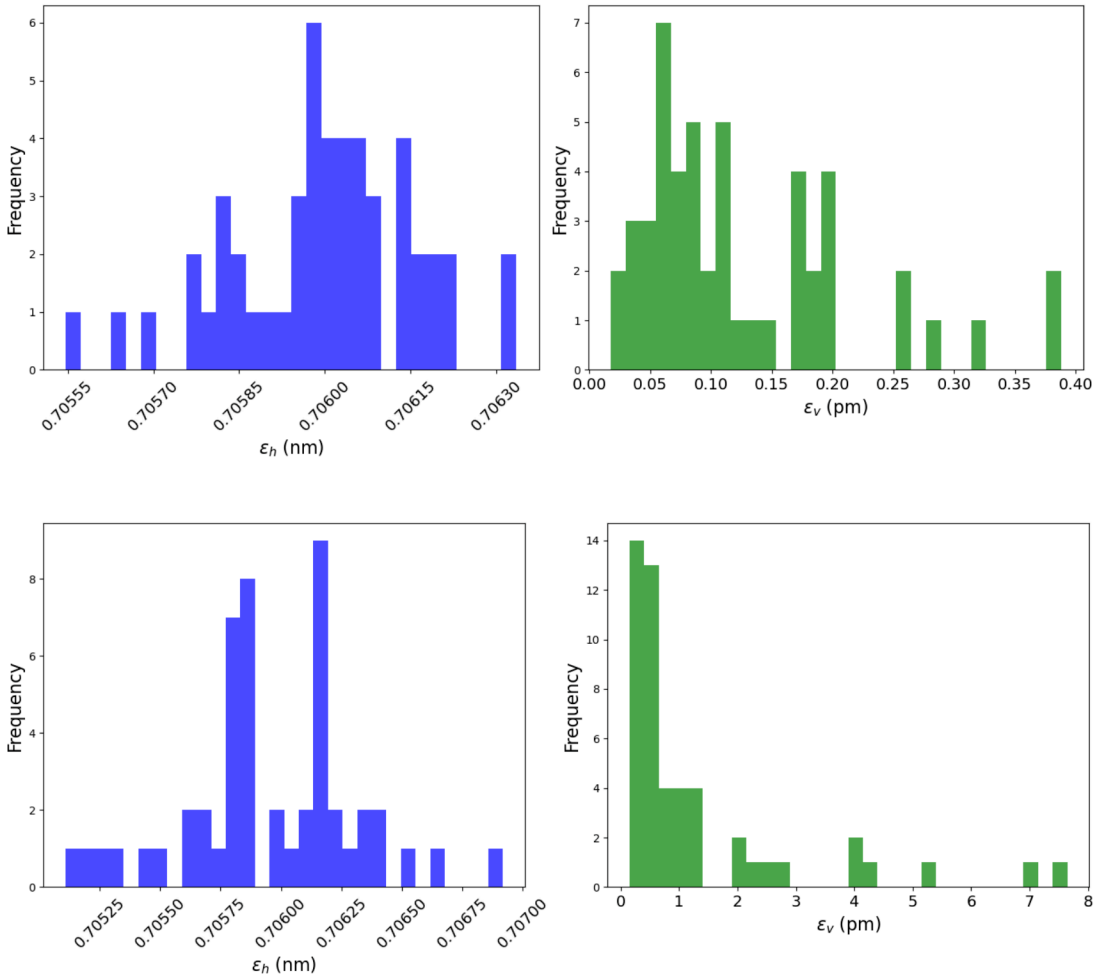

Figure 4.22: Horizontal (left) and vertical (right) emittance distributions for 50 seeds, following the correction chain outlined in Fig. 4.2, are shown for random alignment errors with standard deviations of 10 μm (upper plots) and 20 μm (lower plots) in the arc magnets of the baseline lattice

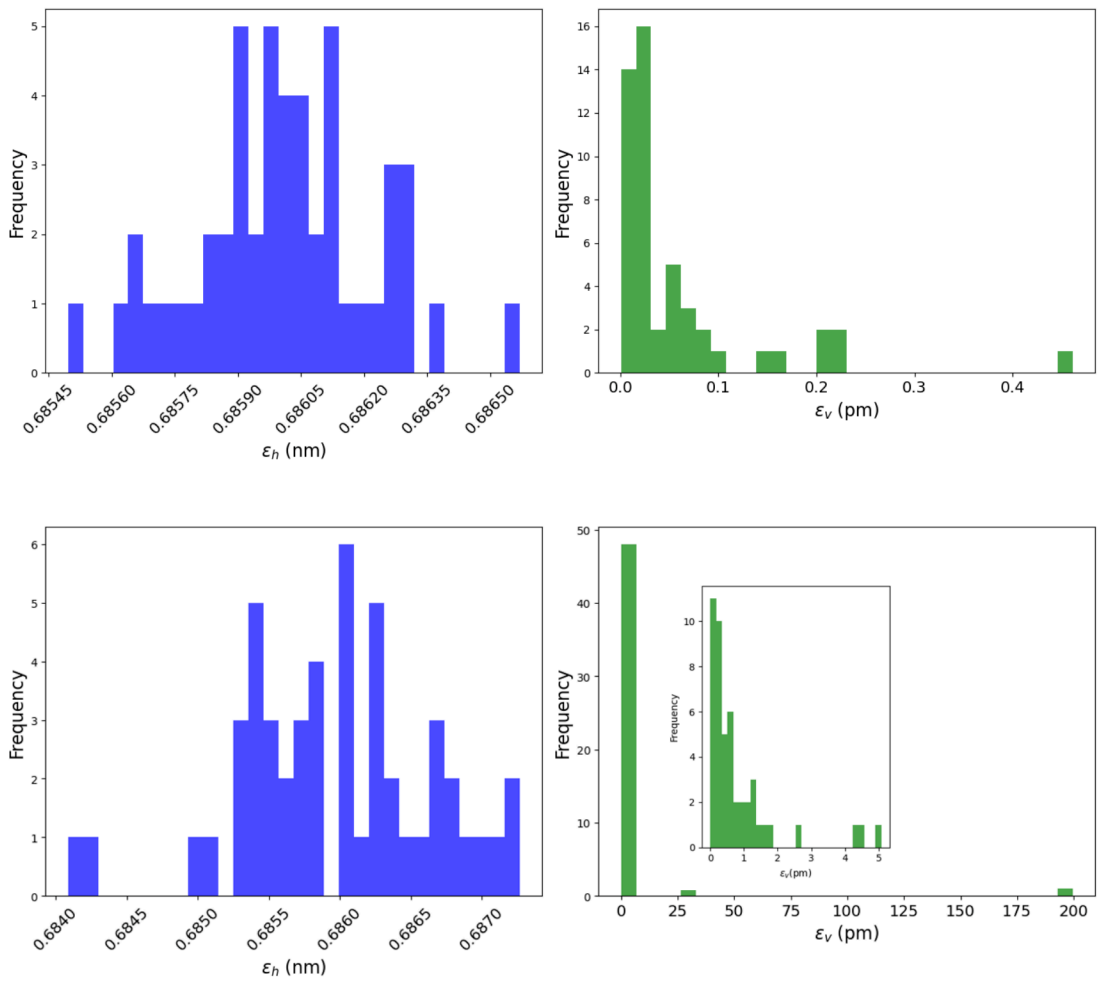

Figure 4.23: Horizontal (left) and vertical (right) emittance distributions for 50 seeds, following the correction chain outlined in Fig. 4.2 are shown for random alignment errors with standard deviations of 10 μm (upper plots) and 20 μm (lower plots) in the arc magnets of the LCCO lattice. The inset in the bottom right plot shows the distribution after removing two large outliers.

Table 4.3: Optics values of the LCCO after each correction step with horizontal and vertical random displacement errors having standard deviation of 10 μm on arc magnets for 50 seeds

		rms orbit x (μm)	rms orbit y (μm)	$\Delta\beta_x/\beta_x$ (%)	$\Delta\beta_y/\beta_y$ (%)	$\Delta\eta_x$ (mm)	$\Delta\eta_y$ (mm)	ε_{h} (nm)	ε_{v} (pm)
With errors	mean	516.6480	696.1600	1.10e-04	4.70e-04	784.9600	10010.6800	-	-
	std	225.7870	302.4920	1.30e-04	1.62e-05	497.5500	7323.8800	-	-
Orbit cor.	mean	0.3320	0.3320	2.58e-08	4.60e-04	0.0130	0.0120	0.6860	0.0001
	std	0.0255	0.0243	1.11e-10	7.97e-10	0.0046	0.0058	0.0002	0.0001
Sext. on	mean	0.3320	0.3330	0.1050	0.1556	0.8045	1.0560	0.6860	0.2370
	std	0.0255	0.0244	0.0350	0.0470	0.3340	0.4720	0.0002	0.3420
Beta beat cor.	mean	0.3320	0.3340	0.0230	0.0278	0.1710	1.0560	0.6860	0.2560
	std	0.0250	0.0240	0.0067	0.0110	0.0880	0.4710	0.0002	0.3630
Coup. & η_y cor.	mean	0.3323	0.3340	0.0037	0.0260	0.0013	0.0098	0.6860	0.0570
	std	0.0250	0.0240	0.0014	0.0083	0.0005	0.0005	0.0002	0.0840
Final cor. result	mean	0.3320	0.3340	0.0132	0.0223	0.1020	0.0098	0.6860	0.0570
	std	0.3320	0.3340	0.0130	0.0230	0.1020	0.0090	0.6860	0.0574

Table 4.4: Optics values of the baseline after each correction step with horizontal and vertical random displacement errors having standard deviation of 20 μm on arc magnets for 50 seeds

		rms orbit x (μm)	rms orbit y (μm)	$\Delta\beta_x/\beta_x$ (%)	$\Delta\beta_y/\beta_y$ (%)	$\Delta\eta_x$ (mm)	$\Delta\eta_y$ (mm)	ε_{h} (nm)	ε_{v} (pm)
With errors	mean	1119.58	1493.39	1.92e-7	0.00019	2002.22	16028.51	-	-
	std	515.60	533.66	1.39e-7	1.37e-5	1572.75	10891.69	-	-
Orbit cor.	mean	1.71	1.66	6.83e-9	0.00018	0.036	0.044	0.71	0.02
	std	0.09	0.10	4.04e-10	1.52e-8	0.013	0.017	0.000	0.02
Sext. on	mean	1.74	1.74	1.18	2.10	9.21	9.79	0.71	0.89
	std	0.10	0.11	0.38	0.77	3.56	3.54	0.0004	0.65
Beta beat cor.	mean	1.76	1.83	0.33	0.41	8.43	9.79	0.71	1.54
	std	0.11	0.20	0.14	0.20	3.29	3.52	0.0004	1.77
Coup. & η_y cor.	mean	1.78	1.81	0.36	0.44	0.10	0.33	0.71	1.36
	std	0.11	0.20	0.14	0.22	0.03	0.04	0.0004	1.75
Final cor. result	mean	1.78	1.81	0.29	0.37	1.09	0.35	0.71	1.34
	std	0.11	0.20	0.14	0.18	0.44	0.12	0.0004	1.70

Table 4.5: Optics values of the LCCO after each correction step with horizontal and vertical random displacement errors having standard deviation of 20 μm on arc magnets for 50 seeds

		rms orbit x (μm)	rms orbit y (μm)	$\Delta\beta_x/\beta_x$ (%)	$\Delta\beta_y/\beta_y$ (%)	$\Delta\eta_x$ (mm)	$\Delta\eta_y$ (mm)	ε_{h} (nm)	ε_{v} (pm)
With errors	mean	1225.0700	1474.8500	8.00e-04	6.00e-04	1851.6450	20718.8300	-	-
	std	617.8000	710.8400	1.00e-03	3.60e-04	1306.1060	16730.2800	-	-
Orbit cor.	mean	0.6640	0.6470	2.58e-08	4.60e-04	0.0270	0.0680	0.6860	0.0016
	std	0.0436	0.0514	2.55e-10	1.46e-09	0.0130	0.0760	0.0006	0.0035
Sext on	mean	0.6660	0.6573	0.2170	0.2840	1.7360	2.1220	0.6860	0.9790
	std	0.0430	0.0520	0.0630	0.0880	0.7159	0.7670	0.0005	1.3360
Beta beat cor.	mean	0.6710	0.6670	0.0530	0.0630	0.3850	2.2160	0.6860	1.4936
	std	0.0430	0.0570	0.0330	0.0520	0.1620	0.9820	0.0006	1.9690
Coup & η_y cor.	mean	0.6740	0.6745	0.0147	0.1270	0.0340	0.4910	0.6860	1.3120
	std	0.0480	0.0910	0.0380	0.3810	0.1803	2.6800	0.0006	3.3460
Final cor. result	mean	0.6710	0.6890	0.0600	0.0787	0.3550	0.9360	0.6860	5.4153
	std	0.0430	0.1680	0.1940	0.1880	0.5490	4.7290	0.0006	28.3440

Table 4.6: Optics values of the baseline after correction steps with horizontal and vertical random displacement errors having standard deviation of 10 μm on arc and IR magnets for 50 seeds

		rms orbit x (μm)	rms orbit y (μm)	$\Delta\beta_x/\beta_x$ (%)	$\Delta\beta_y/\beta_y$ (%)	$\Delta\eta_x$ (mm)	$\Delta\eta_y$ (mm)
With errors	mean	2188.7400	10110.0690	4.112e-07	2.380e-04	4992.8160	140701.7700
	std	1367.9780	6899.8970	3.712e-07	1.080e-04	4114.4580	116837.4220
Final cor. result	mean	1.1945	1.6650	0.4074	1.8844	0.9420	0.5550
	std	0.0636	0.2240	0.6370	3.9770	0.6960	0.5390

Table 4.7: Optics values of the LCCO after correction steps with horizontal and vertical random displacement errors having standard deviation of 10 μm on arc and IR magnets for 50 seeds

		rms orbit x (μm)	rms orbit y (μm)	$\Delta\beta_x/\beta_x$ (%)	$\Delta\beta_y/\beta_y$ (%)	$\Delta\eta_x$ (mm)	$\Delta\eta_y$ (mm)	ε_{h} (nm)	ε_{v} (pm)
With errors	mean	1244.9630	10843.2070	0.020128	0.014090	2137.1260	192494.1000	-	-
	std	613.8740	6803.6600	0.020300	0.015000	1399.5200	146679.6560	-	-
Final cor. result	mean	1.1584	1.0890	0.0436	0.1105	0.7500	0.0880	0.6850	4.8600
	std	0.4927	0.3120	0.0081	0.0380	0.3920	0.0587	0.0001	3.4110

4.4 Optimizing the correction procedure

In this section, we present various attempts to optimize the correction procedure to achieve the design value of 0.7 pm for vertical emittance under larger alignment tolerances. These optimizations include adjusting the number of singular values used in the SVD orbit correction and ramping the sextupoles in steps. We will also discuss the necessity of repeating some correction steps throughout the entire chain. Additionally, we will explore different optics correction algorithms.

Number of singular values

The impact of increasing the number of singular values used for SVD orbit correction on the rms orbit and dispersion distortion values for the baseline and the LCCO lattice, with 10 μm standard deviation of random alignment errors on both arc and IR regions are shown in Tables 4.8 and 4.9. As the number of chosen singular values increases, there is an improvement in both orbit and dispersion correction. The reduction in rms orbit and dispersion, indicating convergence of the correction, is observed with 1500 singular values for the baseline lattice and 2500 for the LCCO lattice.

Figure 4.24 provides a logarithmic plots of the singular values for the horizontal ORM of the baseline and the LCCO lattice indicating the chosen cut off values.

Table 4.8: Impact of increasing the number of singular values on orbit and dispersion correction for the baseline lattice

Orbit correction	**rms orbit x** (μm)	**rms orbit y** (μm)	$\Delta\eta_x$ (mm)	$\Delta\eta_y$ (mm)
With err	1620.69	9123.88	1452.14	66566.81
Orb cor with 500 svd	14.06	13.62	1.08	7.88
Orb cor with 1000 svd	2.10	2.80	0.56	4.62
Orb cor with 1500 svd	1.69	2.75	0.44	4.61

Sextupoles ramping in steps

Ramping up the strength of the sextupoles in steps has been tested and shows improvement in reducing the distortion of optics parameters. This approach mitigates the

Table 4.9: Impact of increasing the number of singular values on orbit and dispersion correction for the LCCO lattice

Orbit correction	**rms orbit x** (μm)	**rms orbit y** (μm)	$\Delta\eta_x$ (mm)	$\Delta\eta_y$ (mm)
With error	460.89	20334.90	551.49	390637.06
Orb cor with 500 svd	14.29	12.02	1.67	48.96
Orb cor with 1000 svd	4.29	4.27	1.18	18.02
Orb cor with 1500 svd	3.41	2.01	1.15	9.61
Orb cor with 2500 svd	3.09	1.52	1.13	9.11

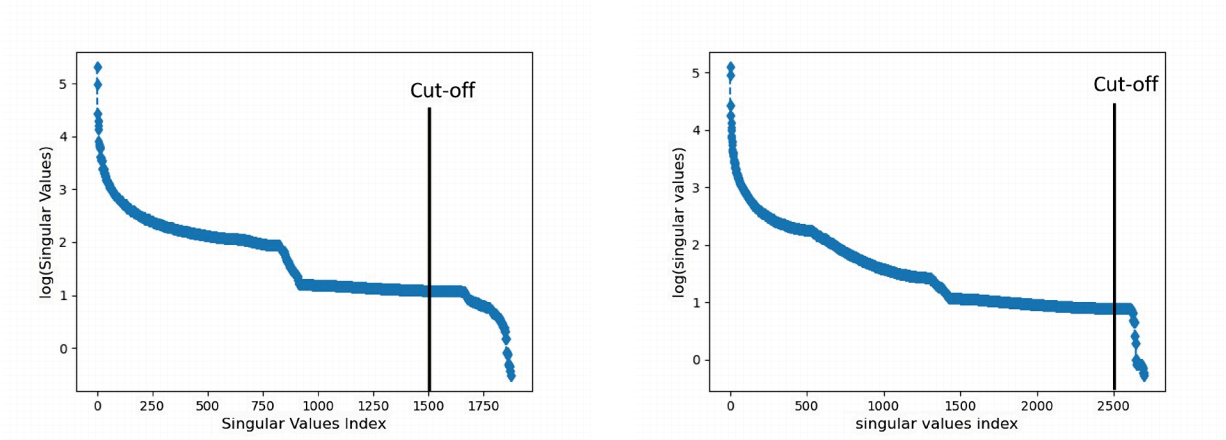

(a) Baseline lattice

(b) LCCO lattice

Figure 4.24: Logarithmic plot of the singular values for the horizontal ORM

strong impact of the sextupoles' nonlinear fields on the optics values. Figures 4.25 and 4.26 present the baseline lattice optics parameter values, including horizontal and vertical tune shifts, at each step of sextupole ramping with no other corrections applied. The plots were generated with random alignment errors in all arc sextupoles, having a standard deviation of 100 μm. As seen from Figures 4.25 and 4.26 the distortion of the optics parameters increases with the strength of the sextupoles, which can lead to the beam encountering resonances or unstable beam dynamics. To manage these variations, we incorporated orbit and tune fitting into the correction process as part of the ramping procedure. When the sex-

tupoles are completely turned on the achieved horizontal and vertical chromaticity values were 1.388 and 0.141 respectively, however, it deviates from the nominal values -0.017 and -0.061, therefore, chromaticity correction is performed at the end of the ramping process. Figure 4.27 shows the sextupoles ramping approach with these variations included.

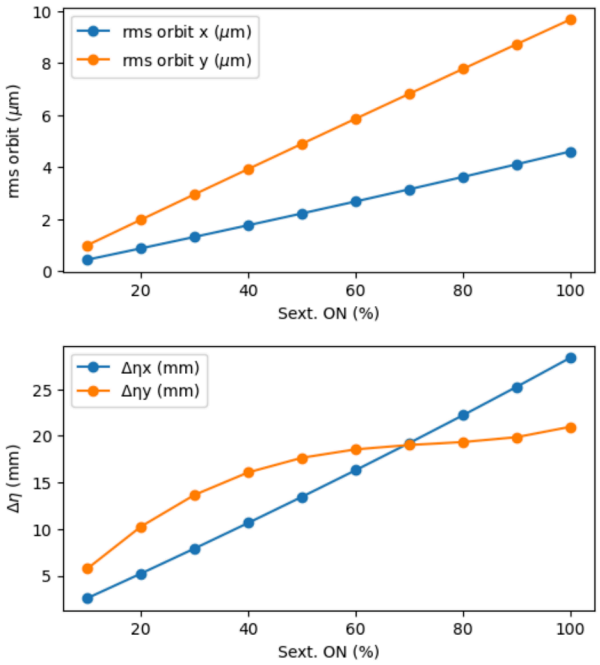

Figure 4.25: RMS distortions for horizontal and vertical orbits and dispersion with increasing sextupole strength.

Before performing the sextupole ramping, the random alignment error tolerance for the baseline lattice was a standard deviation of 10 μm. With sextupole ramping, the alignment tolerance can be increased to a standard deviation of 30 μm.

Additional orbit correction steps along the scheme

With alignment tolerances of 100 μm standard deviation the correction including sextupole ramping shows improvement across optical values, however vertical emittance experienced significant growth, reaching mean values of 537.30 pm for the baseline lattice as shown in Tab. 4.10. The growth in vertical emittance results from the increased orbit

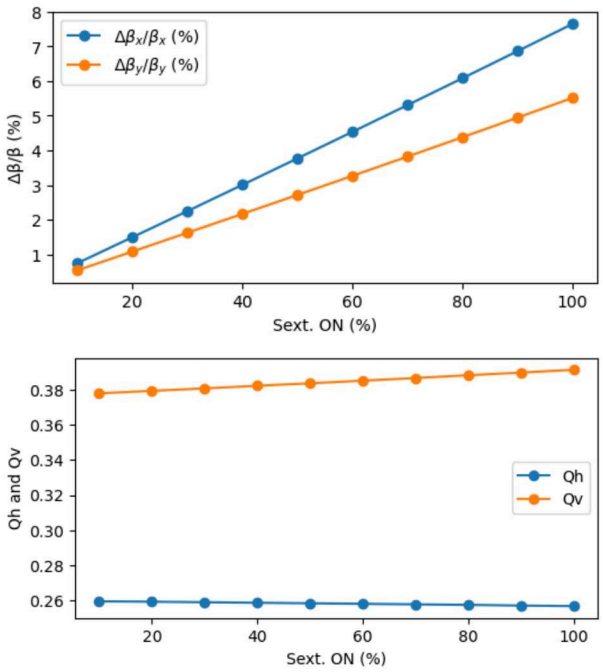

Figure 4.26: Beta beating and tunes for horizontal and vertical planes with increasing sextupole strength. The nominal fractional horizontal and vertical tunes for the baseline lattice are 0.2598 and 0.3763 respectively.

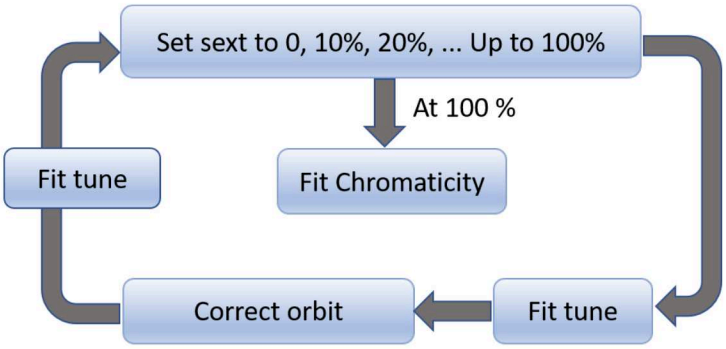

Figure 4.27: Sextupole ramping approach

distortion observed during the correction steps following sextupole ramping. For the baseline lattice the horizontal rms orbit distortion increased from 8.49 μm to 12.81 μm after

ramping, while the vertical rms orbit distortion increased from 8.40 μm to 17.74 μm as illustrated in Tab. 4.10.

After correcting for random alignment errors in the arc magnets of the LCCO lattice, with a standard deviation of 100 μm, the horizontal rms orbit distortion increased from 3.31 μm to 3.87 μm, and the vertical RMS orbit distortion increased from 3.22 μm to 4.36 μm. The achieved mean vertical emittance was 444 μm.

Additional orbit correction steps up to the end of the scheme were necessary and have reduced the achieved vertical emittance for the baseline lattice to from 537.30 pm to 5.99 pm, as shown in Tab. 4.11 where the optics parameters values are shown after final correction of horizontal and vertical random alignment errors having standard deviation of 100 μm in the arc magnets, for the LCCO lattice further orbit correction reduced the vertical emittance values from 325.58 pm to 10.52 pm.

Table 4.10: Correction of horizontal and vertical random alignment errors, with a standard deviation of 100 μm in the arc magnets of the baseline lattice, with sextupole ramping included in the correction procedure for 50 seeds

		rms orbit x (μm)	rms orbit y (μm)	$\Delta\beta_x/\beta_x$ (%)	$\Delta\beta_y/\beta_y$ (%)	$\Delta\eta_x$ (mm)	$\Delta\eta_y$ (mm)	ε_{h} (nm)	ε_{v} (pm)
With errors	mean	5727.41	7304.30	9.35×10^{-7}	2.07×10^{-4}	10560.84	70773.25	-	-
	std	2098.96	2206.81	7.19×10^{-7}	5.77×10^{-5}	6434.41	42308.78	-	-
After sext. ramping	mean	8.49	8.40	5.99	10.40	44.27	43.72	0.71	10.29
	std	0.45	0.45	1.77	4.93	13.26	13.64	0.01	5.62
Beta beat. cor.	mean	10.76	14.90	2.50	3.69	41.52	44.11	0.72	327.05
	std	1.74	3.76	1.22	2.33	16.33	14.67	0.02	402.75
Coupling & η_y cor.	mean	12.62	18.09	4.62	13.38	2.37	4.17	0.73	636.65
	std	2.62	6.12	2.29	10.45	1.07	2.07	0.04	814.78
Final cor. result	mean	12.81	17.74	3.10	6.28	10.19	3.88	0.73	537.30
	std	2.60	5.36	2.95	7.73	5.50	1.77	0.04	664.58

Table 4.11: Constantly correcting the orbit throughout the scheme reduced the achieved vertical emittance. Case 1: Orbit corrected only through the ramping. Case 2: Further orbit corrections. For 50 seeds

		rms orbit x (μm)	rms orbit y (μm)	$\Delta\beta_x/\beta_x$ (%)	$\Delta\beta_y/\beta_y$ (%)	$\Delta\eta_x$ (mm)	$\Delta\eta_y$ (mm)	ε_h (nm)	ε_v (pm)
Case 1	mean	12.81	17.74	3.10	6.28	10.19	3.88	0.73	537.30
	std	2.60	5.36	2.95	7.73	5.50	1.77	0.04	664.58
Case 2	mean	8.56	8.35	1.93	3.23	4.95	2.93	0.70	5.99
	std	0.49	0.44	0.99	3.15	1.93	0.96	0.0049	4.54

4.5 Benchmark of commissioning simulations with errors and corrections: AT vs. MAD-X

Following a previous report on FCC-ee tuning simulations [136] that highlighted some discrepancies between the simulations performed with MAD-X and with AT, we participated in a dedicated comparison study to understand and correct these discrepancies. In this section we used the same errors as outlined in references [137] and [138], and followed the same simulations steps as outlined in the previous subsection.

To include the PyAT data points in the plot shown in Fig. 4.28, the correction steps involved ramping the sextupole strengths in incremental steps, interleaved with orbit and tune corrections, chromaticity corrections were performed at 100% of the sextupole strengths.

Figure 4.28 illustrates the good agreement between the two codes for misalignments up to 30 µm, up to the orbit correction step. Therefore, it is tentatively concluded that the discrepancy from the two studies originates from the different optics correction strategies. Our pyAT studies implement LOCO optics correction approach, while the current MAD-X studies [118] implement a response matrix on phase advance, dispersion and coupling RDTs. This comparison underscores the need to further investigate and compare different optics correction algorithms within the framework of PyAT as will be seen in the following section.

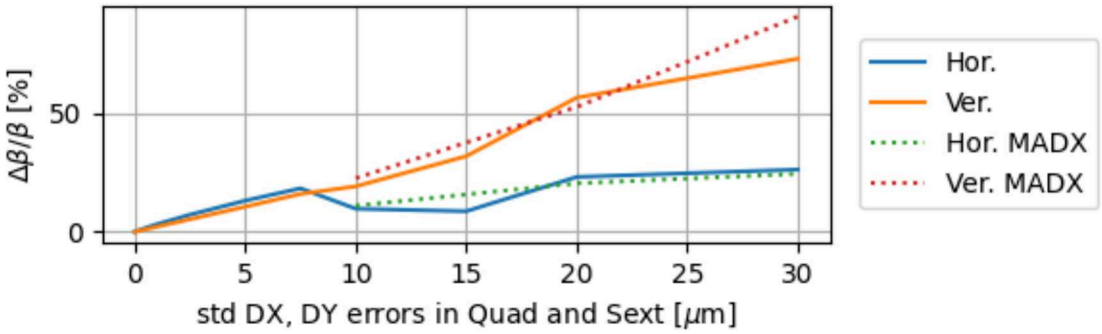

Figure 4.28: A comparison of β-beating between the PyAT and MAD-X codes, after assigning random misalignment errors (horizontal axis) and performing orbit and tune corrections, shows good agreement between the two codes. Solid lines represent results from AT, while dotted lines represent results from MAD-X [138].

4.6 LOCO vs. phase advance and coupling RDTs correction

We have begun exploring the impact of applying different optics correction algorithms and comparing them to our initially adopted algorithm, LOCO. Previously, we applied LOCO iterations to separately correct the beta beating, and coupling through vertical dispersion correction, utilizing all the normal quadrupoles and all skew quadrupoles at sextupoles. However, LOCO does not address phase advances and coupling resonance driving term corrections. We integrated phase advance correction into our scheme. The phase advance matching consequently results in beta beating correction as illustrated in Subsection 3.4.2. We also integrated coupling RDTs corrections into our scheme and compared the results of the new optics correction methods with those obtained using LOCO.

Initially, similar to LOCO, all normal quadrupoles were used to construct the phase advance and horizontal dispersion response matrices used for correction. However, applying the resultant relative quadrupole strengths failed to sufficiently correct the beta beating and horizontal dispersion. Therefore, we examined different corrector locations by using normal trim quadrupole components installed at every sextupole magnet.

4.6.1 Different correctors locations

We initially tested the new corrector locations using LOCO, which resulted in improved performance and a larger DA compared to the previous corrector locations. To further enhance LOCO performance, we followed the LOCO correction with coupling RDTs and vertical dispersion correction. We used the same skew quadrupoles located at the sextupoles, which were also used for LOCO dispersion correction iterations. This approach led to an improvement in the achieved vertical emittance. The achieved mean value of the vertical emittance for 50 seeds was 0.75 pm, compared to 5.99 pm when using only LOCO for optics correction.

Figure 4.29 shows the DA after correcting for random horizontal and vertical alignment errors, with a standard deviation of 100 μm, on the arc magnets of the baseline lattice. The correction was performed using LOCO followed by coupling RDTs and η_y correction with different sets of corrector locations, indicating an improvement in DA with the new set of corrector locations.

The achieved median DA of the seeds with the new set of corrector locations covers an area range from -20 to 20 horizontally and up to about 250 vertically in multiples of the horizontal and vertical beam sizes. Compared to DA median coverage with the old set of corrector locations ranged from -10 to 10 horizontally and up to about 170 vertically with the old set of corrector locations.

We then began to examine the impact of replacing LOCO with phase advance and horizontal dispersion correction using the normal trim quadrupoles at sextupoles followed by coupling RDTs and vertical dispersion correction. Table 4.12 demonstrate the optics parameters resulting from the new tuning scheme. The correction scheme achieved the design vertical emittance of 0.73 pm (mean value from 50 seeds) when random horizontal and vertical alignment errors with standard deviation of 100 μm were applied to arc components of the baseline lattice. Table 4.13 presents the results for the LCCO lattice. Table 4.14 illustrates the strengths of the horizontal and vertical orbit correctors, as well as the skew quadrupoles, after correction of random alignment errors with standard deviation of 100 μm in the arc components for the baseline lattice. For magnet design, low magnet strength is preferred because it translates into reduced power consumption, which in turn

leads to lower costs.

A histogram of the vertical emittance after correction, shown in Fig. 4.30, indicates that the corrected seeds primarily achieved vertical emittance values below 1 pm, with only a few seeds exceeding this threshold. It remains crucial to verify whether the resulting DA has also improved compared to LOCO followed by coupling RDTs and vertical dispersion correction. Figure 4.31 illustrates the achieved DA using phase advance + η_x and RDTs + η_y optics correction correction instead of LOCO for the baseline lattice. The achieved median DA of the seeds when applying phase advance + η_x and RDTs + η_y covers an area range from -20 to 20 horizontally and up to about 320 vertically in multiples of the horizontal and vertical beam sizes, the larger DA compared the LOCO DA in Fig. 4.29b highlights a better performance of the phase advance + η_x and RDTs + η_y corrections for the lattices and conditions we examined. Since the calculated DA so far does not include synchrotron radiation, a reduction in the nominal DA is expected when SR effects are considered due to particle losses. However, these DA calculations are useful for comparing different correction approaches. SR will be accounted for in the tuning simulation later in Sec. 4.8. Simulation with LOCO method typically takes significantly more time compared to simulations using phase advance + η_x and RDTs + η_y due to the large-dimensional matrices mathematical operations and the performed iterations.

In conclusion, while the new correction scheme including phase advance + η_x and RDTs + η_y correction improved the machine performance, as clarified by large DA area, this study does not assert that phase advance correction algorithm is superior to LOCO algorithm for optics correction of accelerators. LOCO minimize the deviation between model and measured ORMs, whereas by using trim quadrupoles at the sextupoles to correct the phase advance, the phase advance between all of the sextupoles (arc sextupole pairs and crab sextupoles) are better corrected than in case of LOCO so that the chromatic aberrations are not as significant, leading to better optics performance.

Table 4.12: Correction of random horizontal and vertical alignment errors with standard deviation of 100 μm on the arc components of the baseline with advance + η_x and RDTs + η_y correction for 50 seeds

		rms orbit x (μm)	rms orbit y (μm)	$\Delta\beta_x/\beta_x$ (%)	$\Delta\beta_y/\beta_y$ (%)	$\Delta\eta_x$ (mm)	$\Delta\eta_y$ (mm)	ε_{h} (nm)	ε_{v} (pm)
With err	mean	6224.83	7276.71	1.01e-06	0.000224	11985.76	73458.77	-	-
	std	2329.70	2922.48	7.31e-07	6.48e-05	7340.09	53557.01	-	-
After sextupoles ramping	mean	8.55	8.35	5.99	9.91	45.24	45.97	0.71	9.62
	std	0.45	0.46	2.13	3.87	16.80	14.87	0.01	4.83
RDTs & η_y cor.	mean	8.58	8.42	6.01	9.94	45.09	4.49	0.72	2.32
	std	0.45	0.46	2.16	3.92	16.811	1.65	0.01	2.91
Phase advance & η_x cor.	mean	8.55	8.35	0.35	0.79	2.95	4.36	0.71	0.89
	std	0.45	0.46	0.19	0.35	1.62	1.64	0.00	0.85
Final cor. result	mean	8.55	8.35	0.35	0.79	2.94	4.37	0.71	0.73
	std	0.45	0.46	0.19	0.35	1.61	1.64	0.00	0.85

Table 4.13: Correction of random horizontal and vertical alignment errors with standard deviation of 100 μm on the arc components of the LCCO with phase advance + η_x and RDTs + η_y for 50 seeds

		rms orbit x (μm)	rms orbit y (μm)	$\Delta\beta_x/\beta_x$ (%)	$\Delta\beta_y/\beta_y$ (%)	$\Delta\eta_x$ (mm)	$\Delta\eta_y$ (mm)
With errors	mean	8153.76	10714.79	0.28	0.16	11731.75	150637.32
	std	3278.44	4961.20	0.24	0.16	6708.75	119456.25
After sextupoles ramping	mean	5.24	4.98	1.57	2.26	12.35	16.51
	std	0.37	0.43	0.51	0.60	5.67	7.12
RDTs & η_y cor.	mean	9.68	7.30	1.57	2.33	13.05	1.24
	std	20.53	9.56	0.55	0.81	5.67	2.53
Phase advance & η_x cor.	mean	6.35	6.44	0.09	0.37	0.38	1.03
	std	4.90	6.81	0.24	1.33	0.58	1.62
Final cor. result	mean	6.50	5.62	0.09	0.38	0.37	0.89
	std	6.07	3.13	0.24	1.43	0.55	0.93

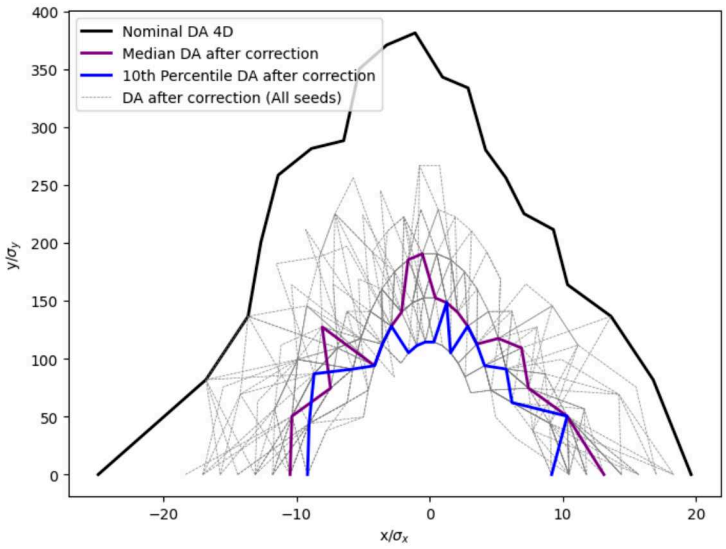

(a) Using LOCO with all normal quadrupoles followed by RDTs + η_y correction

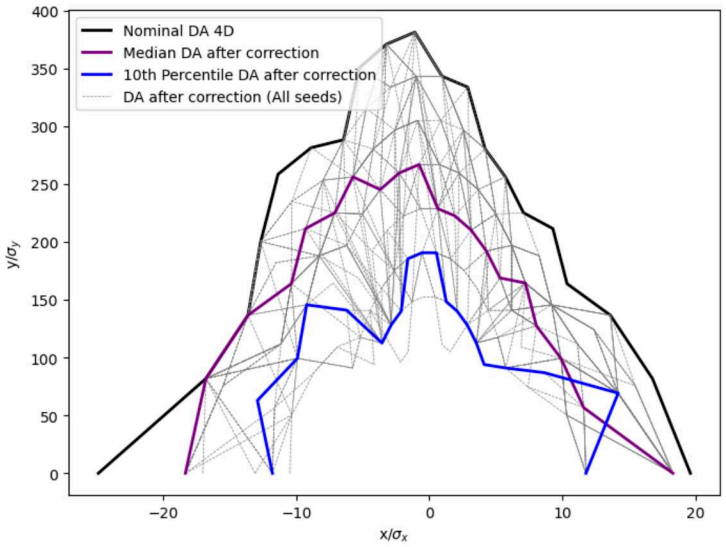

(b) Using LOCO with normal trim quadrupoles at sextupoles followed by RDTs + η_y correction

Figure 4.29: DA after correcting for random horizontal and vertical alignment errors, with a standard deviation of 100 μm, on the arc components of the baseline lattice for 50 seeds

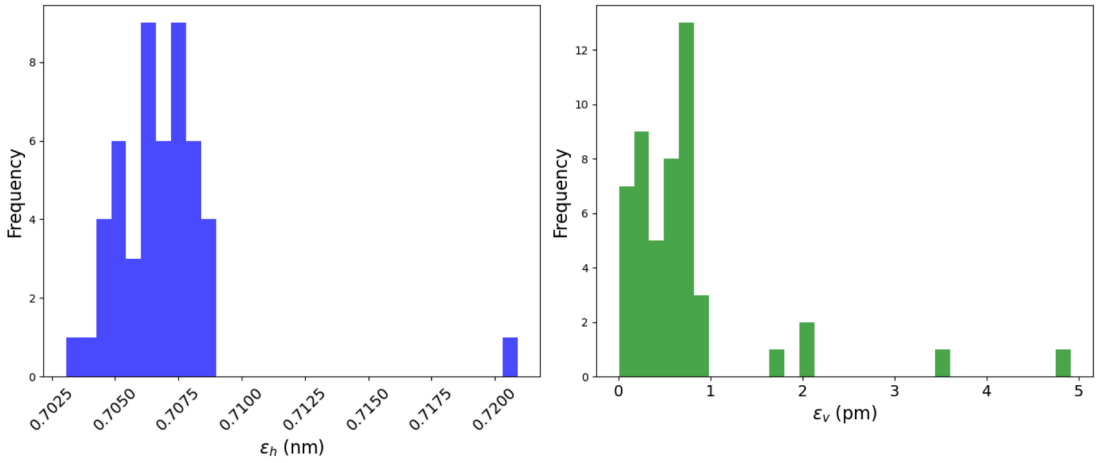

Figure 4.30: Horizontal (left) and vertical (right) emittance frequency distributions for 50 seeds, after following the correction chain using phase advance and RDTs + η_y, when random horizontal and vertical alignment errors with a standard deviation of 100 μm were applied to the arc magnets of the baseline lattice

Table 4.14: Mean rms and maximum strengths of orbit and skew quadrupole correctors used to correct random alignment errors with a standard deviation of 100 μm in the arc magnets of the baseline lattice, averaged over 50 seeds

Parameter	**Value (Mean)**
RMS horizontal orbit corrector strengths	2.13 μrad
Peak horizontal orbit corrector strengths	7.07 μrad
RMS vertical orbit corrector strengths	2.14 μrad
Peak vertical orbit corrector strengths	7.01 μrad
RMS skew quadrupole strengths	4.71 m^{-2}
Peak skew quadrupole strengths	2.40 $\times 10^{-4}\,\mathrm{m}^{-2}$

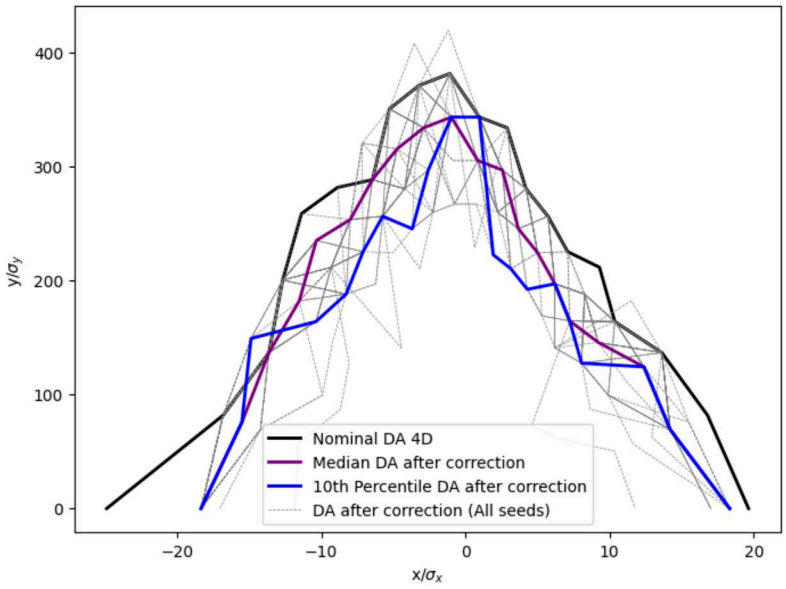

Figure 4.31: DA after correction of random horizontal and vertical alignment errors with a standard deviation of 100 μm on the arc components of the baseline lattice, using phase advance + η_x and RDTs + η_y corrections, for 50 seeds

4.7 Correction results including IR magnets alignment errors

The improvement in the tuning simulation results, achieved by incorporating phase advance and coupling RDTs correction, has encouraged us to explore the most challenging part of the FCC-ee: the interaction region (IR). This region is very sensitive to alignment errors due to the strong focusing magnets, strong sextupoles used for local chromaticity correction, and large beta function values. Initial results demonstrate the ability of the correction algorithm to handle horizontal and vertical random alignment errors of up to 100 μm standard deviation in the arc magnets and up to 5 μm standard deviation in the IR for the baseline lattice. Beyond this limit of errors in the IR, the correction procedure failed to achieve physical values. Table 4.15 shows the achieved optics parameters values after correction. We managed to improve the achieved optics values by further optimizing the correction schemes. This optimization involved performing iterations of phase advance + η_x and coupling RDTs + η_y corrections interleaved with correction of the orbit and tune to avoid resonances. The improved correction results with 100 μm standard deviation of random alignment errors in the arc and 5μm in the IR are presented in Tab. 4.16, where PyAT failed in obtaining results for the achieved emittance. Figure 4.32 indicates a reduction in the achieved DA area compared to Fig. 4.31 caused by introducing of additional 5 μm alignment errors in the IR magnets.

Table 4.15: Initial results of correction procedure after random horizontal and vertical displacement errors with a standard deviation of 100 μm in the arc magnets and 5 μm in the IR magnets of the baseline lattice were introduced for 50 seeds.

		rms orbit x (μm)	rms orbit **y** (μm)	$\Delta\beta_x/\beta_x$ %	$\Delta\beta_y/\beta_y$ %	$\Delta\eta_x$ (mm)	$\Delta\eta_y$ (mm)
Values	mean	15.60	13.87	0.59	3.47	4.47	7.80
	std	49.51	38.81	0.46	2.78	8.99	5.22

With the arc magnet misalignment errors of 100 μm rms and 5 μm rms misalignment of the IR magnets, the optics parameters after correction are already significantly larger (see

Table 4.16: Results after optimization, after correction of random horizontal and vertical displacement errors with standard deviation of 100 μm in the arc components and 5 μm in the IR components of the baseline lattice for 50 seeds

		rms orbit x (μm)	rms orbit **y** (μm)	$\Delta\beta_x/\beta_x$ %	$\Delta\beta_y/\beta_y$ %	$\Delta\eta_x$ (mm)	$\Delta\eta_y$ (mm)
Values	mean	8.510	8.310	0.056	0.086	0.125	0.242
	std	0.590	0.520	0.089	0.088	0.050	0.247

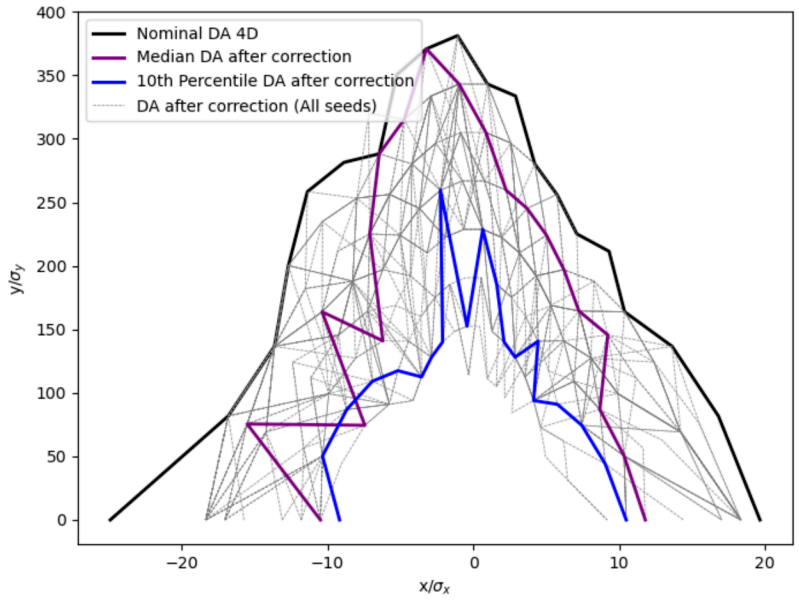

Figure 4.32: DA after correction of random horizontal and vertical displacement errors with standard deviation of 100 μm in the arc components and 5 μm on the IR components of the baseline lattice

Tab. 4.16) and the emittance could not be calculated. Further increasing the IR magnet misalignment errors to 10 μm rms resulted in 50% of the seeds failing due to unstable optics encountered during the correction procedure. These results indicate that the performed

global correction procedure for FCC-ee should include dedicated local corrections through developed IP tuning knobs [139], to achieve the desired optics values at the IPs. The challenges with IR magnets alignment tolerances and tuning will likely be addressed by a dedicated alignment system with feasible tolerances provided by the FCC-ee magnet alignment group to guide future tuning simulations.

4.8 Tuning studies with synchrotron radiation

So far, our tuning simulations have been conducted without considering radiation effects. To explore more realistic scenarios, we have evaluated the effectiveness of our tuning tools in the presence of SR, which has several effects on the beam dynamics as mentioned earlier in Subsection 1.2.4.

Including the SR in the tuning studies was done by using the AT command `enable_6d`. This command activates longitudinal motion and by default, enables radiation effects in the elements, activates RF cavities, and collective effects. Subsequently, we needed to introduce additional correction steps into our scheme, as outlined below:

Setting RF parameters

We activated the accelerating RF voltage to the appropriate level using the AT function `set_cavity`, and ensured that the cavity phase and frequency were correctly set. These settings were established using the AT functions `set_rf_frequency` and `set_cavity_phase`. The one RF system for the baseline lattice consist of 24 cavities with harmonic number 121200 and an RF voltage of 80 MV for each cavity.

Tapering

Tapering involves locally adjusting magnet strengths to compensate for beam energy variations. Performing tapering at this stage is necessary due to the large energy loss per turn caused by SR and the large saw-tooth distortion in the horizontal orbit, which can result

in beam loss. Individually tapering all magnets ensures that the orbit and optics remain nearly the same as they would be without the effects of radiation. This process is carried out using the `tapering` command, which scales the magnet strengths with the local energy to correct the closed orbit and optics errors introduced by SR. Figure 4.33 illustrates the large saw-tooth distortion in the horizontal closed orbit of the baseline lattice in the presence of SR, with an orbit rms value of 26.54 μm. Performing magnet tapering has reduced the horizontal orbit distortion to an rms value of 0.019 μm.

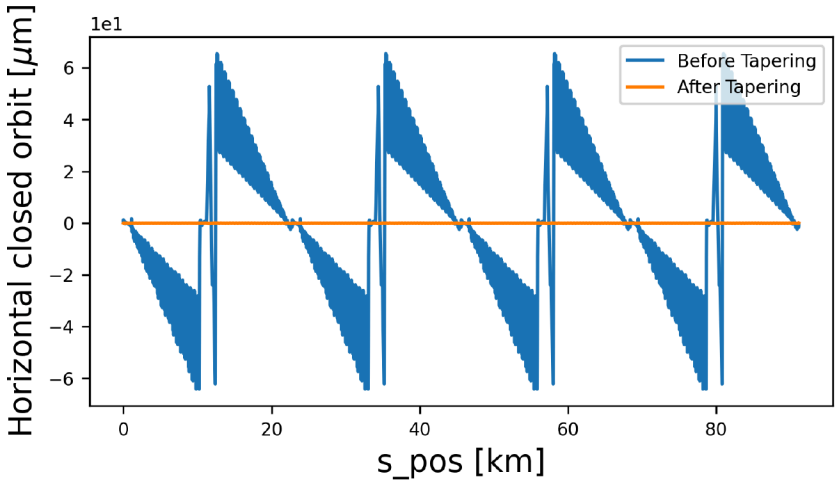

Figure 4.33: Horizontal closed orbit before and after applying magnets tapering

The nominal DA in the presence of SR compared to the nominal DA without radiation reveals a reduction in the DA area due to particle loss as seen in Fig. 4.34 for the baseline lattice. The calculated nominal DA with SR covers area range from -20 to 20 horizontally and up to 40 vertically in multiples of the horizontal and the vertical beam sizes: $\sigma_x = 4.526 \times 10^{-4}$ m and $\sigma_y = 1.819 \times 10^{-5}$ m respectively.

Trajectory correction (beam threading)

Correcting the intial trajectory, also known as beam threading, of the injected beam is crucial at this stage to establish a closed orbit and ensure that the beam circulates over a few turns. We utilized a PyAT-based function [140], which employs an SVD method using

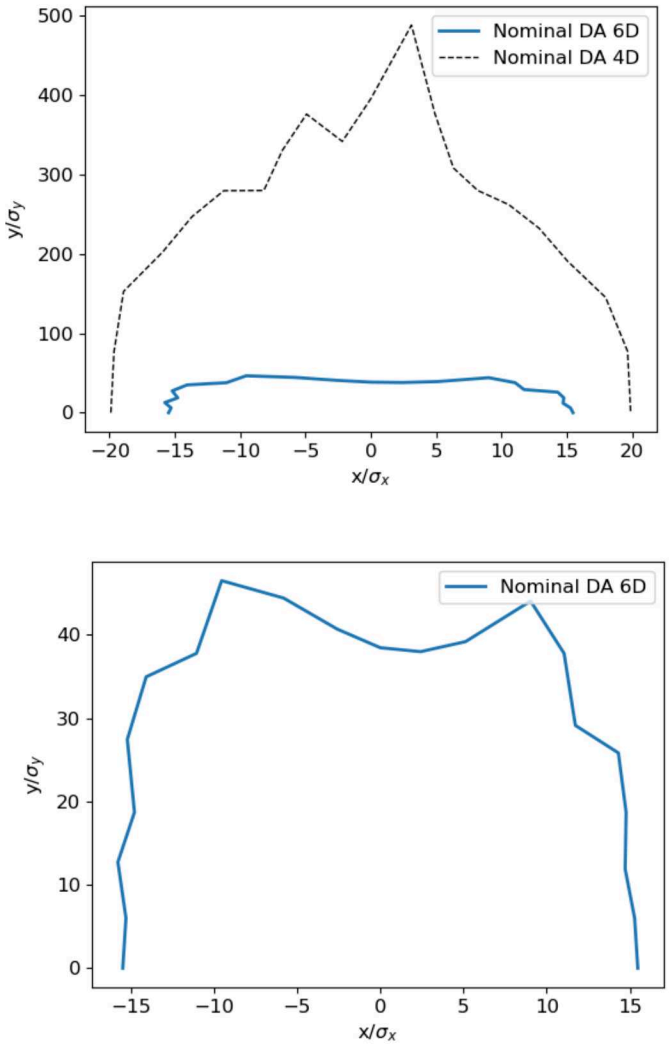

Figure 4.34: Comparison of nominal baseline lattice DA calculated at the first cavity: with and without SR (upper), zoomed-in view with SR (lower). The DA were calculated with 512 turns. The beam sizes are $\sigma_x = 4.526 \times 10^{-4}$ m and $\sigma_y = 1.819 \times 10^{-5}$ m.

the lattice's trajectory response matrix. This approach helps adjust the beam's trajectory and transitions the lattice from its initial uncorrected state to a state of full one-turn transmission.

After implementing the above mentioned steps to incorporate radiation effects, the improved tuning scheme including the phase advance + η_x and coupling RDTs + η_y optics correction were evaluated after applying horizontal and vertical random displacement errors with standard deviation of 100 μm to the arc quadrupoles and sextupoles and 150 μm to all dipoles, for 20 error seeds. Figure 4.35 illustrate the DA and vertical emittance achieved with the correction applied to the seeds. Figure 4.36 includes the effects of magnet tilt - that is rotation about the direction of the beam. As with the misalignments, the tilts are applied randomly via a Gaussian distribution truncated at 2.5 sigma. Random tilt errors with a standard deviation of 100 μ rad were introduced in the arc quadrupoles and sextupoles, while a standard deviation of 150 μ rad was applied to all dipoles. Figure 4.35 shows that 19 seeds achieved DA close to the nominal while one seed achieved smaller DA compared to the others. The vertical emittance distribution shows that all but one of the seeds were below 1 pm. The mean ε_y was 0.281 pm. Table 4.17 summarizes the achieved optics parameters after correction.

Table 4.17: Optics values of the baseline lattice after correction in presence of SR, with horizontal and vertical random displacement errors with standard deviation of 100 μm on arc quadrupole and sextupoles and 150 μm in all dipoles for 20 seeds

		rms orbit x (μm)	rms orbit y (μm)	$\Delta\beta_x/\beta_x$ (%)	$\Delta\beta_y/\beta_y$ (%)	$\Delta\eta_x$ (mm)	$\Delta\eta_y$ (mm)	ε_{h} (nm)	ε_{v} (pm)
Final cor. result	mean	9.9120	8.5602	1.1666	11.3845	13.3624	0.4630	0.7066	0.2813
	std	1.3112	0.6557	0.7179	7.1324	5.7058	0.5455	0.0024	0.4129

Although one error seed failed when tilt errors were added, the remaining seeds achieved DA close to the nominal as shown in Fig. 4.36, the vertical emittance distribution shows that the seeds achieved values below 0.55 pm with mean value of 0.181 pm. The optics parameter values after correction, including tilt, are illustrated in Tab. 4.18. As observed, some of the corrected optics parameters in Tab. 4.18 are better than those in Tab. 4.17. This improvement may be attributed to the tilting of elements like quadrupoles, which can produce skew quadrupole fields that help correct certain optics parameters, such as coupling, leading to better overall optics performance.

The correction results from this study show that including the SR effect leads to a 90% reduction in the DA in the vertical plane. Additionally, the inclusion of SR causes

Table 4.18: Optics values of the baseline lattice after correction in presence of SR, adding random tilt errors with standard deviation of 100 μm on arc quadrupole and sextupoles and 150 μm on all dipoles in addition to the misalignment described in Tab. 4.17 for 20 seeds

		rms orbit x (μm)	rms orbit y (μm)	$\Delta\beta_x/\beta_x$ (%)	$\Delta\beta_y/\beta_y$ (%)	$\Delta\eta_x$ (mm)	$\Delta\eta_y$ (mm)	ε_h (nm)	ε_v (pm)
Final cor. result	mean	9.3580	8.4064	0.9423	9.2066	8.4097	0.7843	0.7070	0.1811
	std	0.8505	0.3993	0.5410	5.3534	4.7790	0.6588	0.0024	0.1814

larger distortion in some optics parameters, such as horizontal dispersion, compared to the case without SR where the mean $\Delta\eta_x$ was 13.36 mm when SR is included compared to 2.94 mm without SR. This is because, with SR, particles displaced off the design orbit experience magnetic fields that differ from the design values, causing them to move along different orbits and resulting in increased horizontal dispersion. Nevertheless, the results demonstrate the feasibility of the tuning procedure in achieving the design parameters for the FCC-ee, even in the presence of SR.

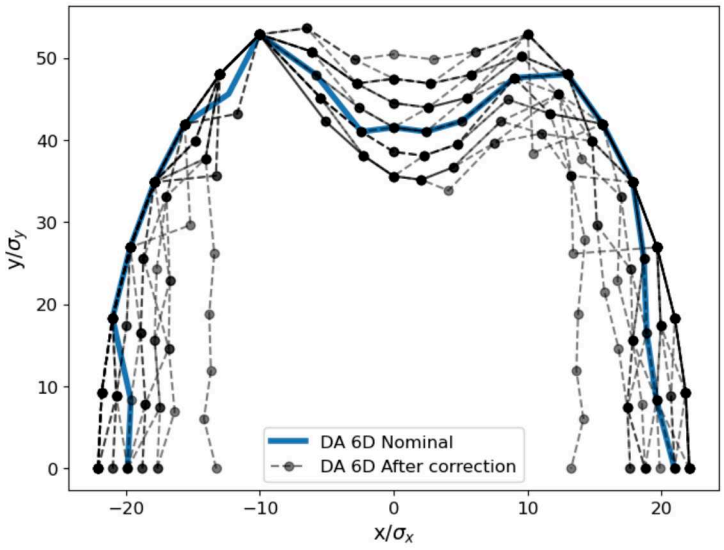

(a) DA

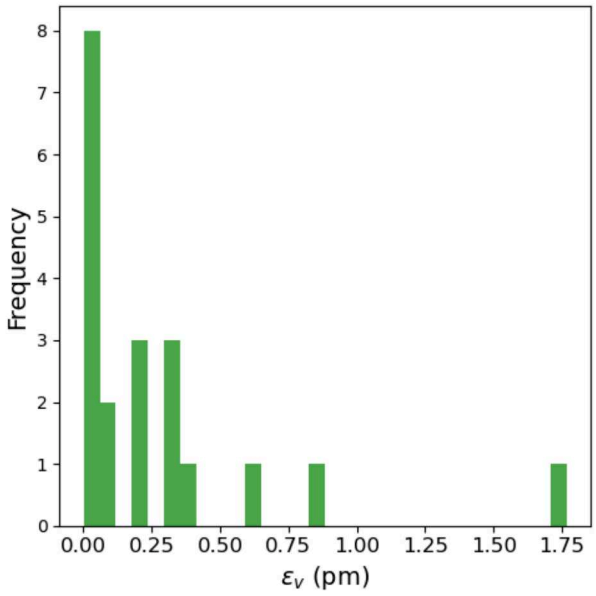

(b) Vertical emittance distribution

Figure 4.35: DA and vertical emittance distribution for 20 seeds after correction of random horizontal and vertical displacement errors in arc quadrupoles and sextupoles with a standard deviation of 100 μm, and a standard deviation of 150 μm in all dipoles in the presence of SR.

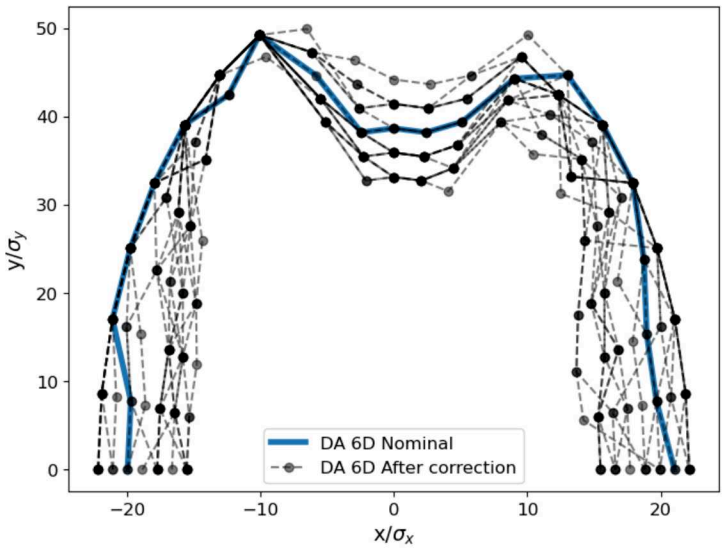

(a) DA

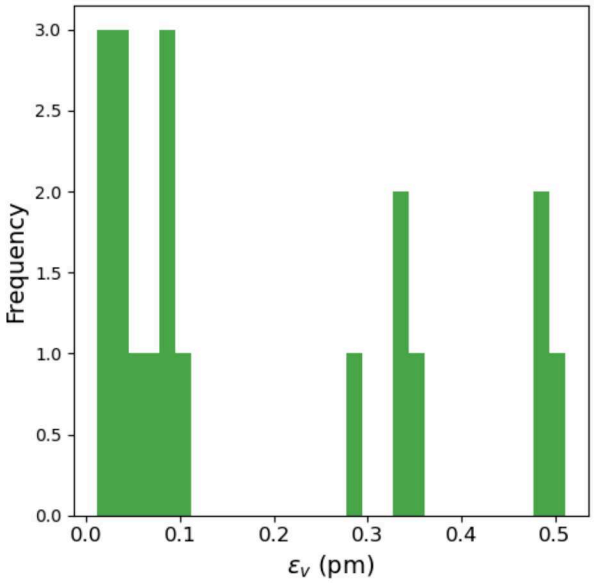

(b) Vertical emittance distribution

Figure 4.36: DA and vertical emittance after correction in presence of SR, adding random tilt errors with standard deviation of 100 μm on arc quadrupole and sextupoles and 150 μm on all dipoles in addition to the misalignment described in Tab. 4.17 for 20 seeds

4.9 BPMs alignment

In this study, we investigated the effects of introducing BPMs alignment in the optics tuning of the baseline lattice. To model the impact of BPM alignment on orbit measurements and subsequent corrections, we started by attaching BPMs to each quadrupole. To model BPM alignment, we introduced a transverse "Offset" field for each BPM element. The offset values for these BPMs were set to equal the assigned offset errors of the corresponding quadrupole. The horizontal and vertical BPM offsets represent the new reference orbit of the lattice, as illustrated in Fig. 4.37. This study considers an ideal scenario where the random misalignments of the BPMs are precisely equal to the assigned misalignments of the corresponding elements to which they are attached. As a result, there is no need for a Beam-Based Alignment procedure.

To perform orbit correction the orbit to be corrected is determined by subtracting the new reference orbit from the distorted orbit.

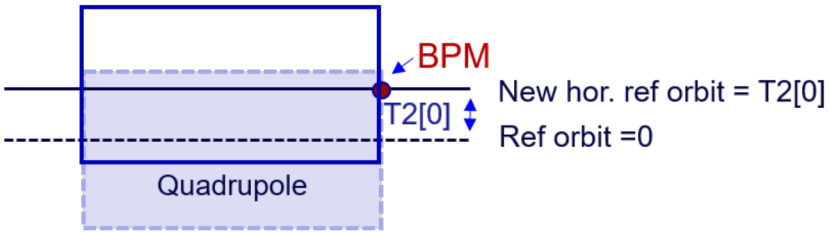

Figure 4.37: The horizontal displacement of the BPMs attached to the quadrupoles represents the new horizontal reference orbit (solid line). T2[0] in AT notation indicates the horizontal displacement of an element at its exit

Table 4.19: Assigned standard deviation of the random alignment errors

Elements	**Horizontal & vertical displacement**	**Tilt θ**
Arc quads and sextupoles	100 μm	100 μrad
All dipoles	150 μm	150 μrad
BPMs	Same as quads	-

Table 4.19 presents the assigned standard deviations of alignment errors. The tuning

simulation was performed and Tab. 4.20 shows the achieved optics parameter values after correction.

Table 4.20: Optics values of the baseline lattice after correction of random displacement and tilt errors as described in Tab. 4.19 for 50 seeds.

		rms orbit x (μm)	rms orbit y (μm)	$\Delta\beta_x/\beta_x$ (%)	$\Delta\beta_y/\beta_y$ (%)	$\Delta\eta_x$ (mm)	$\Delta\eta_y$ (mm)	ε_h (nm)	ε_v (pm)
Final cor. result	mean	24.786	24.395	1.122	10.821	14.523	1.159	0.706	0.054
	std	1.577	1.113	0.826	8.126	7.819	0.791	0.002	0.065

Figure 4.38 shows the DA and vertical emittance distribution after correction of 20 seeds. One seed failed to complete the simulation, and another seed resulted in a large vertical emittance of 300 pm and so was considered to have failed. The achieved DAs for 17 seeds were close to the nominal while one seed achieved smaller DA compared to the others. The achieved mean vertical emittance was 0.054 pm for 18 seeds.

Including BPM alignments in this study seems to add to the complexity by leading to the failure of some seeds; however, the successful seeds represents 90% of the total number of seeds and achieved mean vertical emittance of 0.054 pm, which is well below the design value of 0.7 pm.

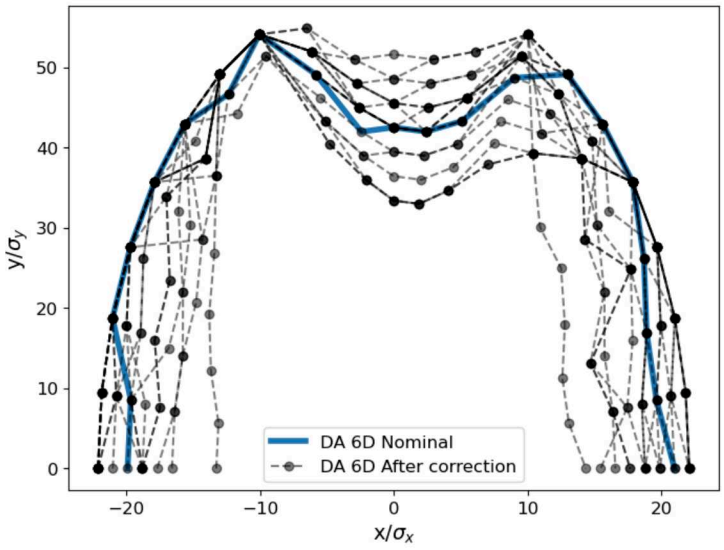

(a) DA

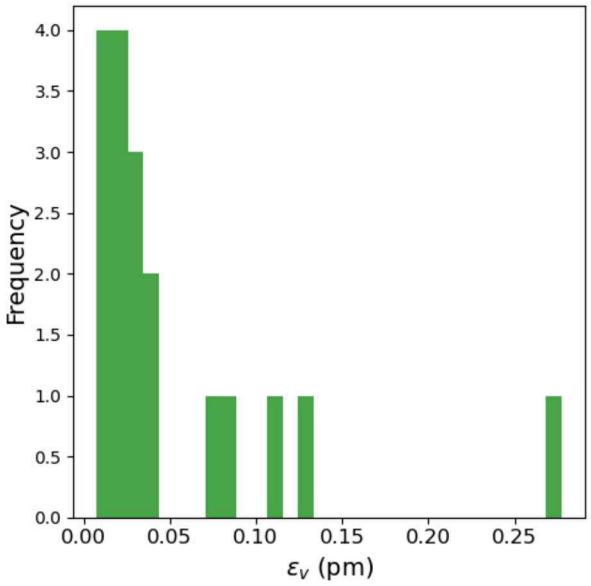

(b) Vertical emittance distribution

Figure 4.38: DA and vertical emittance after correction including BPMs aligned to quadrupoles (with one removed large outlier)

4.10 Results summary

In this chapter, we present our tuning results for the baseline and LCCO lattices at Z energy of 45.6 GeV.

We began by analyzing the sensitivity of optics parameters to alignment errors in magnets. The study shows that the optics distortion is lower for the arc region magnets in both the baseline and LCCO lattices compared to the IR magnets. In some cases, the LCCO optics parameters exhibits less sensitivity to errors in the arc components compared to the baseline.

Next, we examined our developed tuning procedure. The tuning process starts with turning off the sextupoles, which is a necessary step to remove the non-linear effects from the sextupoles at the beginning of the correction procedure. This step is followed by SVD orbit correction and tune fitting using all arc quadrupoles. After this step, the sextupole strengths are ramped up in one step to 100% of the design value, after that the sextupole strengths are varied to perform chromaticity correction.

After sextupole ramping and chromaticity correction linear optics correction was performed using LOCO. We developed a numerical code for LOCO method that includes iterations of beta beating correction until convergence using all normal quadrupoles, 20 horizontal and 20 vertical correctors, and all BPMs were used for ORMs and Jacobians calculations. Coupling correction iterations were performed using skew quadrupole correctors located at every sextupole.

Initial results show a reduction in the optics parameters distortion at each correction step. For the baseline lattice with horizontal and vertical random displacement errors having a standard deviation of 10 μm on arc magnets, the achieved vertical emittance mean for 50 seeds was 0.1295 pm, and 1.338 pm with errors of standard deviation of 20 μm. For the LCCO lattice, the results were 0.057 pm with 10 μm and 5.41 pm with 20 μm. Including random alignment errors of 10 μm standard deviation in IR magnets together with the arc resulted in larger deviations of the achieved optics parameters compared to the previous case, with factors ranging from approximately 2 to 10 times larger depending on the parameter for both LCCO and baseline.

We thoroughly optimized our correction procedure, aiming to achieve the design vertical emittance value (0.7 pm) for realistic alignment tolerances in the magnets. This optimization process involved many steps, start with selecting the most effective singular value cut off to perform SVD orbit correction. We examined the impact of increasing the number of chosen eigenvectors on reducing orbit and dispersion distortion. The study showed that a reduction in rms orbit and dispersion, indicating convergence of the correction, was observed with 1500 singular values for the baseline lattice and 2500 for the LCCO lattice.

We began ramping sextupole strength in steps of 10%, with further orbit and tune correction performed at every stage. Once at 100% of the design value, the sextupole strengths are varied to perform chromaticity correction. With these improvements, the correction procedure managed to increase the manageable alignment tolerances to a 30 μm standard deviation.

Performing orbit correction through the scheme followed by final tune and chromaticity fitting mitigated emittance growth and reduced the achieved mean vertical emittance of 50 seeds from 537 pm to 5.99 pm for the baseline and from 444 pm to 10.52 pm for the LCCO lattice when horizontal and vertical random alignments with a standard deviation of 100 μm in arc magnets were included.

We examined different correctors locations for LOCO by using normal trim quadrupoles located at sextupoles for beta beating correction. The tests showed an improvement in the achieved DA area. Following LOCO with coupling RDTs correction helped achieve a vertical emittance of 0.75 pm, compared to 5.99 pm when using only LOCO for optics correction for the baseline lattice, after correcting random horizontal and vertical alignment errors with a standard deviation of 100 μm on the arc magnets.

We participated in benchmarking study of commissioning simulations with errors and corrections between AT and MAD-X to understand and correct discrepancies between the two computer codes by applying the same errors and following the same correction steps. The study demonstrated good agreement between the two codes when the comparison were performed up to orbit correction step and the agreement between the codes suggests that different tuning simulation results are due to different optic correction algorithms. As

outcome of the benchmarking study we started to explore another optics correction algorithms by integrating phase advance and horizontal dispersion correction into our scheme instead of LOCO to correction the beta beating and horizontal dispersion. We also corrected coupling using skew quadrupoles located at sextupoles by correcting coupling RDTs and vertical dispersion.

The inclusion of the coupling RDTs and vertical dispersion into the correction procedure resulted in a vertical emittance of 0.73 pm (mean value for 50 seeds) when random horizontal and vertical alignment errors with a standard deviation of 100 μm were applied to the arc magnets of the baseline lattice. The nominal DA of the baseline lattice cover an area range from -20 to 20 horizontally and up to 380 vertically in multiples of the horizontal and vertical beam sizes, with beam sizes of $\sigma_x = 8.84 \times 10^{-6}$ m and $\sigma_y = 3.12 \times 10^{-8}$ m.

Subsequent phase advance and horizontal dispersion was applied after the RDTs and η_y correction, which resulting in the achieved median DA of the seeds covers an area range from -20 to 20 horizontally and up to about 320 vertically in multiples of the horizontal and vertical beam sizes. Comparatively, the DA median resulting from using LOCO and RDTs + η_y correction covered from -20 to 20 horizontally and up to about 250 vertically.

After correction of the baseline lattice, the rms horizontal orbit corrector strengths are 2.13 μrad, while the peak horizontal orbit corrector strengths reach 7.07 μrad. The rms vertical orbit corrector strengths are 2.14 μrad, and the peak value is 7.01 μrad. Additionally, the rms skew quadrupole strengths are 4.71 m^{-2}, and the peak skew quadrupole strengths are 2.40 $\times 10^{-4} m^{-2}$.

The achieved optics parameter variations for the LCCO after correction with random horizontal and vertical alignment errors of a standard deviation of 100 μm applied to the arc components of the lattice were lower compared to the baseline lattice, especially for horizontal and vertical beta beating and dispersion, with values of $\frac{\Delta\beta_x}{\beta_x}\,(\%) = 0.35$, $\frac{\Delta\beta_y}{\beta_y}\,(\%) = 0.79$, $\Delta\eta_x\,(\mathrm{mm}) = 2.94$, and $\Delta\eta_y\,(\mathrm{mm}) = 4.37$, for the baseline lattice. For the LCCO lattice, the corresponding values are $\frac{\Delta\beta_x}{\beta_x}\,(\%) = 0.10$, $\frac{\Delta\beta_y}{\beta_y}\,(\%) = 0.39$, $\Delta\eta_x\,(\mathrm{mm}) = 0.38$, and $\Delta\eta_y\,(\mathrm{mm}) = 0.89$.

For the baseline lattice we examined the IR region by introducing 100 μm standard deviation of random alignment errors in the arc magnets and 5 μm standard deviation

of random alignment errors in the IR magnets. Optimization of the correction procedure involved performing iterations of phase advance and coupling corrections interleaved with corrections of orbit and tune to avoid resonances helped in improving the achieved parameters values after correction. However, the DA covered an area range from -10 to 10 horizontally in multiples of the horizontal beam size. Increasing the standard deviation of errors in the IR region to 10 μm led to a failure of 50% of the seeds. The performed global correction will need further refinement through IP tuning knobs to achieve the desired optics at the interaction points. Alignment errors and tuning challenges in the IR magnets will likely be addressed by a dedicated alignment system, with feasible tolerances provided by the FCC-ee magnet alignment group to guide future tuning simulations.

We further explored more realistic conditions by including Synchrotron Radiation (SR). The nominal DA with SR covers an area range from -20 to 20 horizontally and up to 40 vertically in multiples of the horizontal and vertical beam sizes: $\sigma_x = 4.526 \times 10^{-4}$ m and $\sigma_y = 1.819 \times 10^{-5}$ m, respectively.

The correction procedure was also examined under conditions of radiation effects. This was done by setting RF parameters and applying tapering to the magnets. Under these conditions, initial trajectory correction was found to be necessary. The correction scheme was applied to correct horizontal and vertical random displacement errors with a standard deviation of 100 μm on arc quadrupoles and sextupoles and 150 μm in all dipoles of the baseline optics. Out of 20 seeds, 19 seeds achieved a vertical emittance distribution below 1 pm, with a mean value of 0.281 pm. The DA areas for 19 seeds were close to the nominal, except for one seed whose DA area was reduced by a factor of 1.8 in the horizontal plane.

We added horizontal and vertical random tilt errors with a standard deviation of 100 μm on arc quadrupoles and sextupoles, and 150 μm in all dipoles of the baseline optics, to the displacement errors. One seed failed to complete the simulation, while the remaining 19 seeds achieved vertical emittance below 0.55 pm with a mean value of 0.18 pm. The achieved DA was close to the nominal for 19 seeds.

We investigated the effect of BPM alignment by attaching BPMs to the quadrupoles. The simulation of the correction procedure with random displacement and tilt errors with a standard deviation of 100 μm on arc quadrupoles and sextupoles, and 150 μm in all

dipoles, including BPM alignment to quadrupoles for the baseline lattice, resulted in one out of 20 seeds failing. After correcting 20 seeds and excluding a large outlier, the DA for 17 seeds was near the nominal values, while one seed had a smaller DA. The mean vertical emittance for 18 seeds was 0.054 pm. Including BPM alignments increased complexity and caused some seeds to fail, however approximately 90% of the seeds succeeded and achieved a mean vertical emittance below the design value of 0.7 pm.

The outcomes of the studies presented in this chapter demonstrate the feasibility of the developed tuning procedure in achieving the design parameter values while accounting for random displacement and tilt errors with standard deviations of 100 μm on arc quadrupoles and sextupoles and 150 μm in all dipoles, including BPM alignment to quadrupoles.

Looking ahead, future outlooks aim to refine these correction procedures under more realistic conditions, including solenoid errors, scale imperfections in BPMs, investigating the inclusion of girders and their imperfections and long-range misalignments. Additionally, addressing beam-beam effects, impact of the developed IP tuning knobs on the error tolerances of the IR, and exploring different algorithms and computational methods to optimize the performance of FCC-ee will be essential.

Chapter 5

Conclusion

In this thesis, we addressed the optics tuning of the proposed electron-positron Future Circular Collider (FCC-ee), a machine with a circumference of about 90 km. This collider represents the next generation of higher-performance particle colliders, aiming to push the limits of the achieved luminosity. It combines research efforts from several international institutes and laboratories under the leadership of CERN, and will allow for ultra-precise measurements of the discovered particles.

Being a very ambitious project does not remove the fact that the FCC-ee faces a series of challenges. One of these challenges is to the beam dynamics, which arises from the machine components imperfections. FCC-ee will consist of vast array of magnets, each having its own impact if imperfect, potentially preventing the machine from achieving the desired performance. Misalignments and field errors are critical concerns for machines like the FCC-ee and 4th-generation light sources, which are highly sensitive to such imperfections. Research into accelerator optics measurement techniques, and correction methods has been extensive and ongoing. Numerous optics correction techniques have been developed over years to address this challenge effectively. It is crucial to develop a strong correction procedure for FCC-ee unique requirements and to define the tolerance requirements for the machine and large optics tuning simulation campaigns are needed to achieve this.

In this thesis, we explored the potential of several correction algorithms for FCC-ee optics tuning. We developed our own correction procedure, tailored it to the highly-sensitve

FCC-ee lattice, and conducted comprehensive simulation studies. We compared the effectiveness of some correction techniques over others for FCC-ee. Moreover, we conducted a comparison between two proposed machine optics designs for the future collider. The thesis managed to achieve the design parameters for realistic alignment imperfections in the machine arc region magnets.

Looking ahead, we aim to refine these correction procedures under more realistic conditions. Advanced algorithms and computational methods will continue to be explored. Challenges for FCC-ee still lie ahead, specifically in its interaction region, where the strongest magnets are located to focus the beam at the collision point. This makes the region very sensitive to any imperfections.

The outcomes of this thesis not only contribute to the optimization of the FCC-ee's performance but also can be used for future next-generation colliders and light sources.

Bibliography

[1] P. Janot and C. Grojean, Searches for new physics, FCC: The physics case, 2024, FCC: The Physics Case on CERN Courier.

[2] H. Wiedemann, *Particle accelerator physics*, 4 ed. (Springer International Publishing, Cham, Switzerland, 2015).

[3] K. W. Smith *et al.Bibliometric analysis of publications in experimental particle physics on cosmic rays and with accelerators* Vol. 30 (, 2023), Publications in experimental particle physics on cosmic rays and with accelerators.

[4] Future Circular Collider Conceptual Design Report CDR, 2019, FCC CDR on CERN Website.

[5] W. Hillert, *Transverse Linear Beam Dynamics* (Proceedings of the CERN–Accelerator–School Course: Introduction to Accelerator Physics, 2021), arXiv:2107.02614v2,.

[6] J. T. Tanabe, *Iron Dominated Electromagnets: Design, Fabrication, Assembly, and Measurements* (World Scientific Publishing, 2005), SLAC Report SLAC-R-754.

[7] T. Zickler, *Basic Design and Engineering of Normal-Conducting, Iron-Dominated Electromagnets* (CERN-2010-004, pp. 65-102, 2011), arXiv:1103.1119.

[8] S. Russenschuck, *Electromagnetic Design of Accelerator Magnets* (CAS - CERN Accelerator School: Basic Course on General Accelerator Physics, 2005), CERN Document Server.

[9] I. S. Grant and W. R. Phillips, *Electromagnetism* (John Wiley & Sons, 1990), Electromagnetism on Archive.org.

[10] M. Martini, *An Introduction to Transverse Beam Dynamics in Accelerators* (Lectures given at the Joint Universities Accelerator School, Archamps, Geneva, Switzerland, 1996), CERN Document Server.

[11] K. Wille, *The Physics of Particle Accelerators: An Introduction* (Oxford University Press Inc., New York, 2001), Oxford University Press.

[12] M. G. Minty and F. Zimmermann, *Measurement and Control of Charged Particle Beams* (Springer, 2011), Springer Link.

[13] E. D. Courant and H. S. Snyder*Theory of the Alternating-Gradient Synchrotron* Vol. 3 (, 1958), Annals of Physics on ScienceDirect.

[14] A. Wolski, *Beam Dynamics in High Energy Particle Accelerators* (World Scientific Publishing, 2014), World Scientific.

[15] A. Verdier, *Chromaticity* (CAS - CERN Accelerator School: Fourth Advanced Accelerator Physics Course, pp. 204-225, 2014).

[16] Y. H. Chin, A. W. Chao, M. M. Blaskiewicz, and Y. Shobuda*Chromaticity Effects on Head-Tail Instabilities For Broad-band Impedance Using Two Particle Model, Vlasov Analysis and Simulations* Vol. 20 (, 2017), Physical Review Accelerators and Beams.

[17] V. Smaluk, G. Bassi, A. Blednykh, and A. Khan*Combined Effect of Chromaticity and Feedback on Transverse Head-Tail Instability* Vol. 24 (American Physical Society, 2021), Physical Review Accelerators and Beams.

[18] B. Holzer, *Introduction to Transverse Beam Optics* (The Joint Universities Accelerator School (JUAS) Lectures, 2023), Indico CERN.

[19] S. Turner, editor, *Synchrotron Radiation and Free Electron Lasers*CERN Accelerator School CAS (CERN, Geneva, 1998), CERN.

[20] A. W. Chao, *Handbook of Accelerator Physics and Engineering* (World Scientific, 2013), CERN.

[21] A. Wolski, *Low-Emittance Storage Rings* (CERN Accelerator School: Advanced Accelerator Physics Course: Trondheim, Norway, August 18-29, 2013, 2014, pp. 245-294, 2013), Inspire HEP.

[22] K. W. Robinson, *Radiation Effects in Circular Electron Accelerators* (Phys. Rev., vol. 111, pp. 373–380, Jul 1958, 1958), Semantic Scholar.

[23] L. Rivkin, *Electron Dynamics with Synchrotron Radiation* (CERN Accelerator School: Introduction to Accelerator Physics, 2012), CERN Accelerator School.

[24] R. D. Ruth, *Single Particle Dynamics and Nonlinear Resonances in Circular Accelerators* (Springer Berlin Heidelberg, 2007), Springer, Lecture Notes in Physics.

[25] H. Bartosik, Y. Papaphilippou, and A. Wolski, *First Taste of Nonlinear Beam Dynamics* (Proceedings of the CERN–Accelerator School course CAS: Introduction to Accelerator Physics, 2022), arXiv.

[26] Accelerator toolbox 0.6.2 documentation, GitHub.io, Accessed: 2024-7-8.

[27] A. Terebilo, Accelerator modeling with MATLAB accelerator toolbox, in *PACS2001. Proceedings of the 2001 Particle Accelerator Conference (Cat. No.01CH37268)*, IEEE, 2002.

[28] P. Tenenbaum, Lucretia: A matlab-based toolbox for the modelling and simulation of single-pass electron beam transport systems, in *Proceedings of the 2005 Particle Accelerator Conference*, IEEE, 2006.

[29] Website of MATLAB, MathWorks.com, Accessed: 2024-4-8.

[30] Website of Accelerator Toolbox AT, PyPI, Accessed: 2024-7-8.

[31] G. A. et al., *Observation of a new particle in the search for the Standard Model Higgs boson with the ATLAS detector at the LHC* (Physics Letters B, vol. 716, no. 1, pp. 1–29, 2012), arXiv:1207.7214.

[32] A. R. Francia *et al.*, Physical Review Accelerators and Beams **27** (2024), Super Proton Synchrotron.

[33] P. Janot and C. Grojean, Tunnelling to the future, 2024, CERN Courier.

[34] C. S. G. Collaboration, *CEPC Conceptual Design Report: Volume 2 - Physics & Detector* (, 2018), arXiv:1811.10545, 424 pages.

[35] I. I. D. Team, International linear collider, 2024, ILC Website.

[36] J. Hewett, *FCC Week Keynote* (Presented at FCC Week, 10-14 June 2024, San Francisco, USA, 2024), Indico.

[37] *SuperKEKB Project* (, 2021), SuperKEKB Website, Accessed: 26th July 2021.

[38] W. Herr and B. Muratori, *Concept of Luminosity* (CAS, CERN Accelerator School: Intermediate Accelerator Physics, 2006), CERN Document Server, Rep. No. CERN-2006-002, pp. 361–378.

[39] E. Keil, *Beam-Beam Dynamics* (CERN Accelerator School, Rhodes 1993, CERN 95-06, 1995), CERN Document Server.

[40] W. Herr and T. Pieloni, *Beam–Beam Effects* (CERN Accelerator School, CERN–2014–009, 2013), CERN Document Server.

[41] S. Myers, *The LEP Collider, from design to approval and commissioning* (John Adams' memorial lecture, 1991), CERN Document Server.

[42] V. Shiltsev and F. Zimmermann*Modern and future colliders* Vol. 93 (, 2021), arXiv:2003.09084.

[43] M. Bai, V. Shiltsev, G. White, and F. Zimmermann, Ultimate limit of future colliders, 2022, Semantic Scholar.

[44] F. Gianotti, *FCC Timeline from the opening session at FCC Week 2024* (, 2024), Indico.

[45] M. Benedikt *et al.*, *Future Circular Collider study, Volume 3: The Hadron Collider (FCC-hh) Conceptual Design Report* (CERN, in Eur. Phys. J. ST. 228, pp. 755–1107, 2019, 2019), DOI: 10.1140/epjst/e2019-900087-0.

[46] K. Oide*Electron-Positron Circular Colliders, Rev. Accel. Sci. Tech.* Vol. 7 (, 2014), 10.1142/S1793626814300035.

[47] K. Oide, *Optics performance, beam lifetime, injection rate, and vibration* (, Nov 13–15, 2023), FCCIS WP2 Workshop.

[48] K. Oide, M. Aiba, and et al.*Design of beam optics for the Future Circular Collider e^+e^- collider rings* Vol. 19 (American Physical Society (APS), 2016), DOI: 10.1103/PhysRevAccelBeams.19.111005.

[49] G. Roy, Metrics for lattice comparison, 2023, Metrics for Lattice Comparison.

[50] S. A. M. B. e. a. K. Oide, M. Aibab, *Beam Optics for FCC-ee Collider Ring* (, 2017).

[51] K. Oide, Information about FCC-ee baseline optics, 2024, Personal communication, 2024.

[52] J. Keintzel *et al.*, *FCC-ee Lattice Design* (JACoW, 2023), 10.18429/JACoW-eeFACT2022-TUYAT0102.

[53] P. Raimondi, *Local Chromatic Correction Arc Final Focus FCC Optic* (FCC Workshop, 2014), Local Chromatic Correction Arc Final Focus FCC Optic.

[54] P. Raimondi, Arc and long straight sections beam dynamics studies, 2022, https://indico.cern.ch/event/1213879/.

[55] H. Garcia *et al.*, *FCC-ee Final Focus with Chromaticity Correction* (JACoW, Geneva, Switzerland, 2014), IPAC2014 Paper.

[56] P. Raimondi and A. Seryi, Phys. Rev. Lett. **86**, 3779 (2001), Novel Final Focus Design for Future Linear Colliders.

[57] P. Raimondi, *Final Focus design with local compensation of geometric and chromatic aberrations* (FCCIS 2022 Workshop, 5 Dec. 2022, 2022), FCCIS 2022 Workshop.

[58] CERN, FCC-ee Lattice Reference Parameters, 2024, FCC-ee Lattice Reference Parameters, [Online; accessed 1-May-2023].

[59] A. Chao, *Physics of Collective Beam Instabilities in High Energy Accelerators* (John Wiley and Sons, 1993), https://inspirehep.net/literature/362224.

[60] P. Raimondi, Status on superb effort, presentation at the 2nd workshop on super b-factory, frascati, italy, 2006, Talk.

[61] K. Hirata*Analysis of Beam-Beam Interactions with a Large Crossing Angle* Vol. 74 (American Physical Society, 1995), https://eprint.aps.org/doi/10.1103/PhysRevLett.74.2228.

[62] M. Zobov*Crab Waist Collision Scheme: A Novel Approach for Particle Colliders* Vol. 747 (IOP Publishing, 2016), http://dx.doi.org/10.1088/1742-6596/747/1/012090.

[63] P. Raimondi, D. N. Shatilov, and M. Zobov, Beam-beam issues for colliding schemes with large piwinski angle and crabbed waist, 2007, physics/0702033.

[64] M. A. V. Garcia and F. Zimmermann, The European Physical Journal Plus (2019), DOI: 10.1140/epjp/s13360-021-01485-x.

[65] I. Agapov and C. Niebuhr, *Experimental Tests of FCC-ee Performance-Enabling Techniques* (, 2023), Unpublished.

[66] D. Shatilov, Overview of beam-beam effects at fcc-ee, 2017, Overview of Beam-Beam Effects at FCC-ee.

[67] D. Shatilov, Beam-beam effects and parameter optimization for fcc-ee, 2019, Beam-Beam Effects and Parameter Optimization for FCC-ee.

[68] E. Courant and H. Snyder, Annals of Physics **3**, 1 (1958), Theory of the Alternating-Gradient Synchrotron.

[69] R. Tomás, M. Aiba, A. Franchi, and U. Iriso*Review of Linear Optics Measurement and Correction for Charged Particle Accelerators* Vol. 20 (American Physical Society, 2017), 10.1103/PhysRevAccelBeams.20.054801.

[70] N. Catalán Lasheras, H. Mainaud-Durand, and M. Modena, *Measuring and aligning accelerator components to the nanometre scale* (, 2014), Measuring and aligning accelerator components to the nanometre scale.

[71] S. Turner, *CAS - CERN Accelerator School : Measurement and Alignment of Accelerator and Detector Magnets: Anacapri, Italy 11 - 17 Apr 1997* (CERN, Geneva, 1998), Measurement and Alignment of Accelerator and Detector Magnets.

[72] T. Charles, Emittance tuning simulations and next steps, 2020, Emittance Tuning Simulations and Next Steps.

[73] A. Wolski, *Beam Dynamics in High Energy Particle Accelerators* (Imperial College Press, London, England, 2014).

[74] G. Ripken and F. Willeke*On the Impact of Linear Coupling on Nonlinear Dynamics* Vol. 27 (, 1990), On the Impact of Linear Coupling on Nonlinear Dynamics.

[75] F. Willeke and G. Ripken, *Methods of Beam Optics* (DESY, Hamburg, 1988), Methods of Beam Optics.

[76] G. Guignard, *The General Theory of All Sum and Difference Resonances in a Three-Dimensional Magnetic Field in a Synchrotron*CERN Yellow Reports: Monographs (CERN, Geneva, 1976), The General Theory of All Sum and Difference Resonances in a Three-Dimensional Magnetic Field in a Synchrotron.

[77] R. Bartolini and F. Schmidt*Normal form via tracking or beam data* Vol. 59 (, 1998), Betatron coupling: Merging Hamiltonian and matrix approaches.

[78] R. Calaga, R. Tomás, and A. Franchi*Betatron coupling: Merging Hamiltonian and matrix approaches* Vol. 8 (American Physical Society, 2005), Betatron coupling: Merging Hamiltonian and matrix approaches.

[79] M. Wendt, *BPM Systems: A brief Introduction to Beam Position Monitoring* (, 2020), Beam Diagnostic Requirements: an Overview.

[80] Y. C. Chao, Orbit correction methods - basic formulation, current applications at jefferson lab, and future possibilities, 1999, Orbit Correction Methods - Basic Formulation, Current Applications at Jefferson Lab, and Future Possibilities.

[81] V. Ziemann, *Hands-on Accelerator Physics using Matlab* (CRC Press, 2019), https://de.mathworks.com/academia/books/hands-on-accelerator-physics-using-matlab-ziemann.html.

[82] G. White, T. Himel, and H. Shoaee, A hybrid numerical method for orbit correction, in *Proceedings of the 1997 Particle Accelerator Conference (Cat. No.97CH36167)* Vol. 2, pp. 2425–2427 vol.2, 1997, A Hybrid Numerical Method for Orbit Correction.

[83] W. Press, B. Flannery, S. Teukolsky, and W. Vetterling, *Numerical Recipes in C* (Cambridge University Press, Cambridge, England, 1988).

[84] G. Golub and W. Kahan*Calculating the Singular Values and Pseudo-Inverse of a Matrix* Vol. 2 (, 1965), Calculating the Singular Values and Pseudo-Inverse of a Matrix.

[85] S. Banerjee and A. Roy, *Linear Algebra and Matrix Analysis for Statistics, Texts in Statistical Science (1st ed.)* (Chapman and Hall/CRC, 2014), Linear Algebra and Matrix Analysis for Statistics, Texts in Statistical Science (1st ed.).

[86] B. Autin and Y. Marti, *Closed Orbit Correction of A.G. Machines using a Small Number of Magnets* (, 1973), Closed Orbit Correction of A.G. Machines using a Small Number of Magnets.

[87] N. Blaskovic Kraljevic and D. Schulte, *Beam Orbit Correction in the CLIC Main Linac using a Small Subset of Correctors* (, 2019), Beam Orbit Correction in the CLIC Main Linac using a Small Subset of Correctors.

[88] R. Assmann, P. Raimondi, G. Roy, and J. Wenninger*Emittance Optimization with Dispersion Free Steering at LEP* Vol. 3 (American Physical Society, 2000), 10.1103/PhysRevSTAB.3.121001.

[89] M. Aiba and e. a. Michael B, *Study of Beam Based Alignment and Orbit Feedback for SwissFEL* (, 2010), Study of Beam Based Alignment and Orbit Feedback for SwissFEL.

[90] A. Madur, P. Brunelle, A. Nadji, and L. S. Nadolski, *Beam-based Alignment for the Storage Ring Multipoles of Synchrotron SOLEIL* (, 2006), Beam-based Alignment for the Storage Ring Multipoles of Synchrotron SOLEIL.

[91] X. Huang*Simultaneous Beam-based Alignment Measurement for Multiple Magnets by Correcting Induced Orbit Shift* Vol. 25 (American Physical Society, 2022), 10.1103/PhysRevAccelBeams.25.052802.

[92] Z. Martí *et al.*, Fast orbit response matrix measurements at alba, 2017, Fast Orbit Response Matrix Measurements at ALBA.

[93] G.-L. Wang and e. a. Kemin Chen, Nuclear Science and Techniques (2024), Beam Based Alignment using a Neural Network.

[94] X. Huang, Beam-based alignment (bba) simulations for the fcc-ee lattice, 2023, Beam-based Alignment (BBA) Simulations for the FCC-ee Lattice.

[95] A. Hofmann and B. Zotter, *Measurement of the beta-functions in the ISR* (ISR-TH-AH-BZamb, Run: 640-641-642, 1975), Measurement of the beta-functions in the ISR.

[96] M. Kuhn, Transverse emittance measurement and preservation at the lhc, 2016, Transverse Emittance Measurement and Preservation at the LHC, Presented 20 Jun 2016.

[97] A. Franchi, Error analysis of linear optics measurements via turn-by-turn beam position data in circular accelerators, 2018, arXiv:1603.00281.

[98] R. Tomás, O. S. Brüning, R. Calaga, and S. Peggs, Procedures and accuracy estimates for beta-beat correction in the lhc, 2006, Proceedings of the LHC.

[99] J. Safranek and M. Lee, *Calibration of the X-ray Ring Quadrupoles, BPMs, and Orbit Correctors Using the Measured Orbit Response Matrix* (, 1994), SLAC-PUB-6442.

[100] J. Safranek*Experimental Determination of Storage Ring Optics Using Orbit Response Measurements* Vol. 388 (, 1997), Experimental Determination of Storage Ring Optics Using Orbit Response Measurements.

[101] W. J. Corbett, M. J. Lee, and V. Ziemann, *A Fast Model-Calibration Procedure for Storage Rings* (, 1993), SLAC-PUB-6111.

[102] Y. Roblin, Calibrating transport lines using loco techniques, 2011, Proceedings of the LHC.

[103] V. Smaluk *et al.*, Experimental crosscheck of algorithms for magnet lattice correction, 2016, Proceedings of the LHC.

[104] J. Safranek, G. Portmann, A. Terebilo, and C. Steier, *MATLAB-based LOCO* (, 2002), MATLAB-based LOCO.

[105] G. Bohm and G. Zech, *Introduction to Statistics and Data Analysis for Physicists*, Third ed. (Deutsches Elektronen-Synchrotron Hamburg, Germany, 2014).

[106] A. Björck, *Numerical Methods for Least Squares Problems* (SIAM, Philadelphia, 1996), 10.1137/1.9781611971484.

[107] J. J. More, The levenberg-marquardt algorithm: Implementation and theory, 1977, Proceedings of the LHC.

[108] D. W. Marquardt, Journal of The Society for Industrial and Applied Mathematics **11**, 431 (1963), Journal of The Society for Industrial and Applied Mathematics 11, 431-441 (1963).

[109] D. D. Morrison, Methods for nonlinear least squares problems and convergence proofs, 1960, Proceedings of the LHC.

[110] R. Fletcher, A modified marquardt subroutine for non-linear least squares, 1971, A modified Marquardt subroutine for non-linear least squares.

[111] M. K. Transtrum, B. B. Machta, and J. P. Sethna*Geometry of Nonlinear Least Squares with Applications to Sloppy Models and Optimization* Vol. 83 (American Physical Society, 2011), Phys. Rev. E 83, 036701 (2011).

[112] M. K. Transtrum and J. P. Sethna, Improvements to the levenberg-marquardt algorithm for nonlinear least-squares minimization, 2012, arXiv:1201.5885.

[113] A. Franchi, *Studies and Measurements of Linear Coupling and Nonlinearities in Hadron Circular Accelerator* (GSI DISS 2006-07, 2006), PhD thesis.

[114] A. Franchi *et al.Vertical emittance reduction and preservation in electron storage rings via resonance driving terms correction* Vol. 14 (, 2011), https://doi.org/10.1103/PhysRevSTAB.14.034002.

[115] A. Franchi, R. Tomás, and F. Schmidt*Magnet strength measurement in circular accelerators from beam position monitor data* Vol. 10 (, 2007), https://doi.org/10.1103/PhysRevSTAB.10.074001.

[116] B. Härer, *Lattice Design and Beam Optics Calculations for the new Large-Scale Electron-Positron-Collider FCC-ee* (Dissertation from KIT, 2017), PhD thesis.

[117] T. K. Charles *et al.*, Low-emittance tuning for circular colliders, 2019, https://api.semanticscholar.org/CorpusID:182786300.

[118] T. K. Charles *et al.Alignment & stability challenges for FCC-ee* Vol. 10 (, 2023), https://cds.cern.ch/record/2856733.

[119] M. Hofer, Fcc-ee gitlab optics and data repository, `https://gitlab.cern.ch/acc-models/fcc/fcc-ee-lattice`.

[120] Future circular collider electron positron collider optics repository, `https://acc-models.web.cern.ch/acc-models/fcc/fccee/supplementary/`.

[121] Strategic accelerator design (sad) homepage, https://acc-physics.kek.jp/SAD/.

[122] F. Carlier, Xsequence: Managing lattices and models, https://indico.cern.ch/event/1088545/contributions/4576203/attachments/2343958/3996516/Xsequence%20.pdf.

[123] F. Carlier, xconverters github repository, https://github.com/fscarlier/xconverters/tree/main.

[124] E. Musa, Optics-corrections-with-pyat github repository, https://github.com/elafmusa/Optics-corrections-with-PyAT/tree/main.

[125] V. Sajaev*Commissioning simulations for the Argonne Advanced Photon Source upgrade lattice* Vol. 22 (American Physical Society, 2019).

[126] T. Hellert, C. Steier, and M. Venturini*Lattice correction and commissioning simulation of the Advanced Light Source upgrade storage ring* Vol. 25 (American Physical Society, 2022).

[127] FCC-ee Tuning WG Meeting Discussions, FCC-ee Tuning WG online Meeting.

[128] T. Charles, *Accelerator Physicist, Australian Synchrotron* , charlest@ansto.gov.au.

[129] E. Musa, I. Agapov, and T. Charles, JACoW **IPAC2023**, WEPL017 (2023), https://doi.org/10.18429/JACoW-IPAC2023-WEPL017.

[130] L. Malina *et al.*, Python version of simulated commissioning toolkit for synchrotrons pysc github repository, https://github.com/lmalina/pySC.

[131] L. Malina, E. Musa, J. Keil, and I. Agapov*Python Library for Simulated Commissioning of Storage-Ring Accelerators* Vol. ICALEPCS2023 (, 2023), https://doi.org/10.18429/JACoW-ICALEPCS2023-FR2AO05.

[132] E. Musa and L. Malina, pysc/correction/loco.py at master · lmalina/pysc, 2024, LOCO module in PySC, Accessed: 2024-07-07.

[133] Deutsches Elektronen-Synchrotron (DESY) website, https://www.desy.de/.

[134] C. S. et al., *PETRA IV: Upgrade of PETRA III to the Ultimate 3D X-ray Microscope* (DESY, 2019), Upgrade of PETRA III to the Ultimate 3D X-ray Microscope.

[135] I. Agapov *et al.*, Status of the PETRA IV Project, in *10th International Particle Accelerator Conference*, p. TUPGW011, 2019, Status of the PETRA IV Project.

[136] J. Bauche and others., *Progress of the FCC-ee Optics Tuning Working Group* (, 2023), https://doi.org/10.18429/JACoW-IPAC2023-WEPL023.

[137] S. Liuzzo, *Comparing Sensitivities to Errors Between FCC and CEPC Plus Tuning Studies* (, 2024), https://indico.cern.ch/event/1384058.

[138] S. Liuzzo, *Benchmark of commissioning simulations with errors and corrections: AT vs MADX vs MADX PTC* (, 2024), Talk.

[139] S. Jagabathuni, *FCC-ee IP Tuning Simulations* (FCC-ee Optics Tuning Meeting, 10 April 2024), FCC-ee IP Tuning Simulations.

[140] S. Liuzzo *et al.Commissioning Simulations Tools Based on Python Accelerator Toolbox* Vol. 2687 (IOP Publishing, 2024), https://doi.org/10.1088/1742-6596/2687/3/032001.

[141] J. D. Walecka, *Fundamentals of Statistical Mechanics* (World Scientific, 2000), World Scientific.

[142] Website of MAD project, MAD, Accessed: 2022-12-3.

[143] T. Mad-X, *Methodical Accelerator Design Version 5.02.09 User's Reference Manual* .

[144] G. Guignard, *Betatron coupling: Merging Hamiltonian and matrix approaches*CERN Yellow Reports: Monographs (CERN, Geneva, 1976), The General Theory of All Sum and Difference Resonances in a Three-Dimensional Magnetic Field in a Synchrotron.

[145] S. Liuzzo, Lattice studies for FCC-ee V22 and HFD-51, 2023, https://indico.cern.ch/event/1265820/.

Appendix A

Lattice sensitivity to errors

A.1 Comparison between: Z and $t\bar{t}$ lattices

A.1.1 Horizontal and vertical beta beating at different locations

Figures A.1, A.2 and A.3 show that the horizontal and vertical beta values for the Z lattice at different locations are higher than $t\bar{t}$ lattice.

A.1.2 Optics response to increase of alignment errors

Horizontal Dx and vertical Dy random misalignment errors with standard deviation in the range:

$$[0.0, 2 \times 10^{-7}, 4 \times 10^{-7}, 6 \times 10^{-7}, 8 \times 10^{-7}, 10 \times 10^{-7}, 12 \times 10^{-7}]$$

were applied to all quadrupoles, sextupoles, and dipoles without any corrections. Sextupoles and radiation were turned on.

The resulted changes in various optics parameters show a larger distortion for the Z lattice compared to the $t\bar{t}$ lattice. This indicates that the Z lattice is more sensitive to errors and thus harder to correct than the $t\bar{t}$ lattice.

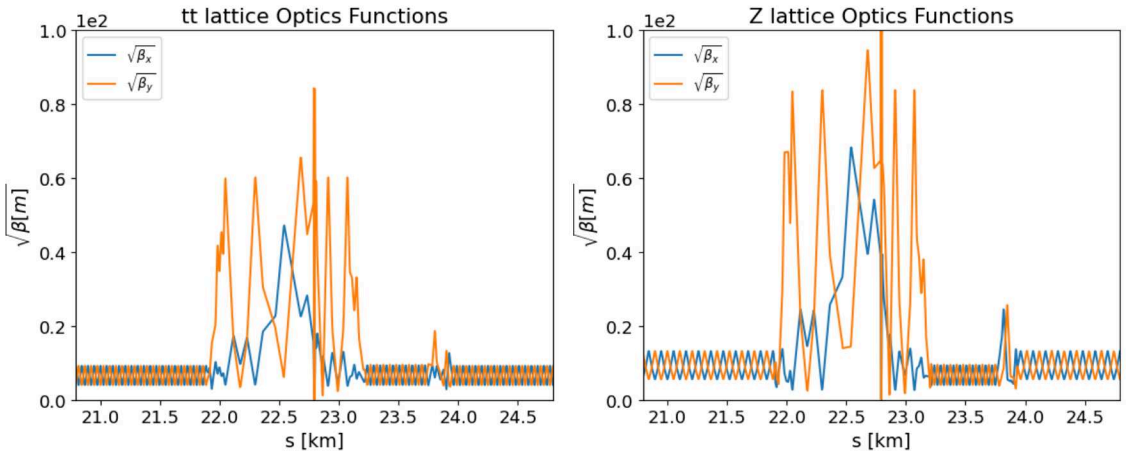

Figure A.1: Horizontal and vertical beta beating around one IP for the baseline $t\bar{t}$ (left) and Z (right).

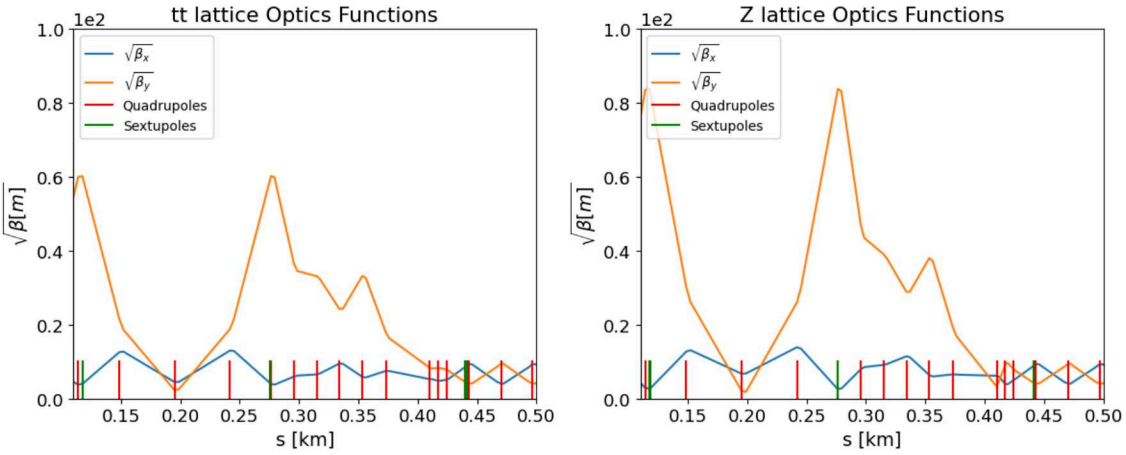

Figure A.2: Horizontal and vertical beta beating at the locations of strong quadrupoles and sextupoles in the IR for $t\bar{t}$ (left) and Z (right).

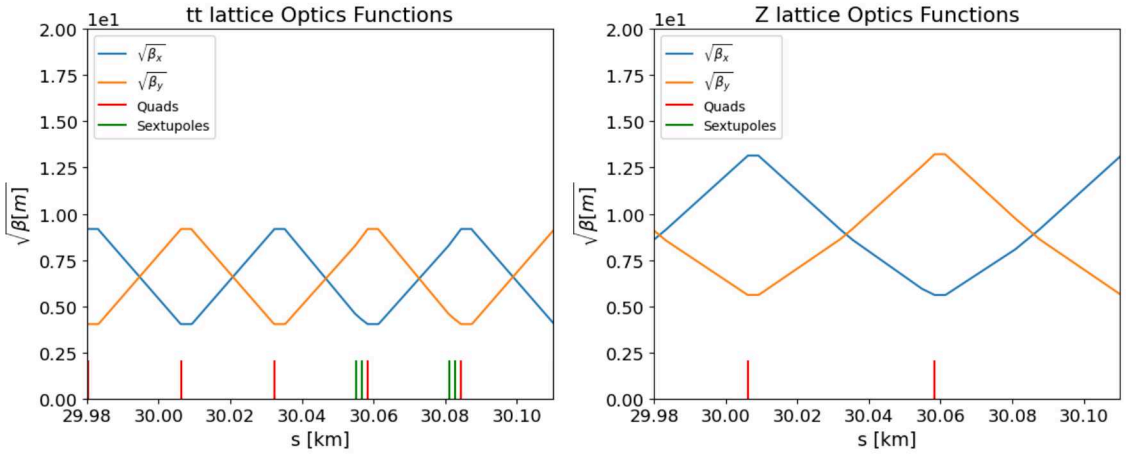

Figure A.3: Horizontal and vertical beta beating at the locations of quadrupoles and sextupoles in the arc region for $t\bar{t}$ (left) and Z (right).

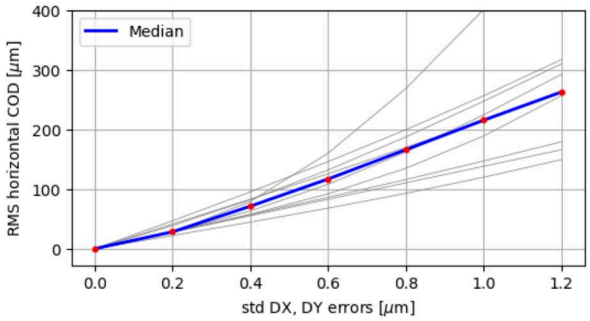

Figure A.4: Horizontal COD for Z lattice

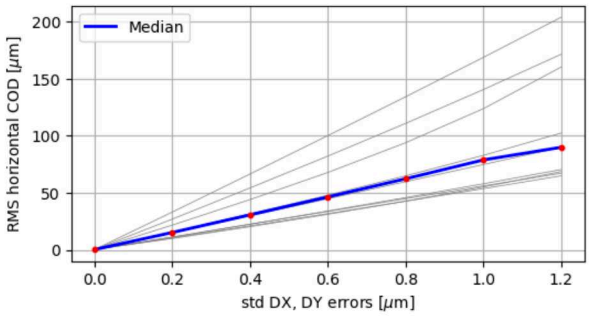

Figure A.5: Horizontal COD for $t\bar{t}$ lattice

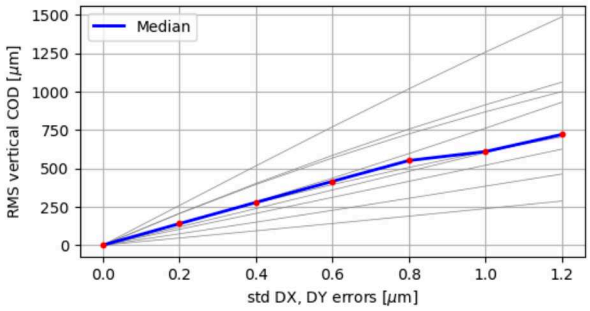

Figure A.6: Vertical COD for Z lattice

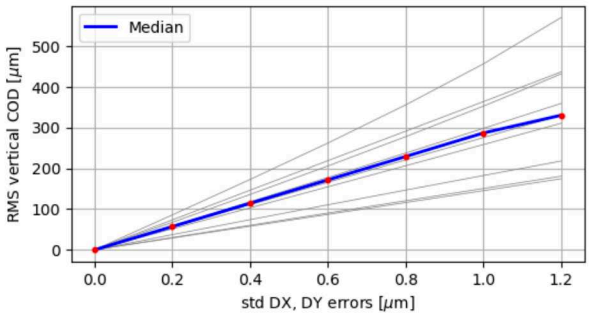

Figure A.7: Vertical COD for $t\bar{t}$ lattice

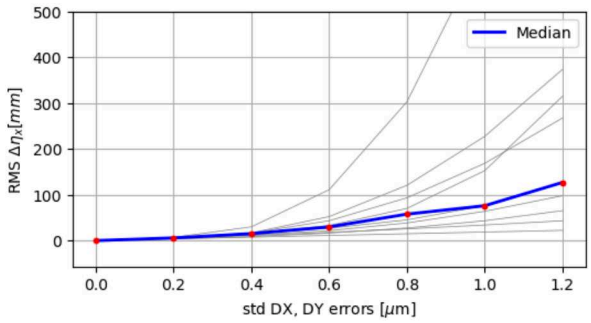

Figure A.8: Horizontal dispersion for Z lattice

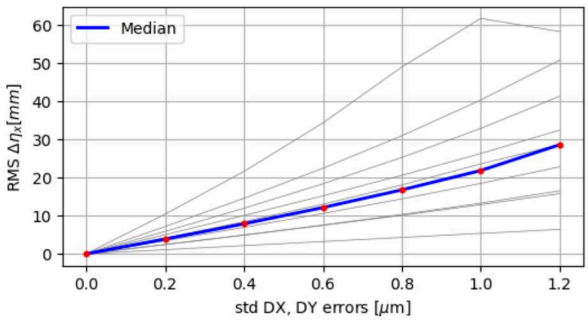

Figure A.9: Horizontal dispersion for $t\bar{t}$ lattice

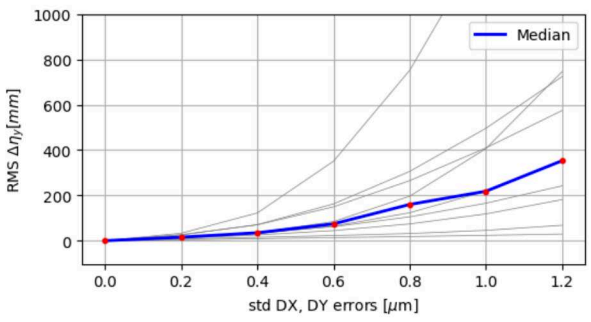

Figure A.10: Vertical dispersion for Z lattice

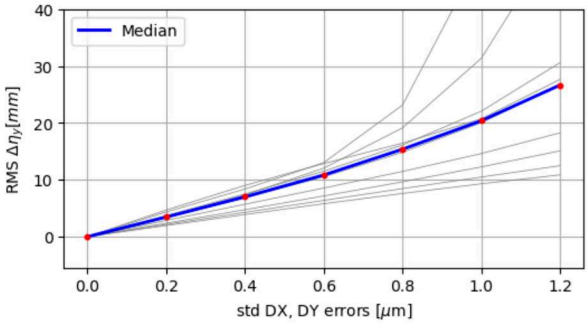

Figure A.11: Vertical dispersion for $t\bar{t}$ lattice

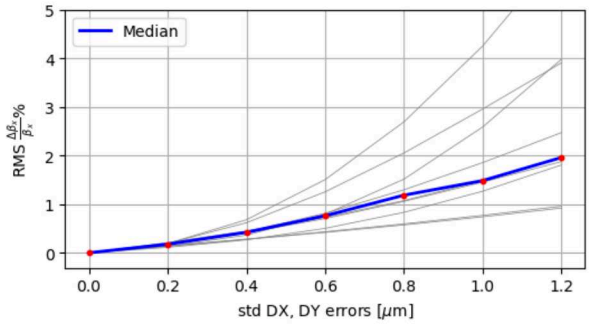

Figure A.12: Horizontal beta beating for Z lattice

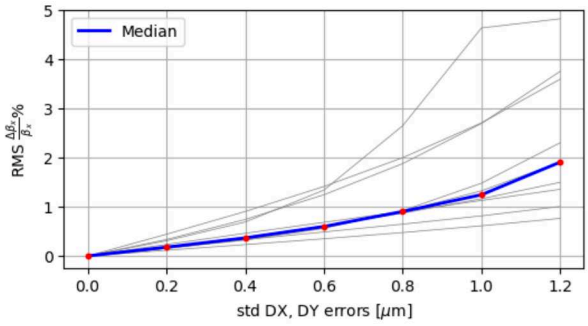

Figure A.13: Horizontal beta beating for $t\bar{t}$ lattice

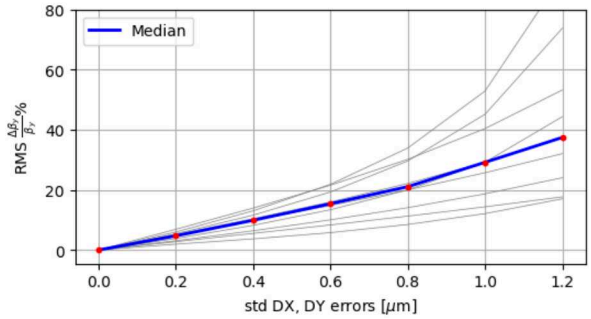

Figure A.14: Vertical beta beating for Z lattice

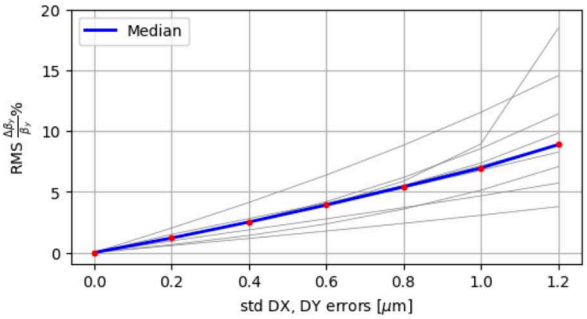

Figure A.15: Vertical beta beating for $t\bar{t}$ lattice

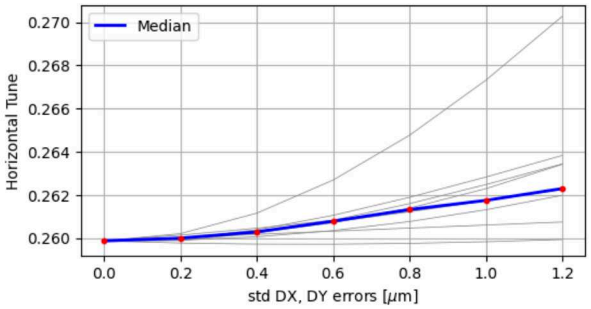

Figure A.16: Horizontal tune for Z lattice

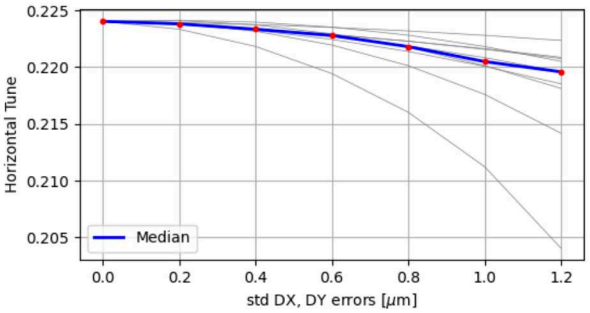

Figure A.17: Horizontal tune for $t\bar{t}$ lattice

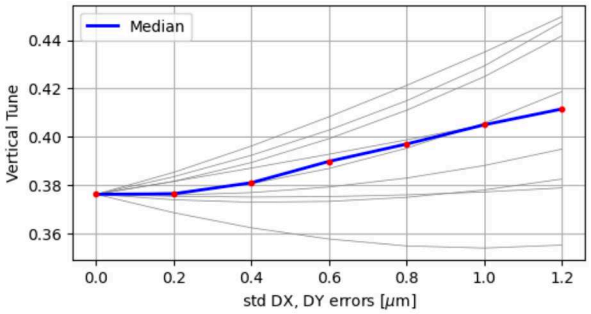

Figure A.18: Vertical tune for Z lattice

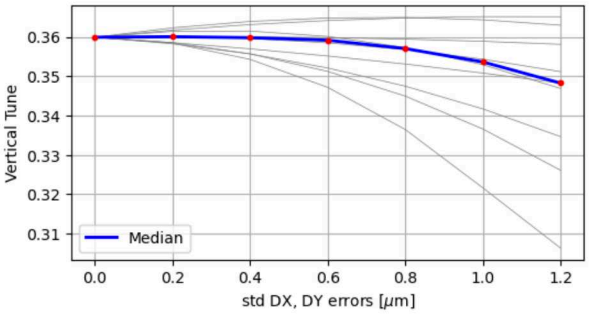

Figure A.19: Vertical tune for $t\bar{t}$ lattice

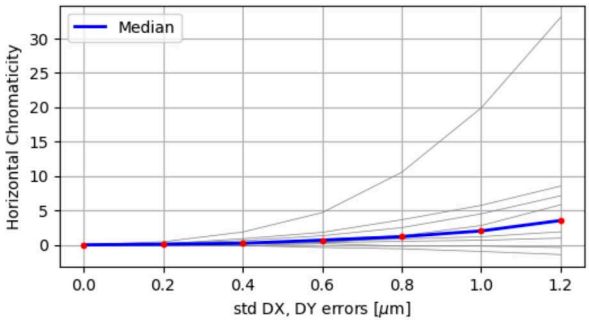

Figure A.20: Horizontal chromaticity for Z lattice

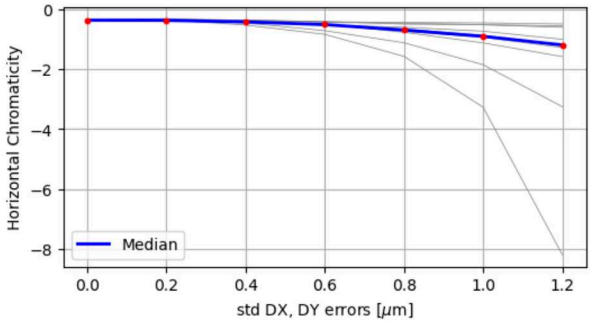

Figure A.21: Horizontal chromaticity for $t\bar{t}$ lattice

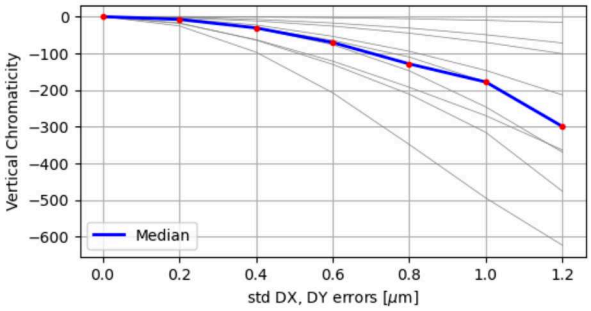

Figure A.22: Vertical chromaticity for Z lattice

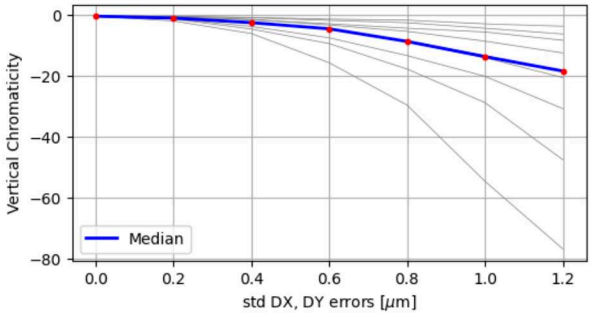

Figure A.23: Vertical chromaticity for $t\bar{t}$ lattice

A.2 Sensitivity to errors while sextupoles are turned off

This study examines various misalignments applied to the baseline Z lattice and the LCCO lattice, with sextupoles turned off and without considering synchrotron radiation (SR). Table A.1 provides a summary of the misaligned elements, detailing the types of misalignment and their corresponding standard deviation values.

Misaligned elements	Type of misalignment	Value (μm)
Arc quads	Hor & Ver displacement	10,20,30,40,50
Arc sextupoles	Hor & Ver displacement	10,20,30,40,50
All dipoles	Hor & Ver displacement	10,20,30,40,50
IR quads	Hor & Ver displacement	10
IR sextupoles	Hor & Ver displacement	10
IR quads	Hor & Ver displacement	10
IR sextupoles	Hor & Ver displacement	10
Arc quads	Hor & Ver displacement	10
Arc sextupoles	Hor & Ver displacement	10
All dipoles	Hor & Ver displacement	10
Arc quads	Displacement + 3 angles rotations	10
Arc sextupoles	Displacement + 3 angles rotations	10
All dipoles	Displacement + 3 angles rotations	10

Table A.1: Applied random misalignment standard deviation to the baseline and the LCCO lattice

Table. A.2 presents a summary of the results for the baseline lattice. Before applying any correction PyAT failed to give values for the horizontal and vertical emittance. Table. A.3 illustrates the combined impact of displacements and three-angle rotations on the arc components of the baseline lattice. Tables A.4 and A.5 shows impact of horizontal and vertical displacement errors and combined impact of displacements and three-angle rotations errors on arc components of the LCCO lattice.

A comparison between the impact of errors in the arc component and the IR component is presented in Tables A.6 and A.7. These results highlight the greater sensitivity of the IR magnets to errors compared to the arc even when we apply the errors while sextupoles are turned off.

Table A.2: Impact of errors on the arc components of the baseline lattice (sextupoles off)

50 seeds		rms orbit $x(\mu$m)	rms orbit $y(\mu m)$	$\Delta\beta_x/\beta_x$ %	$\Delta\beta_y/\beta_y$ %	$\Delta\eta$x (mm)	$\Delta\eta$y (mm)
10	mean	661.124	766.072	0.634	0.96	1294.322	8109.671
	std	298.55	297.023	0.199	0.480	835.080	5724.043
20	mean	1119.57	1493.39	1.175	2.101	2002.22	16028.51
	std	515.597	533.66	0.38	0.766	1572.75	10891.68
30	mean	1929.019	2231.965	1.7474	3.232	3807.41	23466.34
	std	713.98	816.58	0.60	1.364	2041.58	15785.598
40	mean	2728.836	2719.68	2.282	3.855	5333.75	28634.589
	std	1231.93	945.22	0.77	1.466	3920.526	18881.92
50	mean	3167.085	4092.77	3.159	4.722	5787.87	47111.809
	std	1150.435	1426.808	1.109	1.650	3101.976	28390.57

Table A.3: Adding 3 angle rotations errors on the arc component of the baseline lattice (sextupoles off)

50 seeds		rms orbit $x(\mu$m)	rms orbit $y(\mu m)$	$\Delta\beta_x/\beta_x$ %	$\Delta\beta_y/\beta_y$ %	$\Delta\eta$x (mm)	$\Delta\eta$y (mm)
10	mean	31164.707	47166.624	0.000111	0.00072	58755.728	567394.68
	std	11936.754	18719.737	9.2468e-5	0.000528	36254.366	362336.1789

Table A.4: Impact of errors on the arc components of the LCCO lattice (sextupoles off)

50 seeds		rms orbit $x(\mu$m)	rms orbit $y(\mu m)$	$\Delta\beta_x/\beta_x$ %	$\Delta\beta_y/\beta_y$ %	$\Delta\eta$x (mm)	$\Delta\eta$y (mm)
10	mean	516.648	696.162	0.105	0.155	784.96	10010.68
	std	225.787	302.49	0.034	0.047	497.55	7323.88
20	mean	1225.07	1474.85	0.217	0.284	1851.64	20718.83
	std	617.80	710.84	0.062	0.088	1306.106	16730.28
30	mean	1489.96	2344.05	0.315	0.46	2310.64	37264.89
	std	734.088	1022.65	0.11	0.147	1479.00	22877.194
40	mean	2337.88	2888.37	0.422	0.565	3530.76	42327.42
	std	1149.749	1379.435	0.135	0.165	2424.226	31200.389
50	mean	2862.97	3582.41	0.554	0.180	4198.65	48326.76
	std	1070.23	1697.705	0.73	0.233	2270.49	41387.56

Table A.5: Adding 3 angle rotations errors on the arc component of the LCCO lattice (lattice has more dipoles) (sextupoles off)

50 seeds		rms orbit $x(\mu$m)	rms orbit $y(\mu m)$	$\Delta\beta_x/\beta_x$ %	$\Delta\beta_y/\beta_y$ %	$\Delta\eta$x (mm)	$\Delta\eta$y (mm)
10	mean	25586.888	40993.606	7.2374	6.0228	52672.23	646282.484
	std	10620.314	19734.425	6.5592	6.2218	33258.3938	481665.556

Table A.6: Impact of 10μm displacement errors on the IR components compared to arc components of the baseline lattice

50 seeds		rms orbit $x(\mu$m)	rms orbit $y(\mu m)$	$\Delta\beta_x/\beta_x$ %	$\Delta\beta_y/\beta_y$ %	$\Delta\eta$x (mm)	$\Delta\eta$y (mm)
Arc	mean	661.124	766.072	0.634	0.96	1294.322	8109.671
	std	298.55	297.023	0.199	0.480	835.080	5724.043
IR	mean	1869.318	9841.29	3.835e-7	0.000245	4185.86	132811.62
	std	977.78	5324.56	2.979e-7	0.0001079	2937.15	93501.923
IR & Arc	mean	2188.74	10110.069	4.112e-7	0.000238	4992.816	140701.77
	std	1367.978	6899.897	3.712e-7	0.000108	4114.458	116837.422

Table A.7: Impact of 10μm displacement errors on the IR components compared to arc components of the LCCO lattice

50 seeds		rms orbit $x(\mu\text{m})$	rms orbit $y(\mu m)$	$\Delta\beta_x/\beta_x$ %	$\Delta\beta_y/\beta_y$ %	$\Delta\eta$x (mm)	$\Delta\eta$y (mm)
Arc	mean	516.648	696.162	0.105	0.155	784.96	10010.68
	std	225.787	302.49	0.034	0.047	497.55	7323.88
IR	mean	1330.41	10526.986	0.0174	0.0121	2478.838	185857.68
	std	855.02	7088.24	0.0279	0.01862	1880.62	149578.20
IR & Arc	mean	1244.963	10843.207	0.020128	0.01409	2137.126	192494.10
	std	613.874	6803.66	0.0203	0.0150	1399.52	146679.656

Appendix B

Application of LOCO optics correction in PETRA IV lattice

- The developed Python-based numerical code of LOCO has been tested using PETRA IV lattice, version (p4_H6BA_v4_2_4)
- The following two cases were applied:
    1. Applying random relative field errors distributed via a Gaussian with $\Delta k/k = 1 \times 10^{-3}$ to all lattice quadrupoles.
    2. Adding to the field errors horizontal and vertical random relative calibration errors distributed via a Gaussian with a standard deviation $\sigma = 1 \times 10^{-3}$.
- Reduced size LOCO were utilized with 20 horizontal and 20 vertical steering magnets and all BPMs, totalling 2×790 BPMs.
- All lattice normal quadrupoles were used in the fit, totaling 1348 normal quadrupoles.
- The jacobian calculations with dimensions $\mathrm{J}(1348, 40, 1580)$ took approximately 26.4 minutes in DESY Maxwell cluster, performing multiprocessing parallelization.
- Three LOCO iterations were performed.

- Fifty simulations were conducted using different initial conditions (seeds). The mean and standard deviation of the optical parameters were calculated from these simulations.

B.1 Normal quadrupoles field errors

In the first case, where only quadrupole field errors were applied, the results showed 8.92 % horizontal and 8.92 % vertical rms beta beating, with a relative horizontal dispersion of 2.71 mm. These values represent the initially distorted state before any corrections were applied.

Table. B.1 shows the improvement of the horizontal and vertical beta beating and horizontal dispersion in addition to the horizontal emittance over the three LOCO iterations. As noticed from the table the first LOCO iteration has the most impact on reducing the optics parameters, this resulted from choosing relatively large number of singular values when performing the SVD leading to faster convergence of the fit.

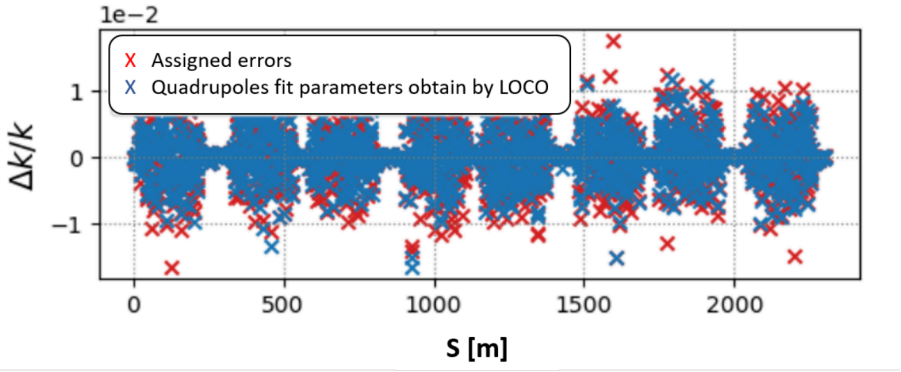

Figure B.1: Relative quadruple strengths obtained by the first iteration of LOCO compared to random relative errors $\Delta k/k = 10^{-3}$, for a single seed.

Figure. B.1 reflecting this, by showing a good reconstruction of the errors after the first LOCO iteration for one of the seeds, the remaining iteration helped in fine tuning the results. Figure. B.2 shows the reduction on the percentage horizontal and vertical

rms beta beating for the 50 seeds over the iterations. The reduction on the horizontal dispersion and the horizontal emittance are shown in Fig. B.3 and Fig. B.4 respectively. The Horizontal and vertical emittance frequency distribution of 50 seeds after following the LOCO iteration are shown in Fig. B.5, demonstrating a reduction in horizontal emittance across most seeds.

Table B.1: Impact of errors on optics parameters and the improvement of the optics values over 3 LOCO iterations with field errors applied to all quadruples.

One seed		$\Delta\beta_x/\beta_x$ (%)	$\Delta\beta_y/\beta_y$ (%)	$\Delta\eta_x$ (mm)	ε_{v} (nm)
$\Delta k/k = 1e-3$	mean	8.92	5.74	2.71	-
	std	3.70	1.91	1.62	-
LOCO 1	mean	2.65	1.43	1.24	0.0204
	std	1.50	0.49	0.68	0.000079
LOCO 2	mean	1.55	1.21	0.71	0.0199
	std	2.09	0.38	0.38	0.000029
LOCO 3	mean	1.26	1.19	0.70	0.0199
	std	0.66	0.38	0.35	0.00026

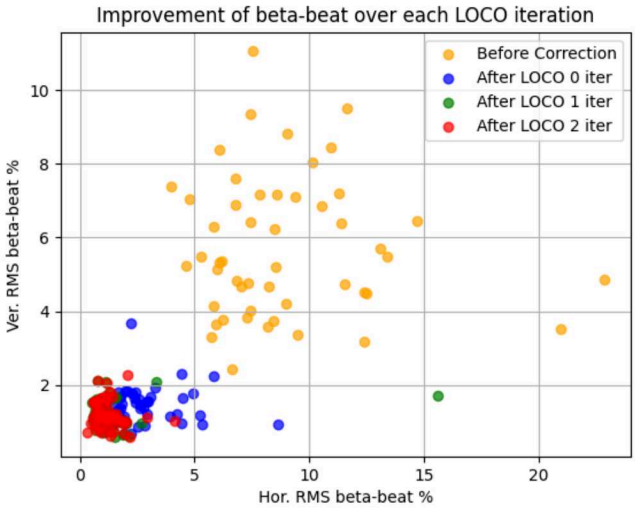

Figure B.2: Horizontal and vertical beta beating improvement over 3 LOCO iterations

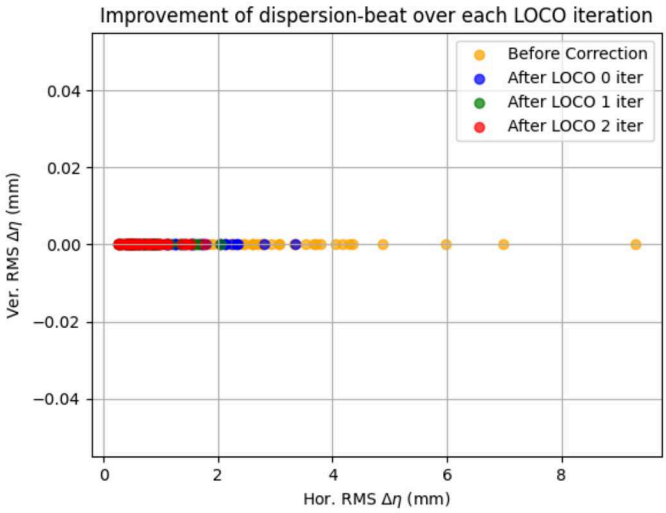

Figure B.3: Horizontal dispersion improvement over 3 LOCO iterations

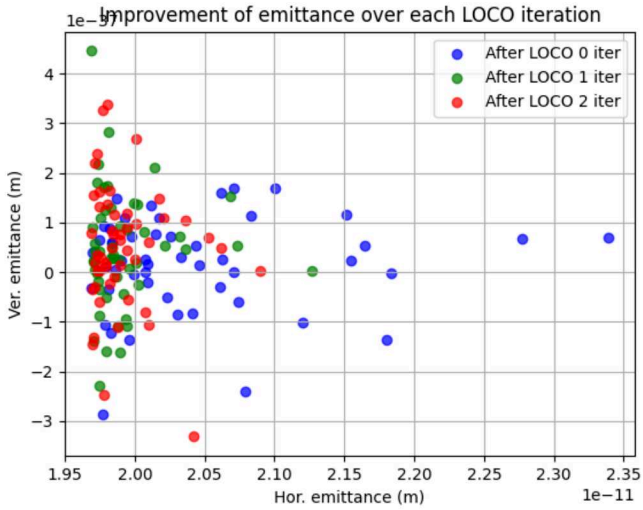

Figure B.4: Horizontal emittance improvement over 3 LOCO iterations

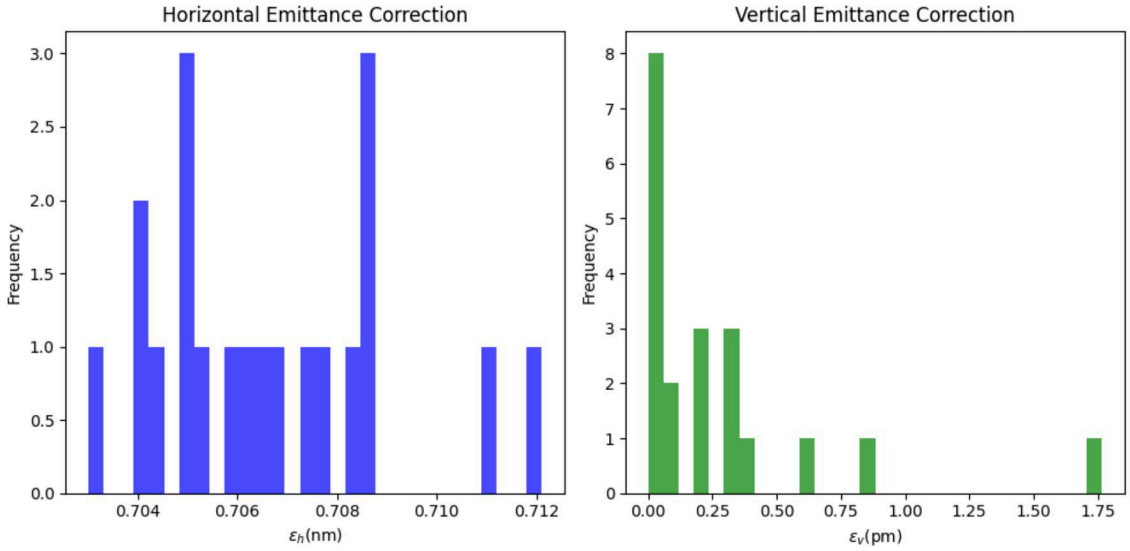

Figure B.5: Horizontal emittance frequency distribution of 50 seeds after following the LOCO iterations.

B.2 Adding calibration errors to BPMs and steering magnets

The second case that we examined, was by increasing the number of parameters used in the LOCO fit. The calibration errors of the BPMs and the steering magnets do not have large impact on the optics parameters values, as represented in Tab. B.2 however, these errors must be taken into account in order to achieve better fitting as illustrated in the formula Eq.(3.27). Table. B.2 shows the correction of the optics parameters up to 1.746% and 1.85% rms horizontal and vertical beta beating respectively and 0.92 mm relative horizontal dispersion.

Table B.2: Impact of field errors in all lattice quadruples, including BPMs and correctors calibrations, and the improvement of optics values over 3 LOCO iterations.

One seed		$\Delta\beta_x/\beta_x$ (%)	$\Delta\beta_y/\beta_y$ (%)	$\Delta\eta_x$ (mm)	ε_v (nm)
$\Delta k/k = 1e-3$	mean	9.15	5.47	2.66	-
	std	3.10	1.59	1.199	-
LOCO 1	mean	2.66	2.04	2.31	0.022
	std	1.02	0.68	0.93	0.0018
LOCO 2	mean	1.789	1.88	0.17	0.021
	std	0.67	0.71	0.90	0.0016
LOCO 3	mean	1.746	1.85	2.08	0.021
	std	0.66	0.68	0.92	0.0016

Figure. B.6 illustrates the reduction in the horizontal and vertical rms beta beating across 50 seeds over 3 LOCO iterations in case of including quadrupoles field errors and calibration errors to BPMs and steering magnets. Figure. B.7 presents the horizontal and vertical emittance frequency distribution of the corrected 50 seeds iterations.

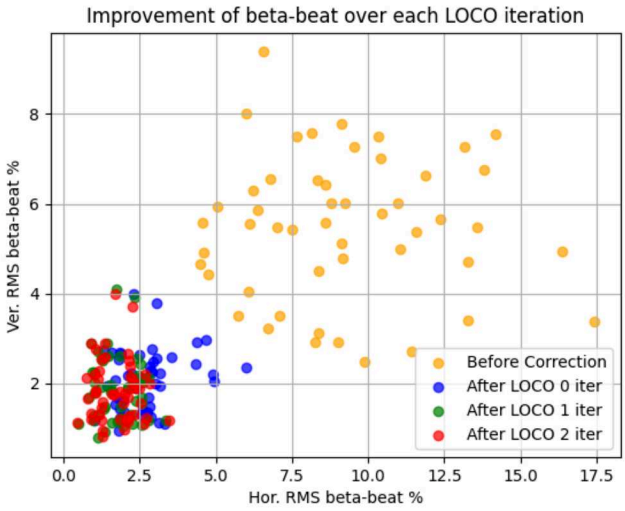

Figure B.6: Horizontal and vertical beta beating improvement over 3 LOCO iterations

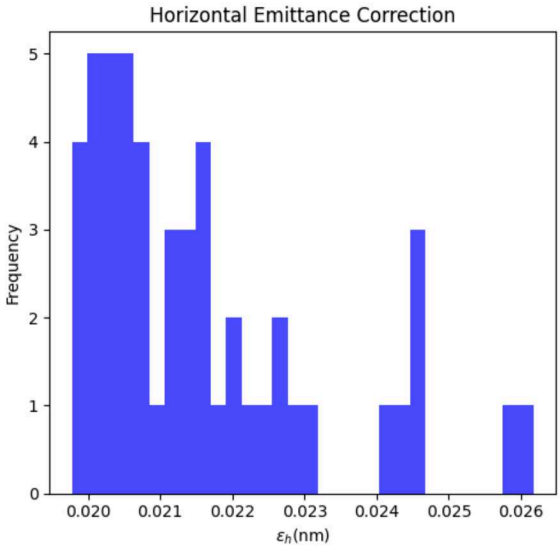

Figure B.7: Horizontal emittance frequency distribution of 50 seeds after following the LOCO iterations.

Acknowledgements

As I reach the Acknowledgments section of my thesis, I reflect on the past three years with gratitude. Starting my PhD journey in Germany, the valuable time I spent at CAS schools, the connections I've made with fellow accelerator physicists, and engaging in useful workshops and conferences—all these experiences have greatly enriched my research and personal growth.

None of the work presented in this thesis would have been possible without the unwavering support of many individuals, to whom I extend my heartfelt thanks.

First and foremost, I am deeply grateful to Dr. Ilya Agapov, whose guidance, advice, support, and supervision over the past three years have been instrumental in both my work and personal development. I am sincerely thankful to Dr. Tessa Charles for her encouragement, enlightening discussions, and her limitless and invaluable assistance.

I have had the opportunity to closely collaborate with colleagues from CERN through the FCCIS project. I would like to thank Dr. Frank Zimmerman for the opportunity to present my work at several workshops and conferences. I also extend thanks to the entire FCC-ee optics tuning group for their insightful discussions and motivation during meetings, particularly Dr. Rogelio Tomas, Prof. Dr. Katsunobu Oide, Dr. Jacqueline Keintzel, and all my colleagues for their support and contributions.

The Python Accelerator Toolbox has been instrumental in my research, from the initial installation of the tool and creation of a simple FODO cell lattice to conducting tuning simulations for the proposed future collider. My sincere gratitude goes to the AT collaboration group and colleagues from ESRF, particularly Dr. Laurent Farvacque, Dr. Simone

Liuzzo, Dr. Simon White, and Dr. Lee Carver, for their extensive assistance and their willingness to share their expertise and valuable insights.

I would also like to express my gratitude to my colleagues at DESY and the PETRA IV Beam Physics group for their assistance and useful discussions.

I extend my sincere thanks to the professors at the Physics Department of Cairo University, for introducing me to the field of accelerator physics.

On a personal note, I am deeply grateful to my parents, Sara Ali and Salah Musa, for their unlimited support, care, and encouragement from my earliest days. I fondly remember discovering my interest in physics at a young age when I stumbled upon a book about Richard Feynman, translated into Arabic, at the library my parents took me to. To my siblings, thank you for sending encouraging messages and inspiring me with your amazing stories. I also draw inspiration from the resilience and achievements of people from my home country, Sudan, which have motivated me throughout my journey.

My heartfelt thanks to all my friends for their encouragement and the memorable time we shared, exploring and enjoying a variety of experiences.

Finally, this work represents a documentation of a three-year journey and serves as a foundation for future expansion. Like research itself, this journey is ongoing.